IMPACT BEHAVIOUR OF AN INNOVATIVE TRAPEZOIDAL COMPOSITE CORRUGATED CORE SANDWICH STRUCTURE UNDER LOW-VELOCITY IMPACT: AN EXPERIMENTAL AND NUMERICAL STUDY

A Thesis submitted by

Sartip Zangana, M Eng

For the award of

Doctor of Philosophy

2020

Abstract

Composite core sandwich structures have been extensively used in aerospace, marine and automotive applications. A few configurations of composite cores have been used in manufacturing sandwich structures for many years. The usual configurations for a corrugated shape are sinusoidal, triangular and trapezoidal shapes. Unfortunately, until now there only has been limited research on the development of trapezoidal composite corrugated cores.

This is significant because sandwich structures in general are often subjected to compression loads and low-velocity impacts during their service life. Failure in composite core sandwiches can be internal and thus not easily noticed. Hence, the mechanical behaviour and failure mechanism of these structures under compression and low-velocity impact loads need to be clearly understood before being used for critical structural applications.

This project intends to fill the gap in the knowledge based on the trapezoidal composite corrugated core sandwich (TCS) structures by investigating the mechanical behaviours and failure mechanism of innovative TCS structure through a well planned experimental framework: quasi-static compression and low-velocity impact loading conditions. The initial experimental tests were limited to a single-cell of a trapezoidal composite corrugated core; later a few multi-cell specimens were experimentally investigated.

Under a quasi-static compression load, results showed that TCS structures are highly anisotropic, as anticipated, and possess superior mechanical behaviour compared to traditional foam, composite honeycomb, and a composite lattice core sandwich. The impact behaviours of TCS structure designs were investigated under low-velocity impact at the visible damage threshold energy of the composite parent materials and at roughly 30% greater than this. The damage mechanisms were scrutinized using high-speed video recordings. During the single-cell investigations, changes in design parameters of the core structure were also thoroughly investigated. TCS structure designs have shown superior impact performances and high resistance in comparison with monolithic composite plate. They also absorbed more impact energy than the visible damage threshold energy of composite parent materials, without a noticeable core fracture.

Where the impact energy exceeded the composite parent materials' visible damage threshold energy, the impact response of the TCS structure performed significantly different depending on the core thickness and the core height. The core thickness was found the most critical influence on single-cell impact performance. The major damage mechanism was identified as starting when the core fails at the upper core angle, followed by a flattening deformation of the lower core angle.

In addition to experimental studies, comprehensive 3D finite element (FE) modelling was undertaken to analyse TCS structures under static and impact/dynamic loading using ANSYS software. Both implicit and explicit dynamic 3-D FE models demonstrated an excellent correlation with the experimental results. Interestingly, predicted mechanical properties under quasi-static compression load, damage area, and energy absorption capacity of the TCS structure correlate exactly with the experimental findings. After successful FE modelling regimes, an effective approach to optimizing the trapezoidal composite corrugated core of the sandwich structure was developed.

Finally, two case studies of multi-cell TCS structures were performed to prove the superior performances of optimized TCS structures. The first case involved the full-scale multi-cell TCS structures fabricated from woven E-glass fibre reinforced epoxy composite material. As anticipated, these structures showed the highest impact resistance, the highest energy absorption and superior impact performance. Furthermore, in full-scale TCS structures, the optimal core design eliminated core fracture damage and TCS structure penetration.

The second case was for a multi-cell TCS structure of hybrid composite core configuration, fabricated from high-performance fibre: kevlar and zaylon. These showed superior impact resistant performances: and severe core failure was eliminated and damage on the upper face sheet could easily be repaired. Furthermore, the hybrid TCS structures provided a high specific energy absorption (SEA) rate with the same structural weight as traditional core materials. In addition, the residual strength and stiffness of the hybrid TCS structures exceeded those of the E-glass fibre composite TCS structure.Finally, the optimized design was extended to a reasonably configured full-scale sample and hybrid core that experimentally proved its superior performances in terms of high impact resistance, high residual strength and core damage prevention.

Certification of Thesis

This thesis is entirely the work of Sartip Zangana except where otherwise acknowledged. The work is original and has not previously been submitted for any other award, except where acknowledged.
Student and supervisors signatures of endorsement are held at University

Principal Supervisor: Assoc. Prof **Jayantha Epaarachchi**

Associate Supervisor: Prof **Peter Schubel**

Associate Supervisor: Assoc. Prof **Canh-Dung Tran**

Acknowledgements

*I would like to express my great thanks to **my mother** and **my family** for their support.*

I would like to express my heartfelt gratitude to my principal supervisor Assoc. Prof **Jayantha Epaarachchi** for his kind dedicated guidance and encouragement. He kept me going in the right direction and also allowed me to seek new and exciting challenges with more flexibility in following my research. I have highly appreciated his suggestions for improving the quality of this research. I would like to express my gratitude to my associate supervisor Prof **Peter Schubel** for his invaluable advice and fruitful discussions and I am so proud to work with him. I would also like to thank my associate supervisor Assoc. Prof **Canh-Dung Tran** for his valuable support.

I am also indebted to Dr. **Wahid Ferdous** for his valuable help in working as a research group.

My sincere gratitude to members of Centre of Future Materials, including Mr. **Martin Geach**, **Wayne Crowell**, and **Brian Lenske**, as well as my friends in the centre. Appreciation also is extended to my proof reader, **Julie Martyn** of Grammarfun. My acknowledgment to my sponsor **Iraqi Government**, and special thanks to the **Iraqi Cultural Attaché** office (Canberra) for all the supports during the period of the study.

Table of contents

Chapter 4 Experimental Results and Discussion

List of Figures

List of Tables

Abbreviations

Notation	Description
Ac	Cross-section of the core strut
AE	Absorbed energy
CD	Core direction
C_E	Specific ratio of impact energy to specimen thickness
CH	Conical impactor head
E_{11}	Young's modulus in the longitudinal direction of composite laminate
E_{22}	Young's modulus in the transverse direction of composite laminate
E_{33}	Young's modulus in the thickness direction of composite laminate
E_c	Core modulus elasticity
E_K	Kinetic energy
E_P	Threshold value of damaged energy
FH	Flat impactor head
F/F_o	Normalised residual capacity
G_{12}	In-plane shear modulus
G_{13}, G_{23}	Through thickness shear modulus
GC	Glass-fibre reinforced epoxy composite corrugated core
GK	Hybrid Kevlar Glass-fibre reinforced epoxy composite corrugated core
GZ	Hybrid Zylon Glass-fibre reinforced epoxy composite corrugated core
F	Axial compression load in the core strut
g	gravity
H	Composite sandwich height
HH	Hemispherical impactor head
h, h_c	Composite core height
h^i	Height of the impactor head before starting the movement
K	Constant depending on the end condition of the core struts
L	Core unit cell length
L1	Core short span length
L2	Core Lower member length
L3	Core long span length
L_c	Core strut length
MD	Machine direction
m	Impactor mass
P	Applied load
S1-T	Coupon specimen ID under tensile test
S1-C	Coupon specimen ID under compression test
S1-S	Coupon specimen ID under shear test
SEA	Specific energy absorption
sf	Shape factor depending on the geometry of the impactor head
SL	Support span length
S^L	Longitudinal shear strength
S^T	Transverse shear strength
TCS	Trapezoidal corrugated core sandwich structure
t	Total thickness of core thickness plus thickness of upper face sheet
t_c	Core thickness
t_u	Upper face sheet thickness

t_l	Lower face sheet thickness
v	Impact velocity
W	Composite sandwich weight
w	Core angle
w_1	Lower core angle
w_2	Upper core angle
X^T	Longitudinal tensile strength
X^C	Longitudinal compressive strength
Y^T	Transverse tensile strength
Y^C	Transverse compressive strength

Greek symbols

Notation	Description
α	Coefficient factor of contribution shear stress to the fibre tensile mode
β	Coefficient factor depends on impact strength of parent material
$d\delta$	Displacement
$d\varepsilon_x$	Strain in the X-direction
δ_{eq}	Equivalent strains
$d\varepsilon_y$	Strain in the y-direction
ρ	Density of the corrugated core
ρc	Relative density of composite corrugated core
ρo	Overall density of the core
$\hat{\sigma_{11}}$,	Effective normal stress tensors in fibre direction
$\hat{\sigma_{22}}$	Effective normal stress tensors in transverse direction
σ_c	Uniaxial core strut stress
σ_{eq}	Equivalent stress
$\hat{\tau_{12}}$	Shear stress tensor components
ν_{12}	In-plane Poisson's ratio
ν_{13} , ν_{23}	Through thickness Poisson's ratio
ν_{xy}	Poisson's ratio

Chapter 1

Introduction

1.1 Background and Significance

Sandwich structures have become more and more widespread among all engineering structures because of their unique mechanical behaviours, such as a high stiffness/strength-to-weight ratio and an excellent capability to absorb the impact energy (Dayyani et al., 2013, Bull et al., 2015, Zhang et al., 2013). Sandwich structures are typically fabricated by bonding two face sheets as upper and lower skins (liners) to a core layer, as shown in Figure 1.1. Adding core to face sheet plates leads to a slight increase in the face sheet weight. However, this core adding yields an increase in the moment of inertia of the cross-section of the sandwich structure. Thus it will improve the structural bending resistance and the buckling load. The elements of sandwich structures are made of either isotropic or non-isotropic materials. Depending on the core form and topology, sandwich structures can be differentiated. For example, Evans et al. (2001) and Wadley (2002) classified sandwich panels into three categories based on their core topology, as illustrated in Figure 1.2.

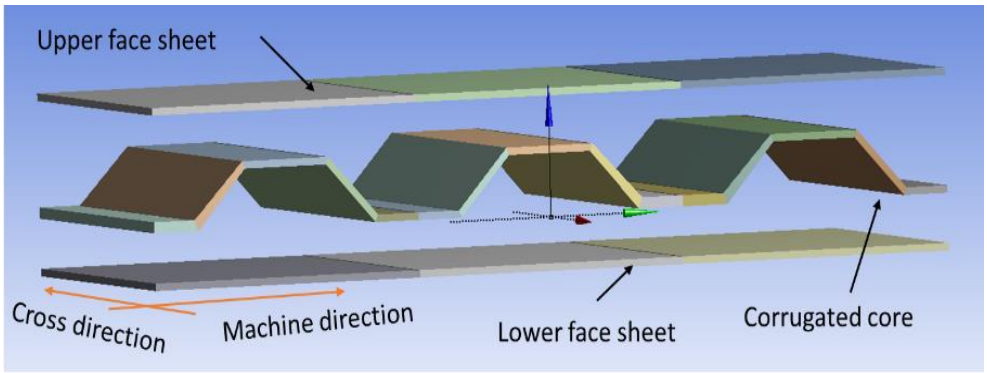

Figure 1.1: Schematic of trapezoidal corrugated core sandwich structure

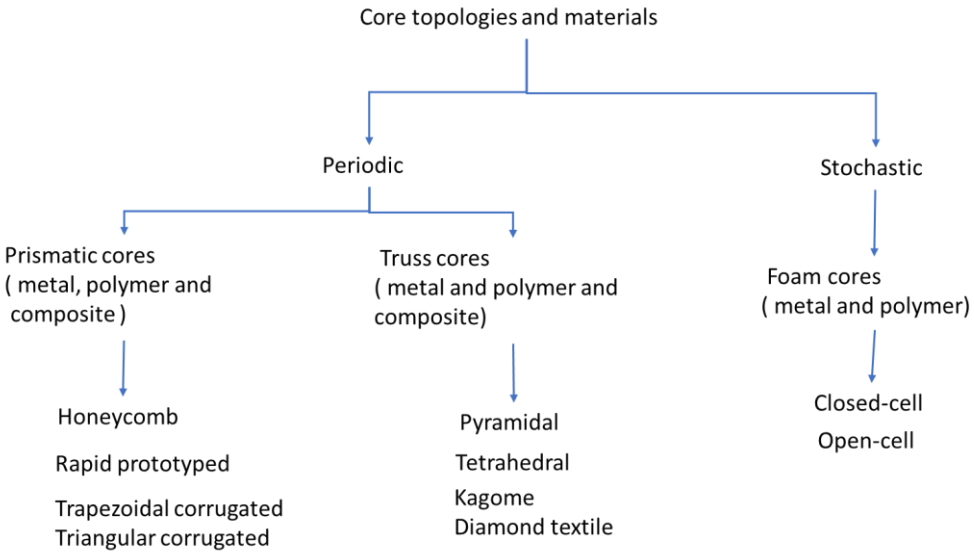

Figure 1.2: Topologies of core sandwich panel (Evans et al., 2001)

All these core topologies have been modified with the aim of improving the mechanical properties of the sandwich structures. The cores are preferably made from particular materials to achieve high mechanical properties such as flexural strength, stiffness, and low density. Moreover, core modification aims to further resist crushing impact loads and withstand in-plane and out-of-plane loads. For some specific applications, core modification also takes into account the thermal conductivity and fire resistance of core materials as design factors.

1.2 Corrugated Core Sandwich Structure

Corrugated core sandwich structures are considered to be efficient, among all sandwiches, owing to their unique mechanical behaviours. This means these sandwich structures have high stiffness in the transverse direction and excellent flexibility in the longitudinal direction (Thill et al., 2010) and corrugated cores exhibit significant in-plane anisotropy (Xiong et al., 2019). Moreover, corrugated sandwich structures display higher critical buckling and lower bending deflection in comparison with a monolithic plate of equal weight. Therefore, since the 19th century, the construction sector has used corrugated core sandwich structures, originally incorporating metals.

Furthermore, corrugated sandwich structures have multi-functional applications (Côté et al., 2006) such as the ability to support loads, change shape under external force and protect minor parts and instrumentation laid inside the core cavities, with

storage space for pressurized gas or liquid, and sound and vibration isolation, as shown in Figure 1.3. Logically, under loading conditions, there is also a relationship between the core integrity (i.e., the energy absorption capability) and the multi-function application (providing protecting for parts) of the corrugated core structures. Thus, improving the capability of the corrugated core sandwich to absorb energy and provide shock resistance usually leads to better protection of the small internal devices and parts running inside the structure.

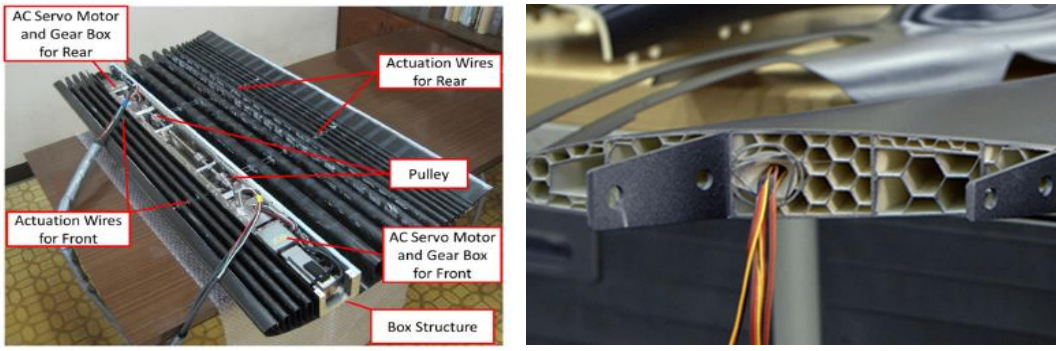

(a) (b)

Figure 1.3: Multi-functional characteristic of corrugated core structures (a) (Takahashi et al., 2016) and (b) (www.images.app.googl/ir)

Recently, lightweight composite materials have gradually made inroads into the construction of high-performance sandwich structures. This is due to their unique mechanical properties, in that they have a comparatively high stiffness-to-weight ratio, as shown in Figure 1.4. Innovative composite corrugated core sandwiches, therefore, have replaced traditional foam core, aluminium alloy and steel sandwich panels in a broader range of applications in the marine, aerospace, transportation industries. Besides their superior structural behaviours, these composite corrugated core structures offer dimensional stability, thermal insulation, and comparable performances in sound isolation to these traditional structures.

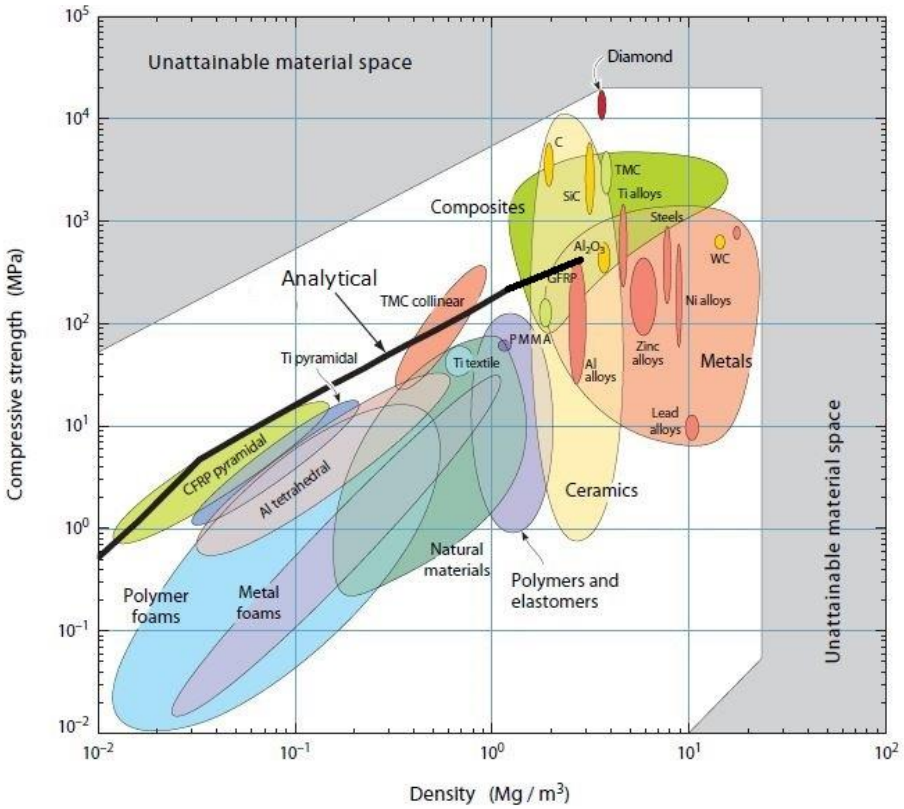

Figure 1.4: Compression strength versus density material chart (Ashby, 2010)

1.3 Application of Corrugated Core Sandwich Structure

Briefly, the utilization of corrugated core sandwich structures has increased extensively in most engineering applications, such as marine structures (e.g., naval ships and combatant deckhouses) (Liang et al., 2001, St-Pierre et al., 2012), public transportation (trains and car bodies) (Ji et al., 2015), aerospace structures (Rejab and Cantwell, 2013), civil engineering (Vaidya et al., 2015), and the packaging industry (Dayyani et al., 2015). This is due to their superior mechanical behaviours, such as their lightweight relative to their size (Huang et al., 2017) and high stiffness-to-weight ratio (Mohammadi et al., 2015, Kazemahvazi and Zenkert, 2009, Bartolozzi et al., 2014).Figure *1.5* shows different corrugated core sandwich structures in various engineering applications.

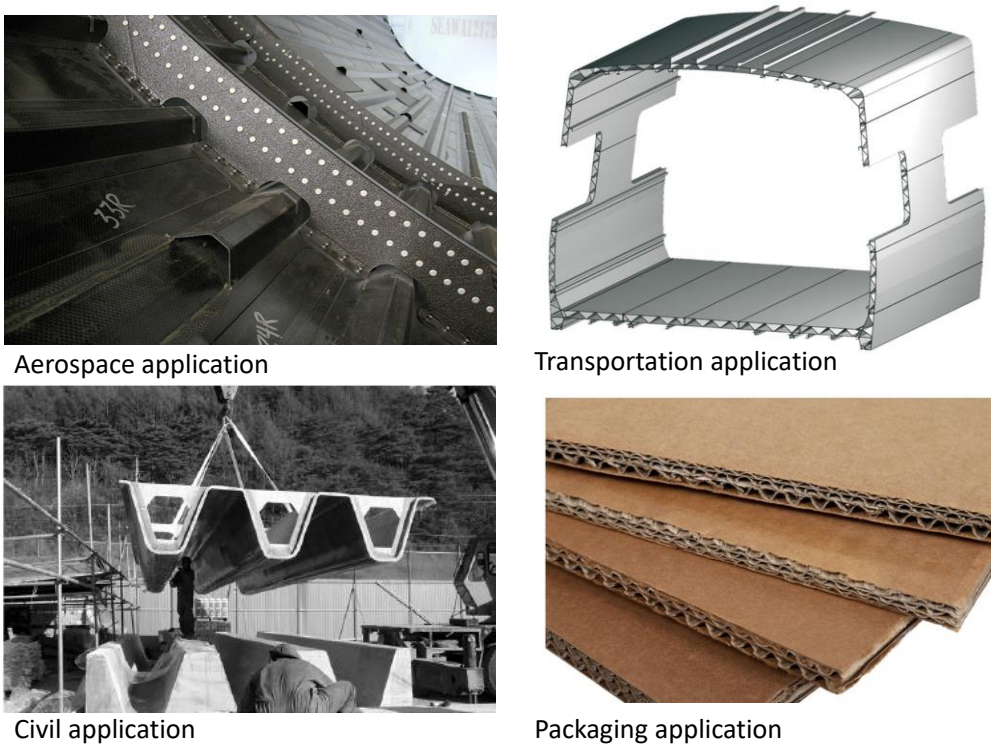

Figure 1.5: Application of corrugated core sandwich structures in several engineering applications (www.images.app.googl/ir)

1.4 Research gaps

Corrugated core sandwich structures i.e. metallic and composite, have been researched for many decades. However, extensive literature based investigation has shown a significant gap in the knowledge base. Lack of detailed design procedures and availability of standardized testing or proofing methodologies have negatively influenced the development of these smart structures. Specifically fibre composite based corrugated research was largely overlooked. The design and fabrication of fibre reinforced composite: single-cell, multi-cell, full-scale, and hybrid composite TCS structures are yet to be introduced. The complete structural behaviour has to be closely investigated. The critical factors governing the structural behaviour such as the influence of support conditions (CD and MD) and performances of TCS structures under quasi-static compression load condition was not clarified. In addition, most influential and important factors such as core geometrical parameters, i.e. core thickness, height, and the short span on the mechanical behaviour have not been investigated. Moreover, damage mechanism of TCS structures under low-velocity impact never been reported. A critical design tool such as a correlated FEA model of a TCS structure under quasi-static and low-velocity impact and determination of an

optimized geometry of trapezoidal composite core under quasi-static condition is not available. Due to the continuous development of new smart composite materials, currently an emerging need for a hybrid TCS structure, which can be replaced many inefficient traditional core structures is required. This thesis will address these issues quantitatively and qualitatively in a well-planned experimental & numerical frame work.

1.5 Project Objectives

A large number of studies have been done on corrugated core sandwich structures for the last four decades to improve their efficiency. These prompted the development of innovating core structures for many engineering applications. The researches to date have tended to focus on metallic corrugated core sandwich structures. However, there is very little published research on trapezoidal corrugated core sandwich structures made of novel materials such as fibre reinforced composites and hybrid derivatives. Furthermore, optimisation for structural efficiency has not sufficiently focused on core topology to improve structures' strength-to-weight factor. Thus, the objectives of the research are:

- Design and fabrication of several new structures of trapezoidal composite corrugated core sandwich (TCS) structures. Woven E-glass fibre reinforced epoxy composites are used in the fabrication of the TCS structures.
- Investigation of the failure mechanism of these TCS structures under different quasi-static and low-velocity impacts.
- Modelling and simulation of the suggested novel TCS structures under different load conditions.
- Numerical optimization of the geometry of the trapezoidal composite corrugated core under quasi-static compression loading conditions.
- Investigation of the low-velocity impact behaviour and failure modes of a novel trapezoidal composite corrugated core, hybridized with high-performance fibre, using the optimized core.

1.6 Scope of the Work

The proposed research focuses on understanding mechanical behaviour, the failure mechanism, and the energy absorption of TCS structures under quasi-

static compression with low-velocity impact loading conditions. Therefore, the research scope of this research is summarized as:

- Manufacture prototype specimens of the TCS structures by woven E-glass/fibre reinforced epoxy composite using wooden moulds.
- Analyse the influence of varying support positions on the mechanical behaviour, failure mechanism, and energy absorption capability of the TCS structures under quasi-static compression. For this investigation, loads are imposed on TCS structures laid on different support positions along the longitudinal and transverse directions. The impact responses of different designs of the composite sandwich core are then investigated and discussed. The failure mechanisms in TCS structures under quasi-static and impact loads are also portrayed. In addition, low-velocity impact loading is performed on single-cell and multi-cell TCS structures.
- Develop numerical models to simulate the quasi-static/low-velocity behaviour of the TCS structures using finite element (FE) models.
- Analyse the impact behaviours at full-scale of different core designs of TCS structures under low-velocity impact at a high level of energy impact.
- Investigate and evaluate the impact behaviour and damage modes of the trapezoidal composite corrugated core by hybridising it with armoured and high-performance synthetic fibres, such as kevlar and zylon, under low-velocity impact.

1.7 Thesis Outline

This dissertation consists of seven chapters, which are outlined in the following:

Chapter 1- Introduction: This chapter outlines the background and significance, aim, research gap, and research objectives of the thesis.

Chapter 2- Literature Review: Here an overview of composite core sandwich structures is presented, including industrial applications and a summary of the previous research on corrugated core sandwich structures.

Chapter 3- Experimental Procedure: In this chapter, the manufacturing of the laminate composite and novel TCS structures is described. It also includes the

experimental set-up of the performed testing, such as coupon tests, quasi-static compression tests, and low-velocity impact testing on the TCS structures.

Chapter 4- Results Discussion: This chapter presents the findings of several tests. The coupon tests measured the mechanical properties of the composite laminate. In addition, the mechanical behaviours and damage mechanism of single-cell TCS structures are evaluated under quasi-static compression loadings. Low-velocity impact testing investigated the impact response of single-cell and multi-cell TCS structures. Several external factors of the impact, such as impactor weight, are presented here.

Chapter 5- Finite Element Simulation: The experimental results given in Chapter 4 are demonstrated using the FE model in this chapter. Here, the quasi-static behaviours of the TCS structures are analysed using ANSYS implicit code. The trapezoidal composite corrugated core is also optimised utilizing the FE model. The impacts of the TCS structures are simulated by explicit ANSYS-Workbench code. The effect of impactor head and weight is explored by investigating the impact behaviour of TCS structures under low-velocity impact.

Chapter 6- Case studies: This chapter involves two case studies. The first studies the impact behaviour of different full-scale TCS structures under low-velocity impact at a high level of energy impact. The second studies the effect of hybridization of the trapezoidal composite corrugated core with aramid and high-performance fibre on the impact behaviour and damage mechanism under low-velocity impact.

Chapter 7- Conclusion: A summary of the previous chapters is presented here. Several benchmarking findings are drawn concerning TCS structures' enhancements. Finally, some future lines of investigation are also recommended.

1.8 Summary

This chapter gave a summary of the research project, including its background, aim and objectives. The research framework and scope of the project were presented, together with the thesis structure.

Chapter 2

Literature Review

2.1 Introduction

This chapter discusses the utilization of sandwich structures in several engineering applications. It also gives an overview of the varieties of sandwich structures with metal and composite corrugated cores, and the essential performance attributes of composite corrugated core sandwich as a replacement for conventional sandwich structures. In addition, it includes a literature review that highlights the investigation of the mechanical behaviour, failure mechanisms, and energy absorption of such sandwiches under compression and low-velocity impact conditions. Furthermore, this chapter aims to identify the research gaps concerning composite corrugated core sandwich structures, deduced from the limitations of the previous studies.

2.2 Applications of the Sandwich Structures

Corrugation core sandwiches have been used in several applications depending on design requirements and sandwich materials. These are discussed according to application in various industries in the following sections.

2.2.1 Packaging industry

In 1856 the first design for cardboard was patented in England (DeLassus et al., 1997). Initially this cardboard, made from paper, was used in hat fabrication. Then cardboard was developed for packaging pottery and glass containers. Nowadays, corrugated boards are used widely to fabricate rigid shipping boxes of almost any size and shape; the base materials are either of paper or plastic. It is worth mentioning that there are several reasons corrugated sandwich is utilized extensively in the packaging industry, such as its lightness, stiffness, cost effectiveness, durability, environmental sustainability, and recyclability (Twede et al., 2014, Dayyani et al., 2015). During

transport and storage, packaging containers are exposed to different load circumstances, such as shock load due to drop-down, composite load in stacking, and vibration load. Therefore, they should possess appropriate mechanical behaviours to sustain all these external conditions.

2.2.2 Transport applications

Sandwich technology has been widely used in locomotives and automobiles since the end of the last century, in cars, buses and train bodies, due to their high strength and effective energy absorption of an impact incident. Moreover, reducing noise and pollution in high-speed trains is an essential aim for designers and this was achieved by using lightweight core sandwich structures. This lighter weight reduces fuel consumption, thus lowering air pollution and global warming. For example, in the Shinkansen-700 series (also known as bullet trains) the low noise and low vibration corrugated core sandwich superstructure in the train body reduced noise to a minimal value (Matsumoto et al., 1999). Sandwich structures were also used in Australian XPT, the Swiss 2000, the French TGV, and the ETR 500 locomotives in Italy (Vinson, 2005).

2.2.3 Marine applications

Corrugated sandwich structures have provided a potential solution to shipboard design problems and naval construction. Their lightness in weight assisted with fabricating several ship areas, such as bulkheads, decks, hatches, and modular accommodation (Knox et al., 1998). In addition, due to a high resistance to shock wave and blast load, the application of such sandwich structures has increased in combatant deckhouse frames of naval vessels (Liang et al., 2001). For example, the laser beam welded corrugated core (LASCOR) provided a weight reduction of between 15% and 30% for fabricated naval structures.

2.2.4 Aerospace applications

One of the newest engineering applications of the corrugated core sandwich is morphing wings. Recently, corrugated core sandwich structures started to be used in aircraft wings as a stabilizer (Winkler, 2012). This is because these structures exhibit high flexibility in one direction and high stiffness in the next direction (Dayyani et al., 2015). Moreover, corrugated core sandwich panels possess the capability of

undergoing recoverable strain and considerable deformation. Furthermore, the deformability of these corrugated sandwich cores can achieve significantly high levels, particularly for the highest elongation in the morphing direction, evaluated under principal tensile loading. Their multifunctional characteristics mean that such sandwich structures are now used in aerospace. For example, these panels offer insulation, which helps to protect the spacecraft from excessive re-entry temperatures (Bapanapalli et al., 2006).

2.3 Base materials of sandwich structures

2.3.1 Metal sandwich structures

Several materials have been used in the manufacturing of the sandwich structures. Initially, metals such as steel, aluminium, brass, and aluminium alloy were used to meet various engineering applications (Wang et al., 2003) (Wadley, 2005). Consequently, most previous researchers have examined the mechanical behaviour, damage mechanism, and energy absorption of these metal sandwich structures. For example, Zhang et al. (2013b) investigated the compressive strengths and dynamic response of foam filled and unfilled cores of stainless steel sinusoidal core sandwich structures. They concluded that the foam filled could considerably enhance these sinusoidal core structures' normal compressive strengths, while under impact load conditions it has no noticeable effect on structural strengthening.

Dharmasena et al. (2013) examined the dynamic deformation of a pyramidal truss core sandwich and monolithic plates made from stainless steel with equal mass. The sandwiches loaded by the spherically expanding shells included water-saturated sand and dry sand. They pointed out that the mid-span deflection of the rear faces of the corrugated sandwich is substantially more than that of the corresponding monolithic steel plate. In another study, Bartolozzi et al. (2015) validated analytic models of homogenization of aluminium sinusoidal corrugated core sandwich panels by static and dynamic experimental tests. They assumed that the complex geometry of the core deformed as an equivalent homogeneous layer; and they demonstrated that the tested sandwich and FE homogenized models have some differences due to the perfect bonding between the equivalent core layer and panel face sheets. St-Pierre et al. (2015) employed low-velocity impact to compare a steel triangular corrugated core sandwich beam (Figure 2.1) and a Y-frame core sandwich beam. The authors highlighted that both have a similar force-displacement under low-velocity impact. As well, quasi-

static and low-velocity impact responses are very similar, indicating that the structural moment of inertia had no noticeable effect on the tests.

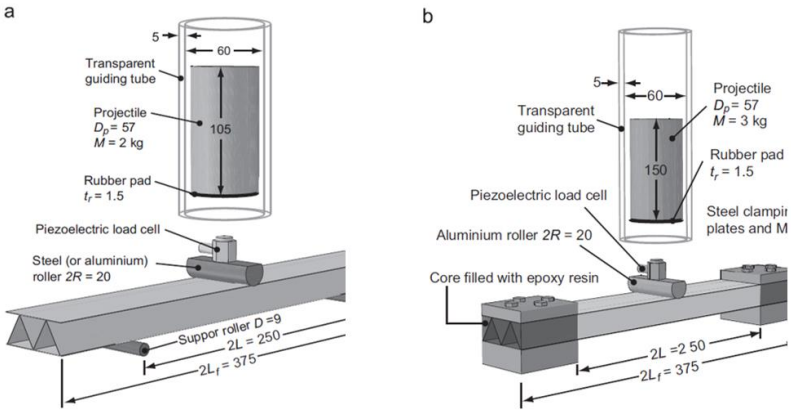

Figure 2.1: Sketch of the experimental set-up used to perform drop-weight tests at 5m/s on Y-beams in (a) simply supported and (b) clamped configurations (St-Pierre et al., 2015)

Kılıçaslan et al. (2013) investigated the deformation and energy absorption of layered (0/90 and 0/0) trapezoidal corrugated aluminium cores under drop-weight testing using spherical, flat and conical end strikers, as seen in Figure 2.2. They observed that the sandwiches were not penetrated by the flat and spherical impactor heads, and the 0/90 sandwich experienced a somewhat higher load deformation and energy absorption than the 0/0 sandwich. In contrast, the conical impactor head caused penetration/perforation of the sandwiches.

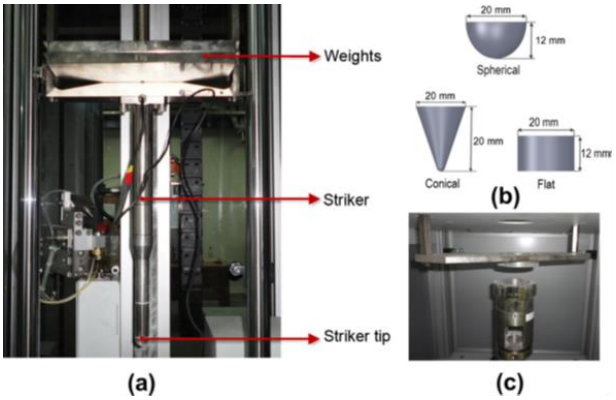

Figure 2.2: Drop-weight test system and parts: (a) impact set-up, (b) striker tips and (c) specimen holder rings (Kılıçaslan et al., 2013)

Wadley et al. (2013a) investigated the impact damage of a corrugated core sandwich made of extruded 6061T6 aluminium alloy. They observed a complete penetration of the impacted area of the upper face sheet (due to shear force), core fracture (due to stretching), bending and tensile of the core struts, followed by back face sheet damage (due to shear-off). In another study, (Wadley et al., 2013b), they performed a low-velocity impact to investigate the influence of a core topology of hybrid aluminium sandwich on the impact response. They found that triangular corrugated core structures have an acceptable impact resistance, and the impact behaviour is enhanced with a prism core. In other work (Boonkong et al., 2016) researchers considered the failure mechanisms of a curvilinear corrugated core structure under low-velocity impact. They noted that the failure took three forms: denting and stretching of the top skin and core buckling of the structure (at low energies), while higher impact energies caused core and skin damage localised to the impact point. Zhang et al. (2016a) tested fully clamped aluminium metal foam sandwich beams to investigate their energy absorption under quasi-static compression and correlated this with a numerical model. Their results revealed that the energy absorption of the asymmetric sandwich beams with an aspect ratio of the upper to lower face sheet ≥ 1 is better than that when it is < 1. To investigate its energy absorption capability Liu et al. (2017a) conducted an impact test on an aluminium foam core sandwich panel with skin specimens of metal fibre laminate. They concluded that an increase of skin thickness improves energy absorption, while an increase in core thickness (aluminium foam) has no effect on the energy absorption.

Recently, Zhao et al. (2018) employed experimental, numerical, and analytical approaches to perform out-of-plane compressive loading on the Ti-6Al-4V sandwich system with corrugated channel cores, as seen in Figure 2.3. The authors reported that the peak strength depends upon the structure's relative density, and they also stated that after peak strength, the core webs continue softening, associated with extensive plastic deformation and core fracture.

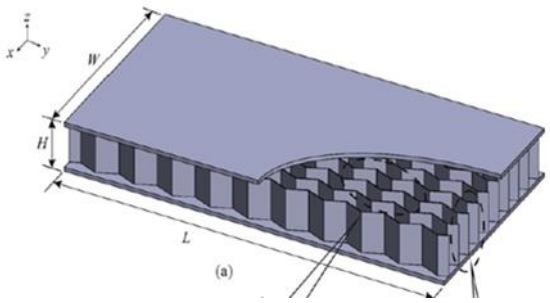

Figure 2.3: Schematic of a sandwich panel with triangular corrugated channel core (Zhao et al., 2018)

Qin et al. (2018) investigated the low-velocity impact behaviour of a corrugated triangle core filled with aluminium metal foam, correlating the experimental tests with a finite element model. The authors suggested that the low-velocity impact behaviour of the sandwich is not affected by the strain hardening of folded plate and face sheets. Under high-speed impact, the damage mechanisms and deformation of metal alloy honeycomb sandwich panels were studied (Xie et al., 2018). These researchers reported that the perforation mechanism is controlled by the shaped plug formation, producing compression/shear failure mode in the impacted zone.

From the literature, it can be concluded that researchers have extensively investigated metal sandwich structures, and there is abundant knowledge about this kind of structure due to the isotopic mechanical behaviour of its base materials. However, the major problem with these metal sandwich structures is their heavy weight, which is a barrier to their use in specific applications that required lightweight yet high strength/stiffness materials. On the other hand, composite materials are fast becoming key in the fabrication of sandwich structures; therefore, the researcher started to investigate the new generation of composite sandwich structures which do not use metals.

2.3.2 Composite sandwich structures

Structural efficiency is an indication of stiffness/strength relative to lightness in design. The structural efficiency of sandwich structures can be maximised by developing and optimizing their core geometry or utilizing the most efficient light material in their fabrication. Therefore, the innovation of fibre reinforced polymer (FRP) composite materials significantly replaced most of the metals previously used for sandwich

structures. These materials are characterized by a high specific strength/stiffness-to-weight ratio (Kazemahvazi et al., 2012), low density (Francesconi and Aymerich, 2018, Li et al., 2016, Sun and Hallett, 2018), fatigue properties and corrosion resistance. Consequently, in recent years, there has been an increasing interest in the investigation of these FRP composite sandwich structures.

2.4 Composite sandwich - core topology

2.4.1 Stochastic core

Closed-cell foam and open-cell foam cores (stochastic core) are used in the fabrication of sandwich structures. The mechanical properties of such sandwiches are considered to be isotropic due to their similar out-of-plane in the plane direction (Wahl et al., 2012). Foam core composite sandwiches have been extensively investigated (Anderson and Madenci, 2000), (Schubel et al., 2007), (Zangani et al., 2008), (Leijten et al., 2009), (Bezazi et al., 2011), (Feng and Aymerich, 2013), (Ude et al., 2013), and (Yashiro et al., 2014). Recently, Sakly et al. (2016) used a foam core with glass fibre epoxy skins, Walsh et al. (2017) used polmethacry-limide (PMI) foam between carbon fibre skins. Morada et al. (2017) examined a ATH/ epoxy core to investigate the low-velocity impact on the sandwich panel. However, such types of sandwich cores (stochastic foam) are considered to be conventional (Torre and Kenny, 2000). Therefore, this work focuses on composite periodic core sandwich structures.

2.4.2 Periodic core

In addition to the core materials, the core topology is one of the dominating parameters that affect the mechanical behaviour, failure mechanism, and energy absorption capacity of sandwich structures (Wadley et al., 2013b). The periodic core outperforms the stochastic core sandwich, particularly in core deformation, compressive strength, and energy absorption (Mueller et al., 2019). Therefore, researchers have investigated different periodic core geometric topologies under out-of-plane and impact/dynamic conditions. This is because such composite periodic core sandwiches are susceptible to out-of-plane and impact events during their service lives, such as tool drops by maintenance staff, bird strikes, handling in equipment/service vehicles and hailstorms (Liu et al., 2017b). In addition, their impact/dynamic incident parameters are still a critical issue (St-Pierre et al., 2015, Zenkert et al., 2005). The mechanical behaviours,

failure mechanism, and energy absorption capability of composite periodic core sandwich structures have received considerable attention, as is outlined in Section 2.5.

2.5 Mechanical behaviour of composite sandwich structures

Composite sandwich structures provide an extensive range of benefits over conventional sandwich cores, and their use in engineering applications is continuously increasing. Therefore, many researchers have investigated their strength/stiffness and deformation under miscellaneous loading conditions, such as out-of-plane compression load and low-velocity impact, as well as using several sandwich analytic theories. Thus, this literature review aims to reveal the broad spectrum of the recent investigation into the mechanical behaviour of composite sandwiches under various loading conditions.

Besides traditional foam sandwiches, honeycomb core sandwiches have been developed and examined due to their potentially useful mechanical behaviours. For example, Park et al. (2012) investigated the impact/dynamic response of composite square honeycombs under high-velocity impact using the Kolsky bar. The authors mentioned that the impact peak force of the core honeycomb sandwich was about one third that of the parent materials. Gholami et al. (2016) optimized the design of a honeycomb core composite sandwich panel employing a particle swarm optimization technique under out-of-plane load. This revealed that the optimal honeycomb sandwich panel could be achieved with a high number of thin, tall cells. In another study, Yellur et al. (2019) compared a composite honeycomb sandwich with a plywood sandwich, finding that the honeycomb composite provided better impact behaviour. Liu et al. (2019) numerically studied and compared the impact response of a tube filled honeycomb core with honeycomb sandwich panels under low-velocity. The authors stated that the tube filled honeycomb has smaller rear face sheet displacement and higher impact resistance compared to the latter.

In the literature, the concept of lattice truss and the pyramidal sandwich was also offered as another type of cellular core sandwich structure to raise the sandwich strength-to-weight ratio (Wadley et al., 2003). For example, Xiong et al. (2012) studied the impact behaviour of a pyramidal core sandwich structure with two-layer composite core under impact loading. They pointed out that the peak load associated with a complete failure of the truss core is due to the core buckling, as seen in Figure 2.4.

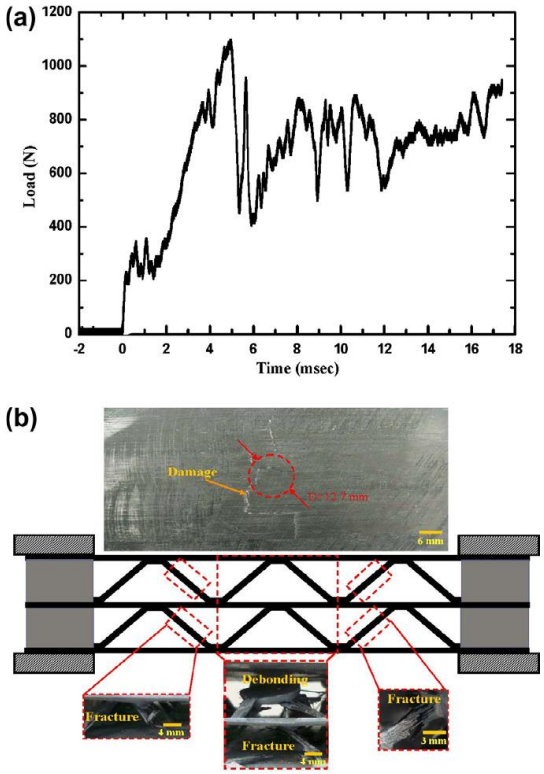

Figure 2.4: Low-velocity impact of a two-layer sandwich panel at 20 J (a) Impactor load-time and (b) Photographs of top face sheet and truss cores after impact (Xiong et al., 2012)

Gao et al. (2013) strengthened the mechanical properties of composite pyramidal truss cores by a hot-press moulding method, finding that this method enhanced core bars to delay the local failure progress of the sandwich. Song et al. (2015) carried out compressive out-of-plane tests on a composite sandwich structure with a stitched lattice core, suggesting that the composite sandwich structure showed a linear-elastic response until lattice failure. Djama et al. (2019) evaluated the mechanical properties of a composite truss core sandwich under out-of-plane compression and in-plane shear tests, then compared the results with the numerical model. Results showed that the composite truss core sandwich had similar specific compressive and shear strengths compared with a few common lightweight structures; the numerical model confirmed a similar response. Sugiyama, Matsuzaki [50] conducted three-point bending tests on various core shapes of 3-D printed composite sandwich structures. They found that the maximum load and flexural modulus increased with increases in the effective density for all composite core geometry.

Several investigators have considered other core configurations. For example, Fan et al. (2010) carried out quasi-static compression tests on a woven textile sandwich. Their results showed that, due to the tilting of fibre piles within the web, the quasi-static compression induces core shear deformation, and core densification appeared at the end of the compression stage. In another study, Fan et al. (2011) investigated the mechanical behaviour of composite multi-layered woven textile sandwich panels. They pointed out that the core laminae of a multi-layered sandwich experience strength failure that leads to increase sandwich compression resistance before the densification of the core. Schultz et al. (2011) experimentally and numerically investigated the buckling behaviour and failure modes of fluted composite core sandwich structures under compression load. Their results showed that structural local buckling causes core failure and this failure increases with increasing post-buckling load. Liu and Turner (2017) carried out experimental quasi-static and dynamic compressive tests to investigate the response of a triangle composite carbon corrugated core sandwich. They used a unidirectional carbon fibre pre-impregnated lamina to fabricate the wrapped corrugated core, by wrapping CFRP around destructible triangular prisms. The researchers suggested that the wrapped composite cores show rate dependent behaviour relative to the dynamic speed.

In the term of hybrid sandwich structures, Odacı et al. (2012) investigated the collapse stress of composite E-glass polyester with a fin aluminium corrugated core sandwich under low-velocity impact. They observed that large fin corrugated cores (i.e., maximum core height) have relatively lower collapse stresses than small fin corrugated cores. Zhang et al. (2013a) tested hybrid pyramidal truss core sandwich structures made from carbon FRP face sheets and aluminium alloy cores under quasi-static compression and low-velocity impact. The authors concluded that under compression tests, the stress-strain curve has a long plateau and the sandwich energy absorption enhances at increasing core relative density, while under low-velocity impact, the peak force and contact time increases with increasing core relative density. Hou et al. (2014) carried out flatwise compression on composite graded conventional kirigami sandwich panels, suggesting that the graded core configuration offers higher compression capabilities against honeycomb sandwich panels. In other experiments, Liu et al. (2017b) investigated the effect of three different impactor shapes on mpact behaviour of a hybrid corrugated core sandwich under low-velocity impact. The upper face sheet of the corrugated structure was fabricated from CFRP combined with a

corrugated aluminium core. Results indicated that the flat impactor head produces the maximum force and shorter impact time. Rong et al. (2018) investigated the influence of geometric configurations of a hybrid sandwich made of corrugated aluminium cores and composite skins on impact behaviour. They found that sinusoidal and arc-shaped core sandwiches have a lower compression strength/stiffness compared to triangle and trapezoidal corrugated cores.

Composite corrugated core sandwich structures have received their share of attention in the literature. Kazemahvazi and Zenkert (2009) investigated the shear modulus of composite corrugated cores under a quasi-static compression load, pointing out that the maximum shear modulus can be obtained at a 45^{o} angle to the core. Zhang et al. (2013c) improved the bending strength of a trapezoidal composite corrugated sandwich composite structure under a quasi-static compression load. They found that an increase of core thickness enhanced the specific bending strength of the sandwich structure while increasing the contact length between the core and upper face sheet led to a decrease in the specific bending strength. Jin et al. (2013) experimentally investigated the mechanical properties of a woven corrugated sandwich composite under a quasi-static compression load, observing that slow core crushing and contact with the upper and lower face sheets generated a ductile load-displacement response associated with a long deformation plateau.

Russell et al. (2010) carried out high-velocity impact tests on unfilled and foam filled glass fibre composite corrugated core structures. The experimental tests were performed by the Kolsky bar on both the parent material and the corrugated system. The authors noted a linear increase of the peak stresses of both the strut wall material and corrugated cores at a low strain rate, as shown in Figure 2.5. They suggested that this increase is due to the strain rate sensitivity of the composite matrix material that stabilized the glass fibre composite micro-buckling failure mode. In contrast, at high strain rates, the peak stresses exhibited no sensitivity to glass fibre compressive crushing.

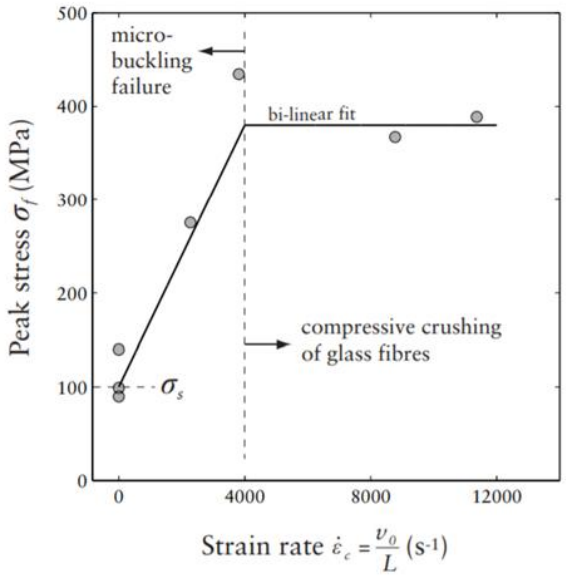

Figure 2.5: Summary of the measured peak stresses of glass fibre corrugated core sandwich as a function of applied strain rate (Russell et al., 2010)

Kazemahvazi et al. (2012) investigated the impact behaviour of two inclined struts mad from carbon/fibre reinforced epoxy to represent corrugated core sandwich. Three types of core aspect ratio were tested under a quasi-static compression load up to a high-velocity impact of 200 ms^{-1} using a Kolsky bar set-up. The authors reported that increasing the compressive load rate leads to a significant enhancement of the sandwich impact strength. The inertial stabilization of the core members also has a pronounced effect on the strength enhancement and impact resistance of the core struts. Schneider et al. (2015) investigated the impact behaviour of a self-reinforced poly (ethylene terephthalate) SrPET composite corrugated core panel under high-velocity impact. They noted that the SrPET composite corrugated core sandwich exhibited a significant rate dependence, which is generally attributed to micro inertial stabilization of the web and high plastic tangent stiffness of the SrPET material. The authors also concluded that the SrPET corrugated sandwich, under a quasi-static and dynamic loading, has a similar performance to commercial polymeric foams.

Furthermore, a number of studies have attempted to develop an analytical model to investigate the mechanical properties of corrugated core sandwich structures. For example, Kazemahvazi and Zenkert (2009) developed an analytical model for the compressive and shear response of monolithic and hierarchical corrugated core sandwich, and they compared with finite element. Xiong et al. (2010) established an analytical model to study the crush response of composite sandwich core and

compared with experimental results, and they mentioned that this model could be modified for other sandwich structures. In another study, Rejab and Cantwell (2013) modified a mechanical formula to predict the compression strength of a corrugated core sandwich. They found that the analytical model gives over estimate outcomes in comparison with experimental and finite element results. However, due to the overestimate outcome of the analytical model and complexity of the corrugated sandwich structures most of the researches have tried to simplify the analytical models. Therefore, in this study the author only indicated to the analytical model in the appendix A.

Generally, most of the composite sandwich structures failed at post-loading conditions; therefore, the failure mechanism attracted the scrutiny of researchers. The next section presents previous work focused on the failure mechanism of the composite sandwich structures.

2.6 Failure mechanisms of composite sandwich structures

Disclosure of damage in sandwich panels is paramount for their engineering application. According to the literature, the failure mechanism of such sandwich structures generally comprises three basic damages: face sheet damage, core crush, and a combination of the two. Most metal sandwich structures show external damage on the face sheet at exposure to impact/dynamic load (DeFrancisci et al., 2012). For example, Zhang et al. (2016b) found a complete tearing mode of the front face, and petalling failure of the back face of a steel corrugated core sandwich subjected to air blast loading. However, the damage in composite sandwich structures is quite distinct to that of metal sandwich structures (DeFrancisci et al., 2012). Due to composite materials' brittleness, such composite sandwich structures tend to have internal micro-damage of the face sheet and core crushing under similar loadings compared to metal sandwich structures. Therefore, the researcher focused considerably on the damage mechanism of the composite core sandwich.

Numerous studies have been carried out on the damage mechanism of composite core sandwich structures. For example, Herup and Palazotto (1998) identified the initiation of damage of a graphite/epoxy honeycomb sandwich as a function of the thickness face sheet and loading rate. They concluded that the load damage initiated under a quasi-static test is lower than that of low-velocity impact tests, and this discrepancy rose with increasing the thickness of the sandwich face sheets. Anderson

and Madenci (2000) considered the effect of low-velocity impact on the damage mechanism of different foam and honeycomb sandwich structures. Their results revealed that the surfaces of both the foam and honeycomb sandwiches show very little fracture at the same levels of impact energy. Othman and Barton (2008) investigated the failure initiation and propagation characteristics of composite honeycomb sandwich panels under quasi-static and impact/dynamic loadings. Both experiments revealed penetration and perforation of the honeycomb panel involving upper skin compression failure, core crushing, and tensile failure and perforation of the lower face sheet. Sakly et al. (2016) measured the damage resistance of a composite foam sandwich under low-velocity impacts. The authors identified delamination and fibre breakage in the composite skin, core/skin de-bonding, and core crushing modes. Chen et al. (2017) numerically investigated the damage mechanism of honeycomb composite sandwich structures under low-velocity impact and compared them with experimental tests. They pointed out that the numerical model showed the key perforation mechanisms and associated damage patterns of the sandwich quite well. Farshidi et al. (2019) numerically and experimentally investigated dis-bond damage propagation in composite honeycomb core sandwiches. They found that the variation in both the crack length and face sheet thickness of the sandwich potentially affects the energy release rate value during the damage event.

In addition to foam and composite honeycomb core sandwich, Xiong et al. (2012) studied the failure mechanism of two-layer carbon fibre composite sandwiches with pyramidal truss cores under quasi-static and low-velocity impact loads (Figure 2.6). Their conclusion was that under a quasi-static load, the peak load is accompanied by damage of the entire individual truss layers; this is either due to buckling of core struts or crushing struts. By way of comparison, under a low-velocity impact test, the failure results from load concentration of the impactor head on the upper skin.

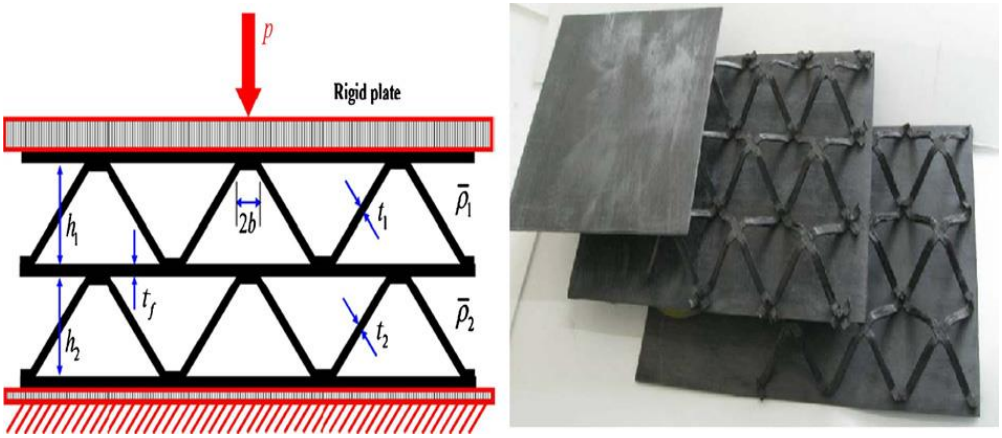

Figure 2.6: (a) Schematic diagram of the quasi-static compression test assembly at a cross-section of 45^o and (b) Carbon fibre sandwich panels with two-layer pyramidal truss cores (Xiong et al., 2012)

Zhang et al. (2013a) tested hybrid pyramidal truss core sandwich structures made from carbon FRP face sheets and aluminium alloy cores under quasi-static compression and low-velocity impact. They found that under compression tests, the buckling of truss members usually occurs, while matrix cracking, delamination of the face sheets, and buckling of the core truss are predominant in the impact tests. Haldar et al. (2018) identified core crushing and local de-bonding damage between an egg-box core cell and sandwich skin as the major failure modes under quasi-static and low-velocity impacts, respectively. Ye et al. (2020) fabricated two variants of pyramid truss sandwich using 3-D printing technology to investigate their failure modes under out-of-plane conditions. They pointed out that the three post failure modes of such printed lattice truss structures comprise core deforming, strain hardening, and softening of the core strut. The mechanisms for failure of composite, foam, honeycomb and pyramidal truss core sandwiches have been explored in a myriad of ways, with various results as presented above.

In the term of composite corrugated core sandwich, Kazemahvazi et al. (2009) experimentally investigated the failure mechanism of a hierarchical corrugation core made of prepreg unidirectional carbon fibre SE-84LV, tested under compression and shear loading conditions. In this study, the authors observed four different damage types: general buckling, shear buckling, local buckling, and face fracture. Schultz et al. (2011) experimentally and numerically investigated compression behaviour (buckling behaviour) and failure modes of composite fluted corrugated core structures.

They suggested that the material's strength failure results from local structural buckling, and this strength failure will escalate through increasing the post-buckled range of loading. Moreover, non-destructive inspection of the impact damage areas showed just one damage flute on either side of the impact region. He et al. (2016) experimentally and numerically investigated the damage mechanism of a hybrid sandwich structure fabricated from an aluminium corrugated core and CFRP face sheets under low-velocity impact. Results showed several types of failure modes: fibre damage, matrix damage, and delimitation of the sandwich skin, in addition to core damage.

Recently, Liu and Turner (2017) investigated the quasi-static and low-velocity impact responses of triangle wrapped composite carbon corrugated core sandwiches. They used unidirectional carbon fibre pre-impregnated lamina to manufacture the corrugated core by wrapping CFRP around destructible triangular prisms. The authors concluded that under a quasi-static test, the failure of the composite core increased as part of the core unwrapped due to the core not being laterally confined and also to matrix cracking at the joints of the core struts and upper face sheet. Under impact tests, the cores struts exhibited a rate dependent response which led to core crush. Yu et al. (2018) analysed failure modes of an adhesively bonded corrugated core sandwich, finding that the adhesive thickness affects stress distribution in the adhesive layer and increasing the glue strength decreased the failure zone. Vignjevic et al. (2019) compared a composite sinusoidal corrugated core and tube core sandwich with a traditional composite foam sandwich, suggesting that the two former sandwiches are considerably more damage resistant than the latter.

The mechanisms for failure of composite corrugated sandwiches have been explored in a myriad of ways, with various results as presented above. Usually, damage of composite sandwich structures is caused by an absorption of the applied energy, particularly under an impact event. As a result, in the next section the energy absorption capability of such sandwiches is considered.

2.7 Energy absorption of composite sandwich structures

Because corrugated composite sandwiches are vulnerable to impact events by foreign bodies, many innovative improvements have been made, including an increase in their energy absorption capability. Prior to this, several kinds of impact tests were performed. Dear et al. (2005) investigated the energy absorption susceptibility of two

different composite honeycomb sandwiches under low-velocity impact, concluding that an increase in the fibre ratio in the sandwich face sheet leads to increased energy absorption. Xiong et al. (2012) compared two-layer sandwich panels of continuous carbon fibre truss core and woven glass fibre textile truss core, and noted that the former has a similar or better energy absorbing capability per unit mass. Ivañez and Sanchez-Saez (2013) developed a numerical model to investigate the low-velocity impact response of a composite honeycomb sandwich beam. Results were that the energy absorption of the composite sandwich was controlled by the core at the low-velocity impact, while with increasing impact velocity, the face sheets of the sandwich were more involved.

Recently, Schneider et al. (2016) developed a finite element model to predict the energy capability of a self-reinforced poly (ethylene terephthalate) composite corrugated sandwich beam under a quasi-static bending load condition and validated this against the experimental test. Both approaches considered the energy absorption. This work revealed that the performance of such a composite core outperforms other composite materials in terms of flexural energy absorption. Morada et al. (2017) investigated the low-velocity impact resistance of ATH/epoxy core sandwich composite panels. This research evaluated sandwich panel performance in terms of their energy absorption capability and impact damage resistance. The composite sandwich absorbed about 50% of the impact kinetic energy, and the ATH/epoxy core enhanced the face sheet damage tolerance. In another study, Sang et al. (2019) manufactured three different composite honeycomb sandwich structures of circular, hexagonal, and re-entrant cores by using a 3D printer to investigate the effect of the core shape and relative density on the energy absorption capability. They pointed out that the circular honeycomb sandwich exhibited poor energy absorption, while the other two honeycomb structures (hexagonal and re-entrant core shapes) showed high load bearing and energy absorption. It can be concluded that the energy absorption capability is still the key question in the innovation of a composite sandwich structure.

2.8 Trapezoidal composite corrugated core sandwich structures

As explained in the literature, several composite sandwich designs have been extensively investigated and applied in engineering applications. In addition to improving the face sheets, most sandwich developments aimed to improve the core

functionality by increasing the core's ability to carry, transfer, and distribute the applied loads.

Among all composite sandwich structures, however, the relative importance of the corrugated core sandwich (periodic cellular structures) has also been subject to research due to several reasons. For example, corrugated core sandwiches are replacing the traditional equivalent relative density foam core sandwich panels due to their offering greater stiffness and strength under structural loading (Evans et al., 2001, Queheillalt and Wadley, 2005). In addition, these sandwich structures have different mechanical behaviour, i.e., high stiffness in the longitudinal direction relative to the transverse (the direction perpendicular to the machine direction) (Dayyani et al., 2013). This has made the corrugated core sandwich play an important role in comber morphing air-foils by their superior aero-elastic performance, changing their shape, and withstanding aerodynamic and external loads (Mohammadi et al., 2015) (Winkler and Kress, 2010). Their characteristic of multifunctional applications (Côté et al., 2006) which offers the ability to protect minor instrumentation laid inside the corrugated core sandwich cavities, has also motivated the researchers to investigate their mechanical properties. Furthermore, a high deformation shape under external force with zero Poisson's ratio (Huang et al., 2016) is another reason that made the corrugated core sandwich structures in the sights of researchers.

Another notable characteristic of corrugated core sandwiches is their high resistance to impact loading and their dissipation of massive kinetic energy compared to uniform plates (Zangani et al., 2008). However, as yet, there is limited literature about trapezoidal composite corrugated core sandwich (TCS) structures, particularly comparing their mechanical behaviour in both core and machine direction under quasi-static load conditions. In addition, none of these studies has addressed the design of continuous single-cell, multi-cell, and full scale TCS structures with a hybrid of a high-performance fibre composite core under low-velocity impact. This is the focus of the present research. The relevant works concerning TCS structures are summarized in Table 2.1.

Table 2.1: Summary of relevant research works on TCS structures

Authors	**Core materials**	**Core design and unite cell**	**Testing procedure**	**Investigation**
Kazemahvazi and Zenkert (2009)	Unidirectional carbon fibre composite	Single-cell/ hierarchical corrugated core	Analytical and FE analysis/ static compression and shear test	Compressive and shear modulus
Kazemahvazi et al. (2009)	Unidirectional carbon fibre	Single-cell/ hierarchical corrugated core	Analytical and experimental/ static compression and shear test	Failure mechanisms
Russell et al. (2010)	Woven E-glass composite	Multi-cell triangle foam filled glass fibre composite corrugated	Experimental and analytical/ high-velocity impact up to 175 m/s	Dynamic out-of-plane compressive response
Kazemahvazi et al. (2012)	Unidirectional carbon-Fibre epoxy	Struts of core to represent single-cell	Experimental/ high-velocity impact up to 200 m/s	Compression response
Zhang et al. (2013c)	Carbon and glass fibre composite	Single-cell/ trapezoidal corrugated core	Experimental/ quasi-static compression load	Bending strength
Jin et al. (2013)	Woven textile composite	Multi-cell sinusoidal corrugated core	Experimental/ quasi-static, shearing and three-point bending	Failure mechanisms
Schneider et al. (2015)	Composite materials/ self-reinforced poly fabric	Wrapped single-cell assembled to fabricate multi-cell trapezoidal corrugated core	Experimental/ quasi-static and high-velocity impact	Out-of-plane compression properties
He et al. (2016)	Aluminium core/ composite skin	Multi-cell trapezoidal corrugated core	Experimental/ low-velocity impact	Impact behaviour of the sandwich

Liu et al. (2017b)	Aluminium core/ composite skin	Multi-cell trapezoidal corrugated core	Experimental/ low-velocity impact	Effect of impactor head
Rong et al. (2018)	Aluminium core/ composite skin	Multi-cell trapezoidal corrugated core	Experimental/ low-velocity impact	Effects of core geometry
Vignjevic et al. (2019)	Carbon fibre composite core	Multi-cell sinusoidal corrugated core	Experimental and numerical/ high-velocity impact	Impact behaviour of the sandwich

Therefore, this research work proposes to contribute to the fabrication and the property value of the TCS structure, made from continuous fibre (i.e. not chopped fibre) fibre composite materials. In addition to a quasi-static compression load, a series of low-velocity impact tests at and beyond the visible threshold damage energy are presented. These experiments aim to understand the mechanical behaviour, failure mechanisms, and energy absorption of the single-cell, multi-cell, and full scale of TCS structures. A numerical model using a finite element model is developed to correlate with the experimental test and to predict the stress distribution and optimization of the trapezoidal composite corrugated core. As well as low-velocity impact, the effect of impactor weight is considered.

Moreover, under low-velocity impact, the skins of the composite sandwich structure might show as undamaged to visual inspections despite internal damage being present, which is a serious problem. Such internal damage causes a degradation in the strength and reliability of the composite sandwich. This can be injurious and most often results in an unexpected catastrophic failure of the sandwich. Therefore, enhancement of the composite corrugated core by hybridizing it with high-performance fibre is also an essential aim of this research work. This will contribute to improving TCS structures' impact resistance under low-velocity impact events.

2.9 Summary

This chapter aimed to present a literature review of the most recent relevant research concerning the utilization of sandwich structures in several engineering applications and their specific characteristics. In addition, it contributed an overview of different sandwich structures, in particular, composite sandwich structures, outlining the reasons for their performance in replacing conventional sandwich structures. Furthermore, the mechanical behaviour, failure modes, and energy absorption capability of composite sandwich structures under various loading conditions have been highlighted. Furthermore, this chapter identified the research gaps for trapezoidal composite corrugated core sandwich structures deduced from the limitations of previous studies.

Chapter 3

Experimental Procedure

3.1 Introduction

This chapter presents the technique of fabricating composite specimens, specifically the laminate composite plate and TCS structure. It also describes the design and manufacturing of several moulds to be used in the TCS structure's fabrication. The experimental procedure for quasi-static compression tests on TCS structures, supporting them in both cross direction (CD) and machine direction (MD) is also discussed. This is followed by a description of the experimental procedure for low-velocity impact tests of different designs of TCS structure, at and beyond the visible damage threshold impact energy of the composite materials. It also presents low-velocity impact tests of different impactor weights on a single-cell composite corrugated core sandwich. Finally, details are given of low-velocity impact on a multi-cell TCS structure at different kinetic energies.

3.2 Coupon Testing of Materials

3.2.1 Fabrication of composite laminate

The composite plate was fabricated from woven 0/90 E-glass fibre reinforced epoxy, and coupon tests were performed on it to find the mechanical properties of the parent material of the TCS structures. Six plies of woven E-glass fibre (R145) of 50 x 30 mm^2 were stacked together using Kinetix R246TX epoxy. The fibre is fabricated by Colan Australia, the fibre weight is 398 g/m^2 with a thickness of 0.5 mm, and the fibre modulus is 70.2 GPa. More information about the mechanical properties of this E-glass fibre can be found on the Colan Australia website. The fibre-epoxy ratio (weight fraction) is supposed to be 50% glass fibre and 50% Kinetix R246TX epoxy (Shin et al., 2015). The orientation fibre was kept same to eliminate the effect of fibre orientation on mechanical properties of the laminate composite materials. The wet

layup technique was used to fabricate the laminate, as shown in Figure 3.1. After 48 hrs of curing at room 25^{o} C, the sample was sent to the workshop for cutting according to the specified geometry of coupon tests.

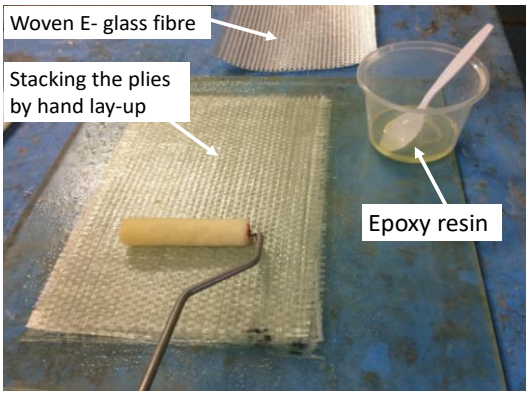

Figure 3.1: Fabrication of the composite laminate plate

3.2.2 Coupon test of composite laminate

As indicated above, to characterise the mechanical properties of the parent materials of the fabricated TCS structures, a series of the coupon tests was carried out on the fabricated composite laminate. These tests were performed according to the coupon test standards, as shown in Table 3.1. The MTS Insight electro-mechanical testing machine at 100 kN was used for the coupon tests, with a crosshead displacement rate of 2 mm/min. A tensile test was also performed on the epoxy resin to estimate the mechanical properties of the epoxy matrix.

Table 3.1: Coupon test types and the standards used in the tests

Test types	Standard	Qty
Tensile test	ASTM-D3039	5
Compression test	ASTM-D6641	5
Shear test	ASTM-D379	5
Tensile test of epoxy resin	ISO-527-1	5

3.2.3 Tensile coupon test

Five specimen coupon composites were tested under tensile test in accordance with standard ASTM-D3039 (2017). Figure 3.2 shows the profile details of the tested specimen, such as the effective length of the tensioned part, the length gripped by the

machine jaws (50mm), and the experimental setup. A uniaxial strain gauge of 5 mm was glued on two specimens to obtain local strain; however, the MTS machine system was exploited to measuring the strain of the other three coupon specimens. Table 3.2 summarizes the dimensions of the specimens.

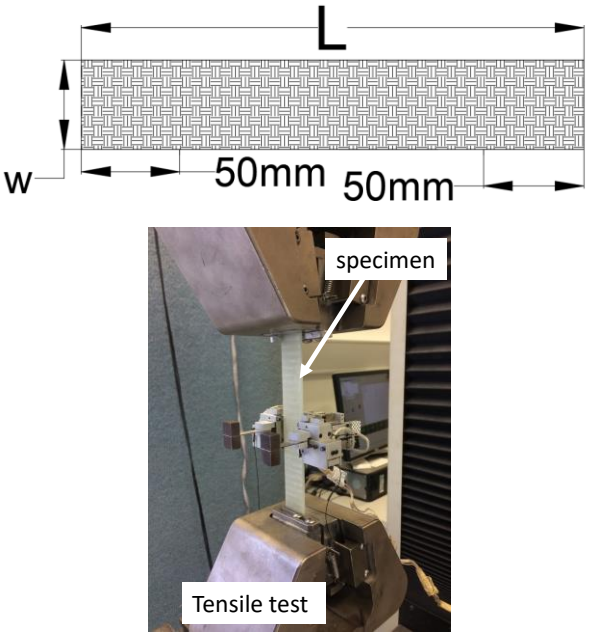

Figure 3.2: Tensile coupon test of woven E-glass fibre reinforced epoxy composite material according to standard ASTM D3039

Table 3.2: Dimensional details of the coupon composite specimens tested under tensile loading

Specimen ID	Length (mm)	Width (mm)	Thickness (mm)
S1-T	250	25	2.9
S2-T	250	25	3.0
S3-T	250	25	3.0
S4-T	250	25	2.95
S5-T	250	25	2.9

3.2.4 Compression coupon test

The standard ASTM-D6641 (2014) was used to perform the compressive coupon tests on the woven E-glass fibre reinforced epoxy composite. The specimens were loaded using an atypical combined loading compression (CLC) test fixture. Standard screws (M6 x 8) were used with bolt torque about 2.5 N.m to support the specimens' sides.

Figure 3.3 shows the geometrical dimensions of the specimens and the test procedure, and Table 3.3 summarizes the geometrical dimensions of the specimens in the compression coupon test.

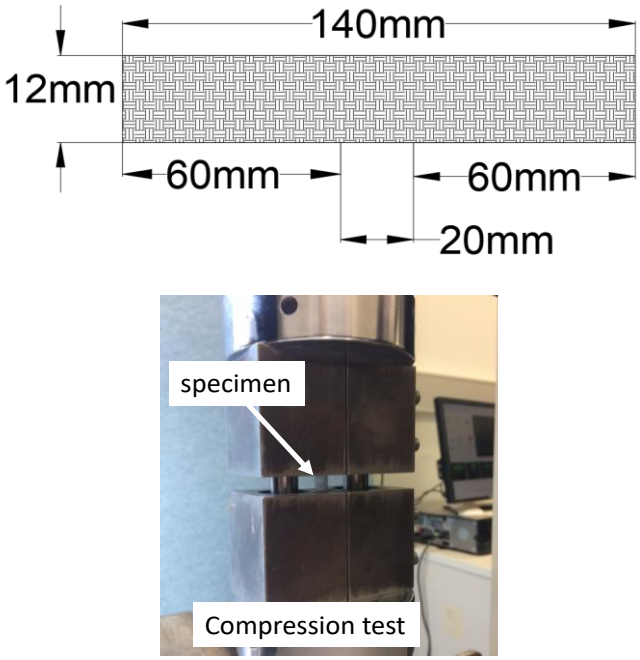

Figure 3.3: Schematic profile of the specimen and the compression coupon test of woven E-glass fibre epoxy reinforced epoxy composite material according to ASTM D6641 standard

Table 3.3: Dimensional details of the composite specimens tested with compressive loading

Specimen ID	Length (mm)	Width (mm)	Thickness (mm)
S1-C	140	12	3.0
S2-C	140	12	3.0
S3-C	140	12	2.9
S4-C	140	12	2.9
S5-C	140	12	2.95

3.2.5 Shear coupon test

Standard ASTM-D379 (2013) was used for the shear test. Figure 3.4 illustrates the recommended dimensions of the specimens. The coupons were cut at 45 degrees from the [0/90] cross-ply laminate to make notch roots with the vertical axis. These coupons

were cut in the warp direction of the woven fibre, i.e., in the diagonal direction of the panel. Table 3.4 reveals the average dimensions of the specific coupon specimens. Electrical resistance strain gauges (FLA-5-350-(QF)) were centered and attached to the notch roots at an angle of 45 degrees for two of the specimens. The strain gauge length was 4mm, and the width was 5.53mm, having a resistance of 350 ± 0.2 Ω. The load and strain data were stored and plotted.

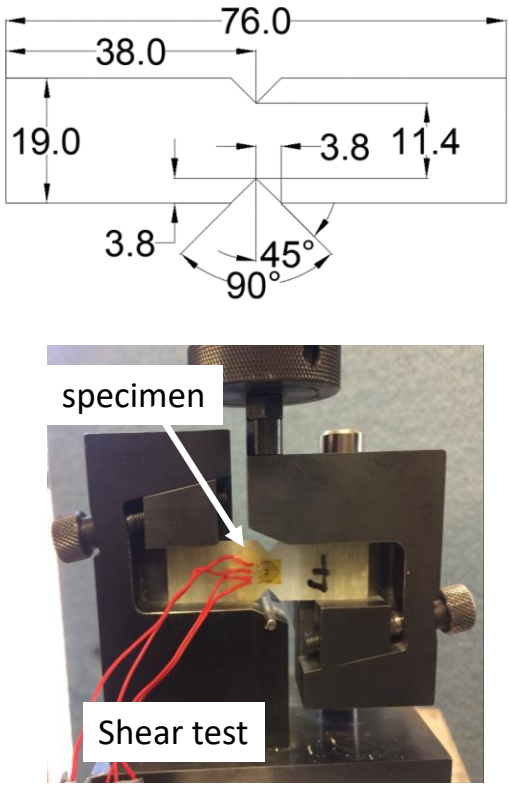

Figure 3.4: Shear coupon test of woven E-glass fibre reinforced epoxy composite material according to ASTM D579 standard

Table 3.4: Dimensional details of the composite specimens testsed with shear loading

Specimen ID	Length (mm)	Width (mm)	Thickness (mm)
S1-S	76	19	2.95
S2-S	76	19	2.95
S3-S	76	19	3.0
S4-S	76	19	2.9
S5-S	76	19	2.95

3.2.6 Coupon test of epoxy resin

The epoxy matrix utilized in this study comprises epoxy resin (R246TX) with a hardener (H160), purchased from ATL Composites Australia. The mix ratio (weight ratio) was 25:100 parts of hardener and resin, respectively. These were mixed and stirred for five mins to ensure the diffusion of the hardener in the resin. Then, the epoxy was poured into a dog-bone steel mould. The prepared samples were cured at 25^{o}C and de-moulded after 28 hours. International standard ISO-527-1 (2012) was used to perform the tensile test at a displacement rate of 1mm/min. Table 3.5 shows the geometrical parameters of the specimens of the epoxy resin matrix.

Table 3.5: Geometrical parameters of the specimens of the tested epoxy resin matrix

Specimens ID	Cross-section area (mm^2)	Effective length (*l*) (mm)
S-1	85.9	75
S-2	86.6	75
S-3	88.1	75

3.3 Fabrication of the TCS Structure

3.3.1 Preparation of moulds

Wooden moulds, consisting of an upper side termed the male part and a lower side termed the female part, was designed and fabricated for manufacturing the TCS structures. The moulds were applied to two groups of materials, the first group was fabricated as a single-cell corrugated core as shown in Figure 3.5 (a); the second was built as a multi-cell core (with three cells of the corrugated core) as shown in Figure 3.5 (b). For the first group, the moulds were coated by a non-sticky hot plastic sheet, while for the second, they were coated by a thermal plastic sheet. This was done to prevent the wet epoxy resin sticking to the moulds. Table 3.6 shows the geometrical dimensions of the fabricated moulds for the single-cell and multi-cell cores. The core angle was kept at a constant value of 45^{o} for the all corrugated core designs for all groups of TCS structures.

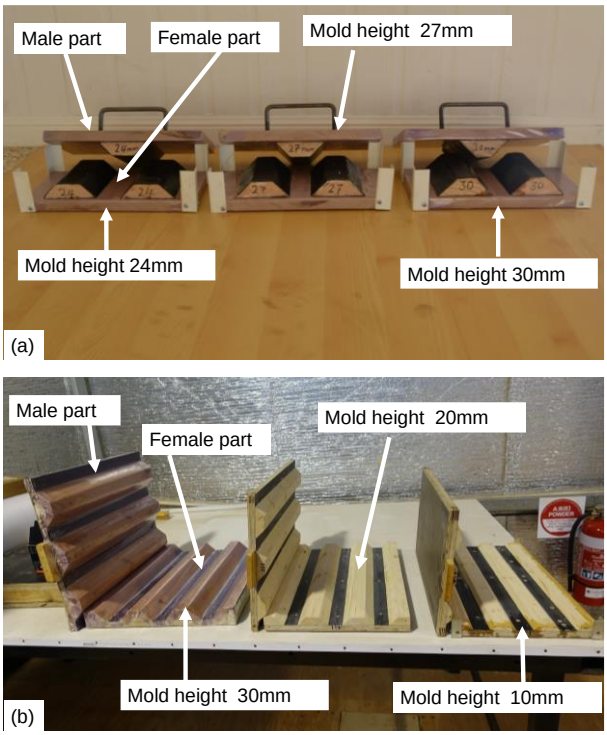

Figure 3.5: The moulds of three different core configuration, a) single-cell and b) multi-cell

Table 3.6: Design and dimensional details of the corrugated moulds

Mould	Number of cells	Height, (mm)	Angle	Short span (mm)	Long span (mm)
Mould-1	Single-cell	24	45	42	90
Mould-2	Single-cell	27	45	36	90
Mould-3	Single-cell	30	45	30	90
Mould-4	Multi-cell	10	45	30	50
Mould-5	Multi-cell	20	45	30	70
Mould-5	Multi-cell	30	45	30	90

3.3.2 Fabrication of the composite corrugated core

The wet layup technique was utilized to fabricate the corrugated core, as shown in Figure 3.6, due to its excellent ability to fabricate a complex shape (Elkington et al., 2015), and low cost. As previously mentioned in this chapter, several designs were used in the fabrication of single-cell and multi-cell cores to investigate the effect of the core geometry on the TCS structure's mechanical properties. In this case, woven E-glass fibre (0/90) was utilized in the fabrication of the composite corrugated core (GC).

The fibre was manufactured by Colan Australia to reinforce epoxy matrix Kinetix R246TX. The warp fibre was laid in the X direction, and weft fibre was laid in the Z direction, while the height of the TCS structure was aligned in the Y direction, as shown in Figure 3.7. However, according to the requested design, the plies' stacking numbers in the composite corrugated cores were four for GC1 and GC4, then six in GC2 and GC5, and eight in GC3 and GC6. After 48 hrs of curing at 25^{o}C, the entire corrugated cores were de-moulded. Then the fabricated corrugated cores were prepared to glue them with the upper face sheets.

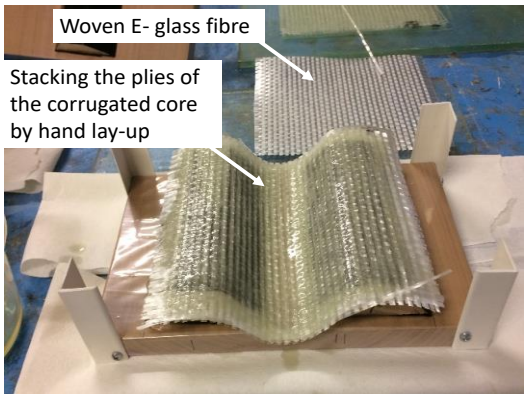

Figure 3.6: The wet-layup technique for manufacturing a single-cell TCS structure made from woven E-glass fibre reinforced composite polymer

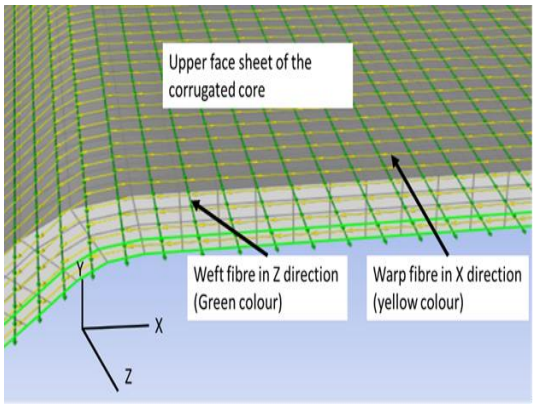

Figure 3.7: Fibre directions in the manufactured TCS structure

3.3.3 Fabrication of the composite “skin face sheet”

The upper and lower face sheets of the TCS structure were fabricated by a technique similar to the fabrication of the composite laminate for the coupon test using wet layup technique. In this work, all the skins were fabricated from woven E-glass reinforced epoxy composite utilizing the wet-layup technique. The ply numbers of the upper and lower face sheets are comparable to those of the corrugated core and these depended on the core configuration.

3.3.4 Gluing TCS structure parts

Techniglue R5 and H5 were used to bond the fabricated upper and lower face sheets with the composite corrugated core, as shown in Figure 3.8, to obtain the TCS structures, as seen in Figure 3.9. The R and H are the resin and the hardener, respectively. The proportion of R5 to H5 was 100/25g, respectively. R5-H5 Techniglue is convenient to combine composite materials together, and it has mechanical properties compatible to those of the Kinetix R246TX epoxy matrix. Then, based on the research requirements, the specimens were cut and finished to the required geometrical measurements. The dimension accuracy of the TCS structure was acceptable. The thickness deviation of the fabricated parts of all the TCS structure was approximately less than 2% mm. This is mainly due to using constant pressure on the moulds. Figure 3.10 shows the schematic diagram of the single-cell TCS structure.

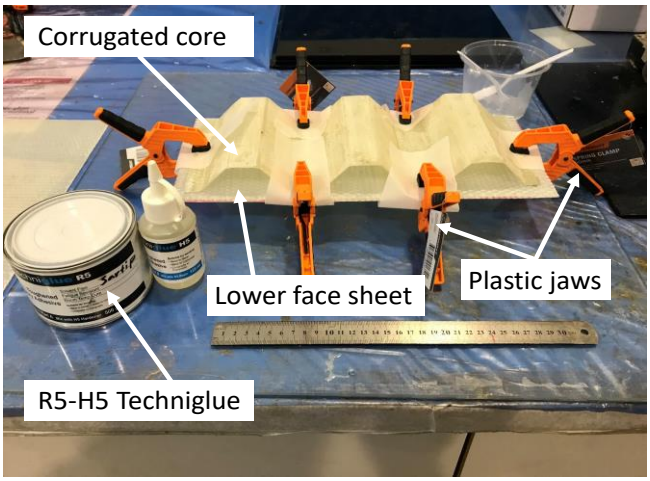

Figure 3.8: Bounding of fabricated upper and lower face sheet and corrugated core by using R5 and H5 Techniglue

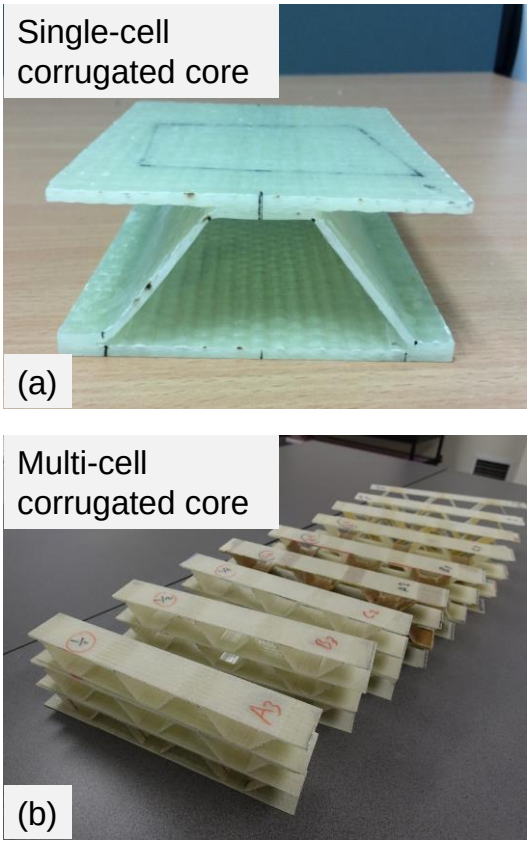

Figure 3.9: Manufactured specimens of the TCS structures

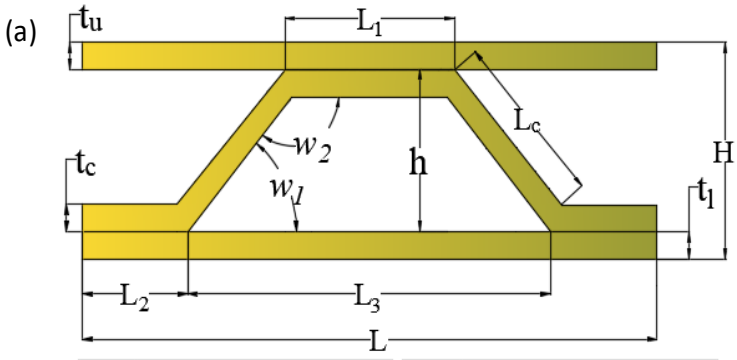

L	Unit cell length	h	Core height
L_1	Short span length	t_u	Upper face sheet thickness
L_2	Lower core member length	t_c	Core thickness
L_3	Long span length	t_l	Lower face sheet thickness
L_c	Core struts length	w_1	Lower core angle
H	Sandwich height	w_2	Upper core angle

Figure 3.10: Schematic diagrams of single-cell TCS structure

3.4 Quasi-Static Test of the TCS Structure

A series of experimental tests of out-of-plane quasi-static compression were conducted on three groups of the single-cell TCS structures (GC). Each group of TCS structures had its own geometrical parameters. The MTS Insight electro-mechanical testing machine at 100 kN capacity was employed to perform the tests, as shown in Figure 3.11. The TCS structures were subjected to displacement time loading at the rate of 0.5mm/min for all the tests. Moreover, in the quasi-static compression tests, two different loading conditions were employed to further investigate the TCS structures' mechanical behaviour. The compression effect of upper faces sheet has been neglected due to no constraint of its edges, where face sheet has free movement.

3.4.1 TCS structures supported in cross direction

In the first condition, groups GC1, GC2, and GC3 were supported in the cross direction (CD) using two steel rollers, as shown in Figure 3.12. The length of the support span was 86 mm in the first test; then the span length was increased to 90 mm to move the support under the inner lower angle of the core struts and tested. Next, the support span was increased to 94 mm for the third test, and for the last case, the length of the support span was 98 mm. The load was applied on the top plate by the flat surface of the ram head. More details about the tested TCS structures with this loading condition are shown in Table 3.7.

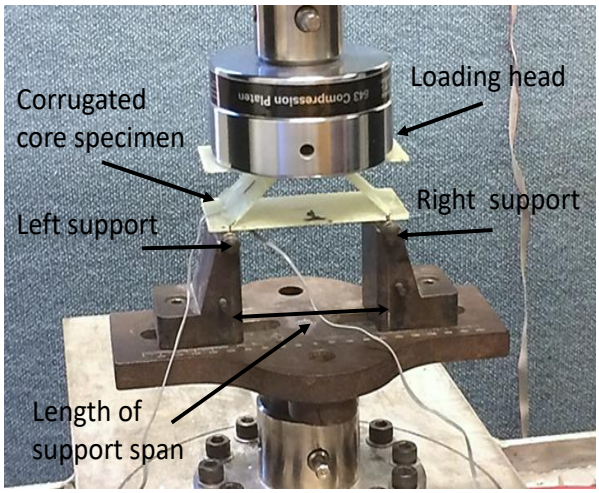

Figure 3.11: Quasi-static compression test of the single-cell TCS structure supported in CD

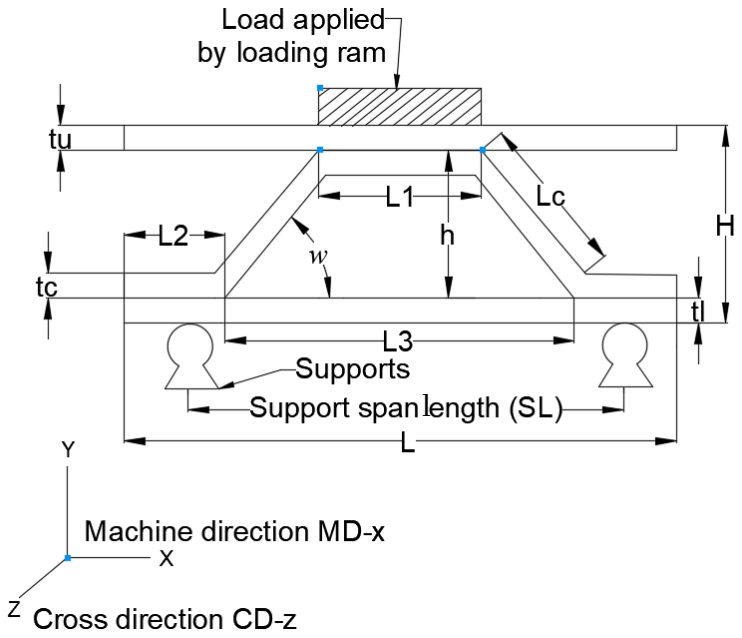

Figure 3.12: Schematic profile of the single-cell TCS structure supported in CD

Table 3.7: Geometrical parameters of the TCS structure tested under quasi-static compression loading supported in CD

Specimen ID	Qty	Lc	L1	h	tc	tu & tl	Core aspect ratio	Ply No
		(mm)	(mm)	(mm)	(mm)	(mm)	tc/Lc	
GC1	4	42	28	30	1.91	2.95	0.045	4-plies
GC2	4	42	28	30	2.85	3.0	0.067	6-plies
GC3	4	42	28	30	3.80	2.95	0.091	8-plies

* Specimen dimensions are the average values of the four specimens in each group

3.4.2 TCS structures supported in machine direction

In the second quasi-static compression loading condition, the TCS structure was supported in machine direction (MD) by being laid on a rigid support plate, as shown in Figure 3.13. In this type of loading condition the groups GC4, GC5, and GC6 were selected. Table 3.8 illustrates more details about the designs of the TCS structure.

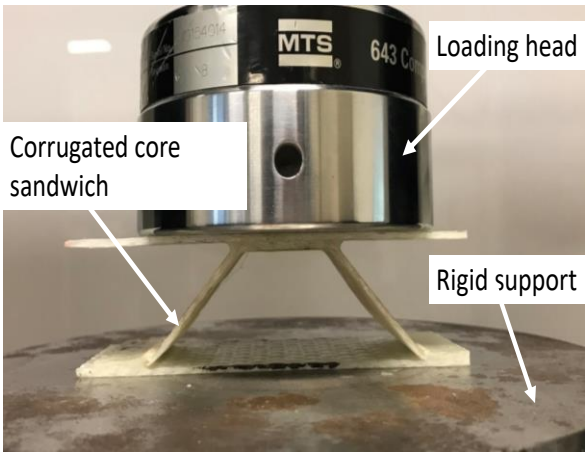

Figure 3.13: Quasi-static compression test of the single-cell TCS structure supported with rigid steel plate i.e. supported in MD

Table 3.8: Dimensional details of the TCS structure tested with quasi-static compression loading in MD

Specimen ID	Qty	L_c	L1	h	t_c	t_u & t_l	Core aspect ratio	Py No
		(mm)	(mm)	(mm)	(mm)	(mm)	t_c/L_c	
GC4	3	42	28	30	1.92	3	0.045	4-plies
GC5	3	42	28	30	2.82	3	0.067	6-plies
GC6	3	42	28	30	3.83	3	0.091	8-plies

* Specimen dimensions are the average values of the four specimens in each group

3.5 Low-Velocity Impact Tests on TCS Structure

Low-velocity impact tests were conducted on TCS structures by employing a drop-weight impact tower. Figure 3.14 shows the schematic diagram of the impact tower, which was built by the author at the University of Southern Queensland. This drop-weight impact system involves an impactor weight and impactor head that falls along guideposts and collides with the target. Two steel rods of a 25mm diameter were utilized to control the impactor head movement. The surface of the steel rods was covered with grease, and the impactor weight was connected to a rigid plastic tube. This was done in order to reduce the friction coefficient between the steel rods and the plastic tube. Therefore, the contact friction force between the steel rods and plastic tube of the impactor was neglected. At the end of the impact event, the impactor head

stopped by means of a plastic stopper attached to the rod. This was to prevent any unexpected impact between the impactor head and the base of the impact tower.

In this study, low-velocity impact tests were performed on different cell designs of the TCS structure with several impact event conditions. The kinetic energy of the low-velocity impact tests was designated to be at and beyond the visible damage threshold energy of the composite parent materials, and this is discussed in the next sections in this chapter. The TCS structure was placed on a rigid plate to represent the supports in MD, and clamped along two sides only, by jaw clamp, according to the method of Jang et al. (1991). Two wood parts were attached between the upper and lower face sheets of the structure to adjust the movement of the upper skin sheet (Figure 3.14). The Siemens LMS- SCADAS system was used for data acquisition. A piezoelectric load sensor model PCB-200C20 was set in between the impactor load and striker tip. This was to achieve a realistic collision event. The accelerometer PCB-5014B was positioned with the impactor mass to measure the acceleration of the impactor. The output acceleration was integrated to obtain the displacement of the impactor head. A high-speed camera (Sony RX100) was employed to capture the impact event and the deformation of all TCS structure members. At the end of the tests, the acquired data were stored for post-processing.

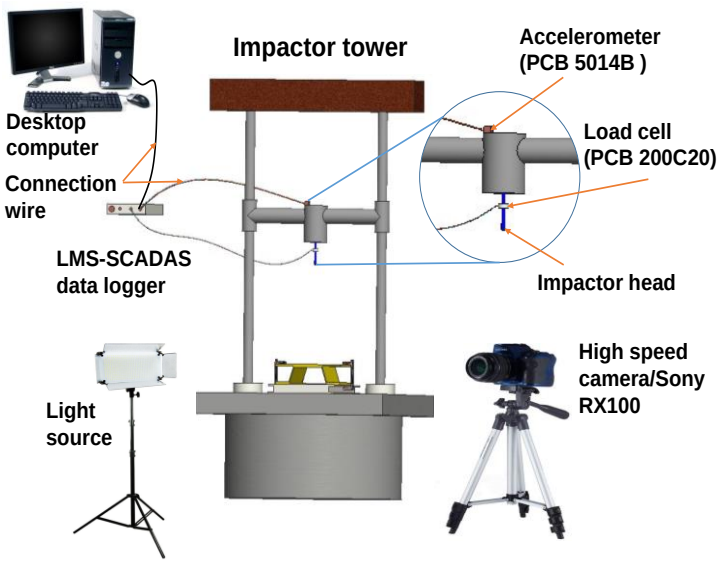

Figure 3.14: The drop-weight tower setup to perform low-velocity impact test on the TCS structure

3.5.1 Impact tests at visible damage threshold energy

Low-velocity impact tests were carried out on the TCS structure of GC7, as shown in Figure 3.15, at the visible damage threshold energy of the parent materials. This was to investigate the impact behaviour and damage mode of the TCS structure at that level of kinetic energy. The visible damage threshold energy of the total thickness of the upper face sheet and flat corrugated core member was designated based on Equation 3.1 of the ASTM-D7136 (2012) Standard.

$$E_P = t.C_E \quad 3.1$$

Where E_P is the threshold value of damaged energy (J), and t is the specimen thickness (i.e. thickness of upper face sheet plus the thickness of the core), and C_E is the specific ratio of impact energy to specimen thickness (6.7 J/mm).

A steel mass of 2.3 kg was dropped from a height of 1.02 m to impact on the centre of the short span of the TCS structure. The impactor velocity at the impact moment was 4.47m/s as calculated by Equation 3.2. Then the kinetic energy (K.E) of the impact can be estimated by Equation 3.3. The K.E of GC7 is 23J and about 10% more than the visible damage threshold.

$$v = (2g.h^i)^{0.5} \quad 3.2$$

And

$$E_K = \frac{1}{2}m.v^2 \quad 3.3$$

Where g is the gravity and h^i is the height of the impactor head before starting the movement, and m and v are the impactor mass and velocity prior the impact event, respectively. Table 3.9 shows the geometrical parameters of the TCS structure GC7.

In this work, three different shapes of steel impactor heads, a 12 mm flat head (FH), a 12 mm hemispherical head (HH) and a 12 mm conical head (CH), were used. This was to overcome the effect of the impactor shape on the TCS structure's impact behaviour and damage modes. The shape and schematic profile of each impactor head are shown in Figure 3.16. A high-speed camera (Sony-RX100Y) was used to observe the entire deformation of the specimens and other information on the testing of the TCS structure under the low-velocity impact. Table 3.10 shows the details of the low-velocity impact procedure of the TCS structure of GC7.

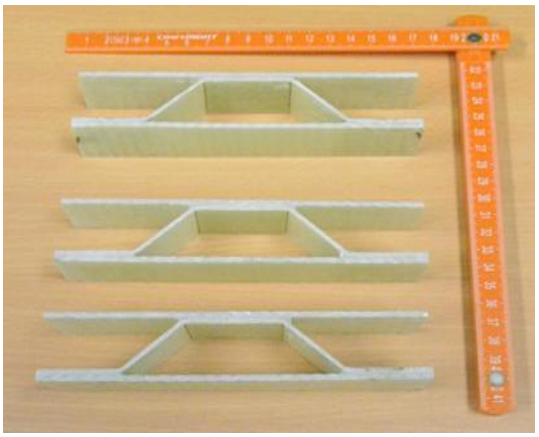

Figure 3.15: Single-cell of GC7's TCS structure tested under low-velocity impact

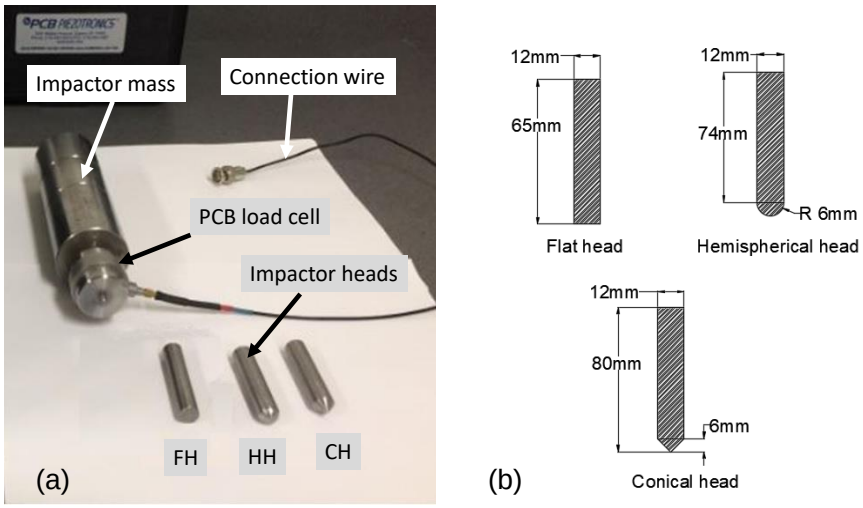

Figure 3.16: Three different impactor heads, fat (FH), hemispherical (HH), and conical (CH)

Table 3.9: Geometrical parameters of GC7 TCS structure subjected to impact test at visible damage threshold energy

Specimen ID	Qty	t_c (mm)	h (mm)	t_u & t_l (mm)	L_1 (mm)	H (mm)	W (gm)
GC7	3	1.33	25.3	1.82	38.02	28.94	50

Table 3.10: Low-velocity impact test procedure of the GC7 TCS structure

Test ID	Impactor head	Impactor weight (kg)	Impactor velocity (m/s)	Kinetic energy (J)
i	FH	2.3	4.47	23
ii	HH	2.3	4.47	23
iii	CH	2.3	4.47	23

3.5.2 Impact tests beyond visible damage threshold energy

Low-velocity impact tests beyond the visible damage threshold energy of composite materials were carried out on three differently designed TCS structures to characterise their impact behaviour. The configurations GC8, GC9, and GC10 include a single-cell TCS structure, as shown in Figure 3.17. Table 3.11 shows the geometrical parameters of the test samples of TCS structures for GC8, GC9, and GC10.

Low-velocity impact tests were performed on the TCS structures using the procedure defined in the ASTM-D7136 (2012) Standard. The TCS structure was also impacted on the centre of the short span of the core and the impact kinetic energy was set beyond the threshold energy by 25-35%. This was to ensure that the specimens would break. As with the earlier impact test, the investigation was performed using three different steel impactor heads: a 12 mm FH, a 12 mm HH, and a 12 mm CH. This was to evaluate the effect of impactor shape, as shown in Figure 3.16. Table 3.12 shows more details about the impact procedure of GC8, GC9, and GC10 TCS configurations.

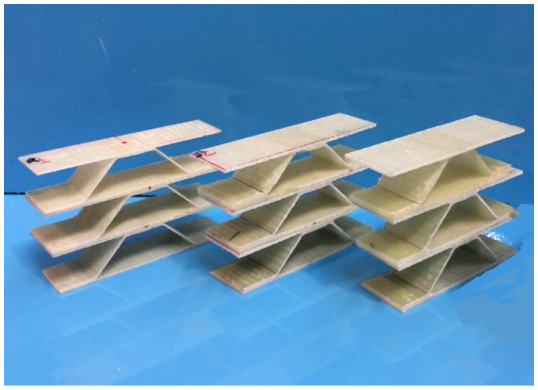

Figure 3.17: Three different configurations of the single-cell GC8, GC9, and GC10 TCS structures

Table 3.11: Different configurations of the TCS structure subjected to impact event beyond the visible damage threshold energy

Specimen ID	QTY	t_c (mm)	h (mm)	t_u & t_l (mm)	L_1 (mm)	H (mm)	W (gm)
GC8	3	1.45	27.5	1.82	32.2	33.4	49.4
GC9	3	2.09	27.5	2.43	33.3	35.7	71.4
GC10	3	2.07	30.1	2.58	27.1	38.7	70.5

** FH, HH, and CH are flat, hemispherical and conical impactor head, m and E are the impactor mass and kinetic energy, respectively

Table 3.12: Low-velocity impact test procedure of the GC8, GC9, and GC10 sandwiches

Test ID	Impactor head	Impactor weight (kg)	Impactor velocity (m/s)	Kinetic energy (J)
i	FH	4	4.47	40
ii	HH	4	4.47	40
iii	CH	4	4.47	40

3.5.3 Impact tests with different impactor weights

The GC11 TCS structure, as shown in Figure 3.18, was also subjected to a low-velocity impact test and the configurations of this are explained in Table 3.13. The hemispherical impactor head of 12 mm diameter was employed in the tests. Velocity and energy equations were used to estimate the impactor velocity and kinetic energy prior to the impact Table 3.14 shows the impact test procedure of the GC11 sandwich. The previous instruments were utilized in measuring the impact output. It should be noted that the hemispherical impactor head was selected in this test procedure. This was due to the active middle role of the hemispherical impactor head in comparison to other impactor types. As well, as the connection screw of the flat impacted head was damaged in an unexpected accident outside the tests.

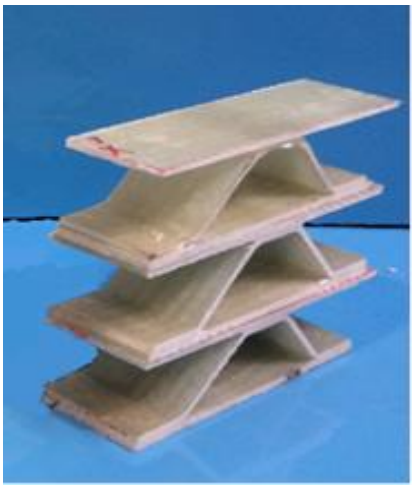

Figure 3.18: The single-cell GC11 TCS structure

Table 3.13: Different configurations of the TCS structure subjected to impact test by different impact weights

Specimen ID	Qty	t_c (mm)	h (mm)	t_u & t_l (mm)	L_1 (mm)	H (mm)	W (gm)
GC11	3	2.66	32.7	3.43	30.6	40	82.7

Table 3.14: Low-velocity impact test procedure with the GC12 TCS structure

Test ID	Impactor head	Impactor weight (kg)	Impactor velocity (m/s)	Kinetic energy (J)
i	HH	15.7	2.62	54
ii	HH	8.6	3.54	54
iii	HH	5.4	4.47	54

3.5.4 Impact test on multi-cell TCS structure

Low-velocity impact tests were carried out on the multi-cell GC12 TCS structure, with geometrical parameters given, in Figure 3.19 and Table 3.15. The impact tests were performed by utilizing a 12 mm hemispherical impactor head with three different impactor weights: 2.5 kg, 3.25 kg and 4 kg. Here, the critical impact energy of 40 J was chosen for impact testing of the GC12 TCS structure (Davies and Olsson, 2004),

as well as to compare the performance of the multi-cell with single-cell TCS structures. The impact test procedure on the GC12 TCS structure is given in Table 3.16 below.

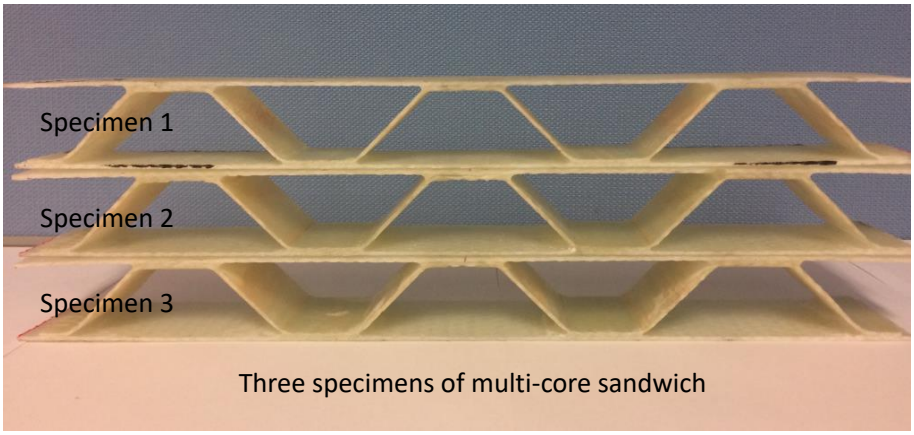

Figure 3.19: Multi-cell TCS structure GC12

Table 3.15: Geometrical parameters of the GC12 multi-cell TCS structure

Specimen ID	QTY	t_c (mm)	h (mm)	t_u & t_l (mm)	L_1 (mm)	H (mm)	W (gm)
GC12	3	2.09	30.1	2.6	27	38.6	166.9

Table 3.16: Low-velocity impact test procedure of the GC12 multi-cell TCS structure

Test ID	Impactor head	Impactor weight (kg)	Impactor velocity (m/s)	Kinetic energy (J)
i	HH	2.5	4.47	25
ii	HH	3.25	4.47	32.5
iii	HH	4.0	4.47	40

3.6 Summary

The fabrication technique for composite specimens, specifically the laminate composite plate and TCS structure, were presented in this chapter. The design and manufacturing of several moulds to be used in the fabrication of the TCS structures were described. The chapter also detailed the experimental procedure of quasi-static compression tests on TCS structures supported in both the cross direction and machine direction. Then, the experimental procedure was explained for low-velocity impact tests of different designs of TCS structure at and beyond the visible damage threshold energy of the composite materials. The low-velocity impact tests with different impactor weights on single-cell TCS structures were characterised. Finally, the low-velocity impact on a multi-cell composite TCS structure at different kinetic energies was detailed.

Chapter 4

Experimental Results and Discussion

4.1 Introduction

The experimental outcomes of the current research are presented in this chapter. First, the outcome of the laminated composite plate coupon test is presented. The trapezoidal core structures were anisotropic structures when they fabricated with metal materials. However, although composite materials are brittle, the TCS structures were predicted to be probably anisotropic, which is why they were subjected to quasi-static compression loading conditions to explore their mechanical behaviour. The results of the quasi-static compression test on the single-cell TCS structure will be discussed. In addition, due to the expected anisotropic mechanical behaviour, the damage mechanism of such TCS structure will differ under loading conditions, which is also explored. Furthermore, the TCS structure is compared with other core materials and types, to indicate their mechanical properties relative to other used cores in the literature.

The latter parts of the chapter discuss the low-velocity impact behaviours, observed failure mechanisms, and energy absorption capability of the TCS structure, including several sandwich designs and various impact conditions. Due to the composite corrugated core being located between the upper and lower face sheets, the visible damage threshold impact energy of the TCS might be more than for the composite parent material, therefore low-velocity impact tests at and beyond the visible damage threshold energy were performed and are discussed.

4.2 Characterisation of the Parent Material

The mechanical properties of the woven E-glass fibre reinforced epoxy composites used in the fabrication of the trapezoidal corrugated core structure were investigated through a series of coupon tests. The mechanical properties of such parent materials

were also employed in a finite element simulation of the TCS structure with different loading conditions, which is discussed in Chapter 5. The following section details the results of the coupon tests.

4.2.1 Tensile tests

Five specimens were prepared by stacking six plies (0/90) of woven E-glass fibre reinforced epoxy to perform tensile tests according to the ASTM-D3039 (2017) standard. Typical stress-strain curves for the composite woven E-glass fibre reinforced epoxy are shown in Figure 4.1. The specimens exhibited linear elastic behaviour until failure. The maximum tensile stress ranged from 210 to 240 MPa, and the strain at this failure stress extended from 0.0185 to 0.021. This shows an acceptable variation of less than 15% for both stress and strain; thus, it can be concluded that the fibre orientation and laminate fabrication were both controlled appropriately. The tested specimens also exhibited similar failure modes of brittle fracture of the composite, as illustrated in Figure 4.2. Subsequently, the Poisson's ratio was estimated from the obtained strain at the longitudinal and transverse directions of the specimens by utilizing Equation 4.1:

$$\nu_{xy} = \frac{d\epsilon_y}{d\epsilon_x} \qquad 4.1$$

Where ν_{xy} is the Poisson's ratio, $d\epsilon_x$ and $d\epsilon_y$ are strain in the X- and Y-direction, respectively. Fromm the experimental data, the tested laminated composite specimens' average Poisson ratio (ν_{xy}) was about 0.15. Table 4.1 shows the mechanical properties of the tested samples.

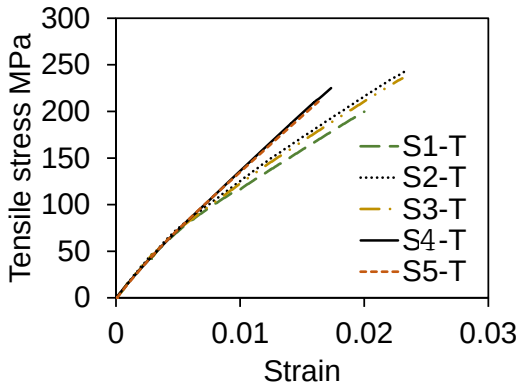

Figure 4.1: The stress-strain response of the tensile test of composite laminate woven E-glass fibre reinforced epoxy

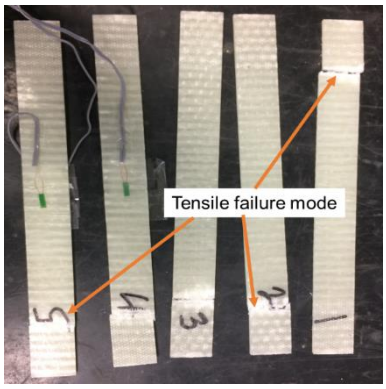

Figure 4.2: Tensile failure of the coupon specimens

4.2.2 Compression tests

Compression testing was carried out on five coupon specimens utilizing the ASTM-D6641 (2014) standard and a combined loading compression (CLC) test fixture. Figure 4.3 shows the compression stress as a function of the strain of the specimens. The compressive stress-strain curves of all specimens show comparable trends of linear elastic response until the fracture. The compressive stress range was about 184 MPa to 195 MPa at the strain value of 0.086 to 0.09, respectively. The results reveal a variation in the compressive tests of less than 6%, which indicates the accuracy of the stacking fibres and the experimental tests. The specimens exhibited brooming failure mode under compression load, as shown in Figure 4.4. The mechanical properties and ultimate compressive strength of the tested samples are summarized in Table 4.1.

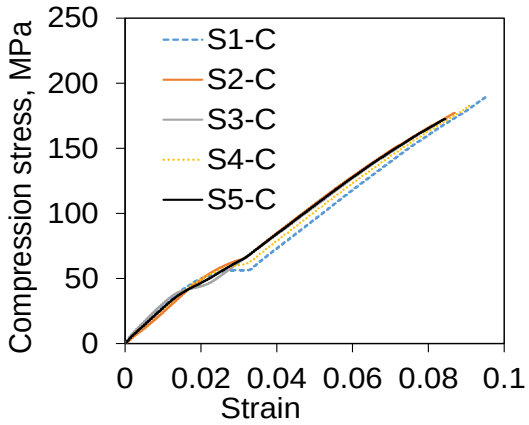

Figure 4.3: Stress-strain response of the compression test of composite laminate E-glass fibre reinforced epoxy

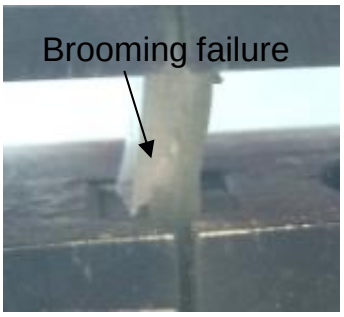

Figure 4.4: Brooming failure mode of the woven E-glass fibre composite during the compression test

4.2.3 Shear test

Five specimens of woven E-glass fibre composite coupons were examined according to standard ASTM-D379 (2013) to obtain their shear properties. The load and strain data were stored and plotted as shown in Figure 4.5. The maximum shear strength was about 40 MPa. However, the specimens S-4 and S-5 tested with strain gauges (type-AF-5) and they exhibited less stress-strain response, due to early stopping these two tests because of strain gauge damage. The strain value ranged between 0.03 for the samples with strain gauges and 0.05 for the rest of the specimens. All specimens demonstrated a similar trend for shear response values; this was due to the composite laminate and ply stacking being well made. In addition, the damage of all tested specimens was in the notch roots associated with fibre breakage, as shown in Figure 4.6. Based on theory of the composite material (Jones, 1998) all the unknown mechanical properties of the woven E-glass composite materials were calculated. Table 4.1 summarizes the mechanical properties of the coupon tests of the woven E-glass fibre reinforced epoxy composite laminate.

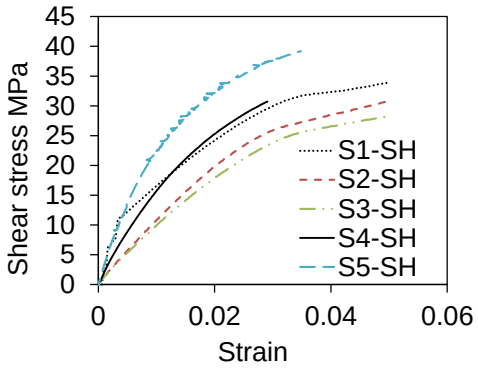

Figure 4.5: Stress-strain response of the shear test of woven E-glass fibre reinforced epoxy composite laminate

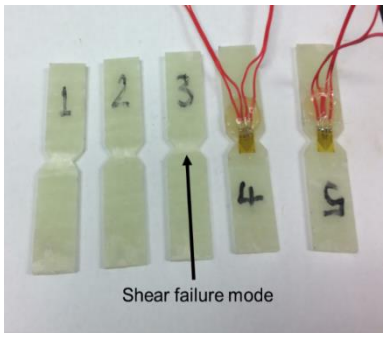

Figure 4.6: Shear failure mode of woven E-glass fibre reinforced epoxy composite laminate after the shear test

Table 4.1: Mechanical properties of woven E-glass fibre reinforced epoxy composite laminate - average values

Symbol	Property	Value	Unit
$E_{11,}$	Young's modulus in the longitudinal direction	13.5	GPa
E_{22}	Young's modulus in the transverse direction	13.5	GPa
E_{33}	Young's modulus in the thickness direction	1.5	GPa
$\nu_{12,}$	In-plane Poisson's ratio	0.15	
ν_{23},ν_{13}	Through thickness Poisson's ratio	0.34	
G_{12}	In-plane shear modulus	1.11	GPa
$G_{23,}\ G_{13}$	Through thickness shear modulus	1.01	GPa
X^T	Longitudinal tensile strength	225	MPa
X^C	Longitudinal compressive strength	-190	MPa
Y^T	Transverse tensile strength	225	MPa
Y^C	Transverse compressive strength	-190	MPa
S^L	Longitudinal shear strength	40	MPa
S^T	Transverse shear strength	40	MPa

4.2.4 Coupon test of the epoxy resin

Epoxy resin is widely utilized with reinforced fibres to fabricate composite laminate; this is due to its desirable properties, such as high stability, adhesiveness, and lightness in weight. The epoxy matrix used in this study comprises epoxy resin (R246TX) with a hardener (H160), purchased from KINETIX-ATL Composites Australia. The prepared specimens were tested according to ISO-527-1 (2012). Figure 4.7 shows the stress-strain curve of these tested specimens; the epoxy resin exhibited a linear response under the tensile test. The ultimate strength, stiffness, and strain of the epoxy resin matrix have been measured from the test outputs. Under similar testing conditions, all the specimens exhibited approximately comparable mechanical properties. Table 4.2 shows the mechanical properties of the specimens of the epoxy resin matrix.

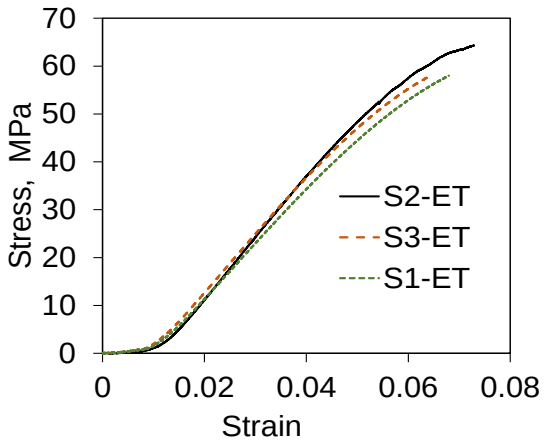

Figure 4.7: The stress-strain response of the tensile test of neat epoxy resin specimens

Table 4.2: Mechanical properties of the epoxy resin matrix

Specimens	Ultimate strength, MPa	Ultimate strain, %	Young's modulus, GPa
S1	58.15	4.75	1.22
S2	64.22	4.95	1.29
S3	58.12	4.81	1.21

4.3 Mechanical Behaviour of the TCS Structure under Quasi-Static Loading

This section is focused on the mechanical behaviours of the TCS structures under a quasi-static compression load. The mechanical behaviours, damage mechanisms, and energy absorption capacities of these structures were experimentally investigated when the sandwiches were supported in the cross direction (CD) and machine direction (MD).

4.3.1 Mechanical behaviour of the TCS structure supported in CD

Three groups of TCS structures (GG1, GG2, and GG3) were tested experimentally under quasi-static compression load. Each group consisted of four specimens with a single-cell core and the effect of the support span length (SL) was investigated. The geometrical parameters and relative densities of each group are different, as summarized in Table 3.7. This was done also to examine the influence of the geometrical parameters and relative densities of the composite core on the mechanical behaviour of the TCS structure.

Figure 4.8 shows four curves of force-displacements for the first group of TCS structures. The results of all tests exhibited three prominent stages: linear elastic (1) non-linear elastic (2) and softening response at post bucking (3). The load-displacement in Stage 1 was attributed to the core struts sharing the applied load with a small core deformation. In Stage 2, due to local elastic buckling of the core struts, the TCS structure showed large displacement; thus, the TCS structure revealed a non-linear force-displacement response. Moreover, exceeding core elastic buckling strength in Stage 3 led to shear delamination (Xu et al., 2016) and tensile failure of the core struts' outer plies. As a result, the composite core struts exhibited stiffness degradation, which led to a decrease the non-linear force displacement of the TCS structure.

From Figure 4.8, the SL: 86 mm showed minimal peak load, due to considerable elastic negative bending of the lower face sheet (Figure 4.9). The core struts buckled out of the trapezoidal core members, followed by core strut fracture in the core's cross width, as shown in Figure 4.9. Figure 4.8 shows that an increase of the support span length to SL: 90 mm (i.e., under the core struts) led to raising the peak load, due to core restraint core axial deformation at support position; thus, increasing the reaction force at the core struts. The core struts also showed fracture at the inclined member's midpoint after the elastic buckling, as seen in Figure 4.10. However, on increasing the

support span length to SL: 94 mm, the peak load decreased (Figure 4.8) due to a reduction in the core struts' resistance and an increase in the core's axial deformation. In this case, the composite core struts also failed closer to the mid length of struts, as seen in Figure 4.11. In the final test of GG1, with the support span length raised to SL: 98 mm, this led to a decreased peak load, less than the case for SL: 94 mm, as shown in Figure 4.8. This was mainly due to the high flexibility of the core struts' base, compared to previous tests. From the captured photos (Figures 4.9, 4.10, and 4.11), it can also be seen that the core struts fractured due to outside core struts buckling with the cases SL: 86 mm, SL: 90 mm, and SL: 94 mm. However, at SL: 98 mm, the composite core struts fractured close to the lower core angle due to buckling of the core struts inside the trapezoidal core shape (see Figure 4.12). It can be concluded that the TCS structure has different mechanical behaviour and core deformation when supported by different CD conditions.

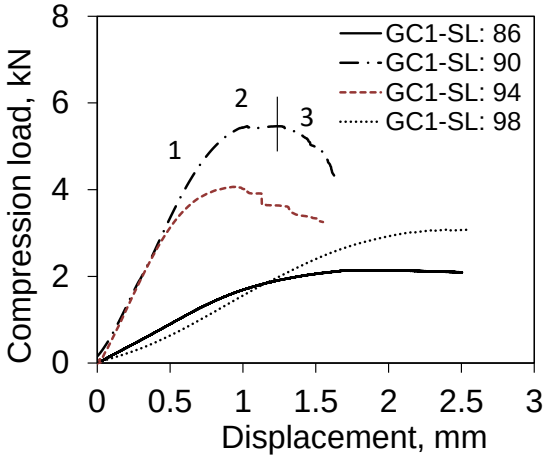

Figure 4.8: Load displacement compression response of GC1 TCS structure supported in CD

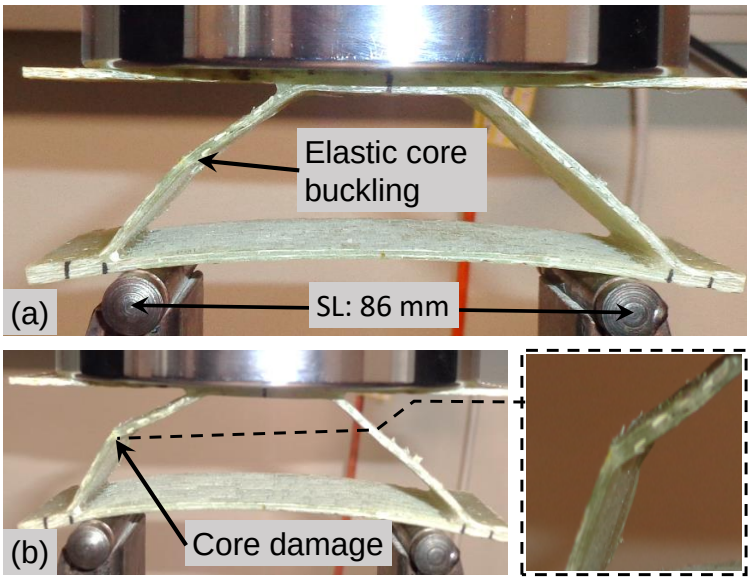

Figure 4.9: Montage of deformation of the TCS structure GC1 under the compressive quasi-static load of SL: 86 mm; a) Buckling of core struts and bending of lower face sheet, and b) Post buckling and core strut damage

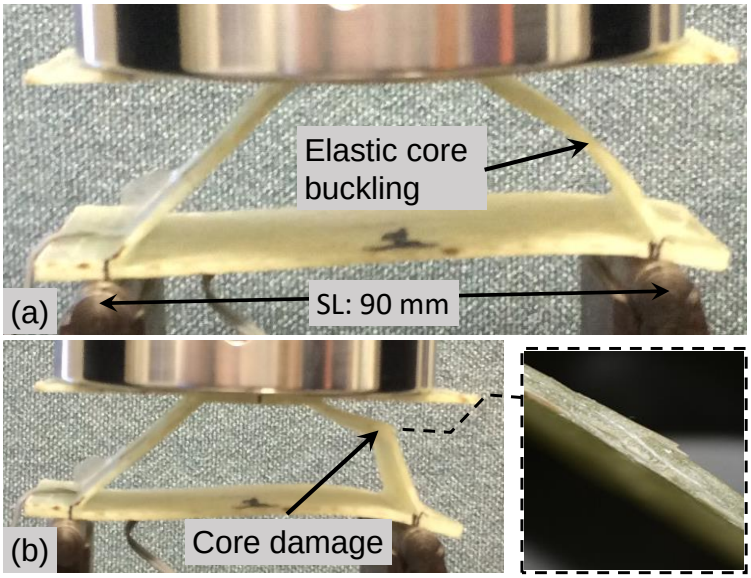

Figure 4.10: Montage of deformation of GC1 TCS structure under the compressive quasi-static load of SL: 90 mm; a) Buckling of core struts and bending of lower face sheet, and b) Post buckling and core strut damage

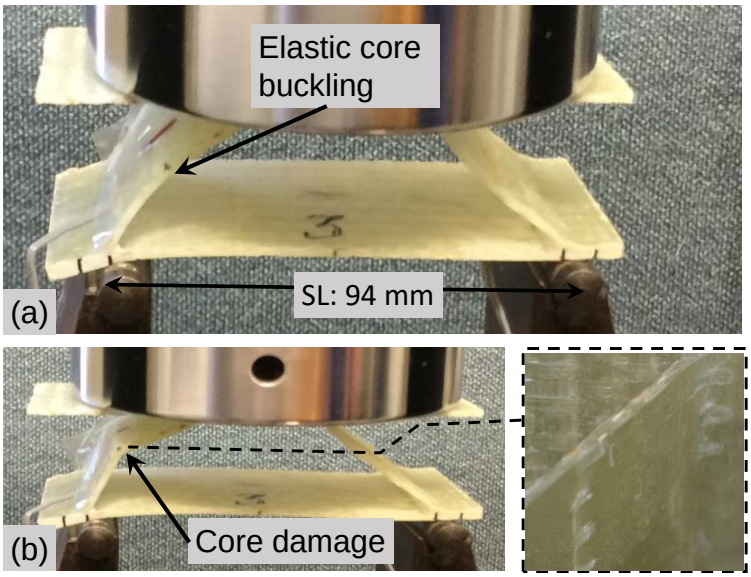

Figure 4.11: Montage of deformation of GC1 TCS structure under the compressive quasi-static load of SL: 94 mm; a) Buckling of core struts and bending of lower face sheet, and b) Post buckling and core strut damage

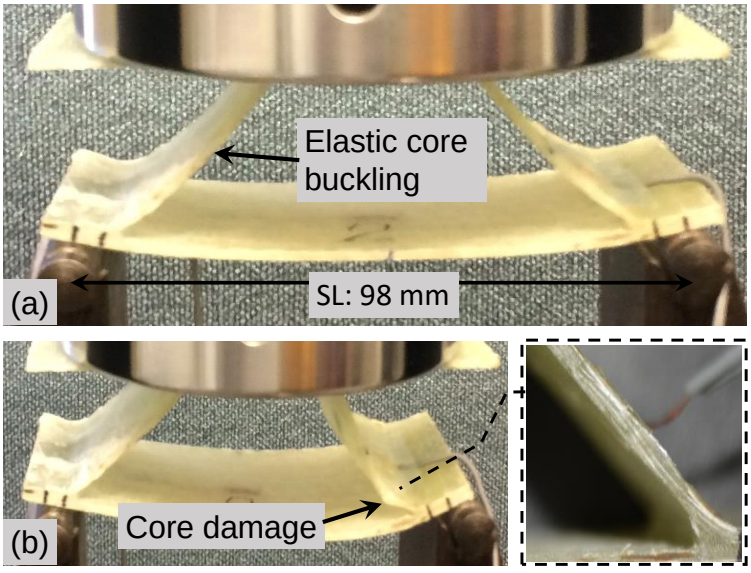

Figure 4.12: Montage of deformation of GC1 TCS structure under the compressive quasi-static load of SL: 98 mm; a) Buckling of core struts and bending of lower face sheet, and b) Post buckling and core strut damage

A comparison of the load-displacement of GC1, GC2, and GC3 TCS structure at SL: 90 mm, as shown in Figure 4.8, Figure 4.13, and Figure 4.14, the core thickness increasing from 1.9 mm (GC1) to 2.8 mm (GC2) and then to 3.8 (GC3), revealed an increase of the sandwich strength from 5.7 kN to 11.8 kN and then 15.5 kN, respectively. This was attributed to a decrease of elastic buckling of the slender core, and meanwhile an increase of compression resistance of the thicker composite core struts with less bulking deformation.

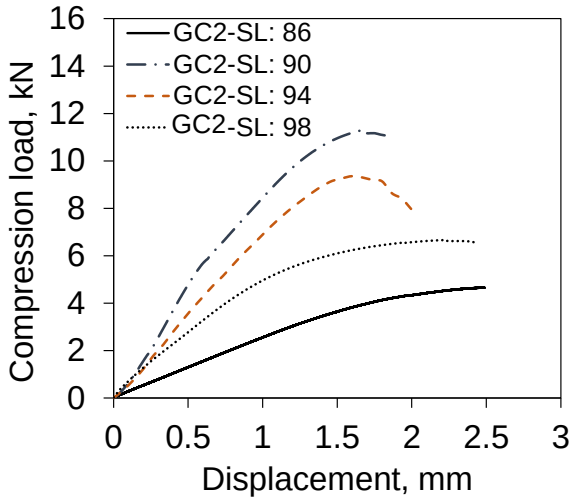

Figure 4.13: Load-displacement compression response of GC2 TCS structure supported in CD

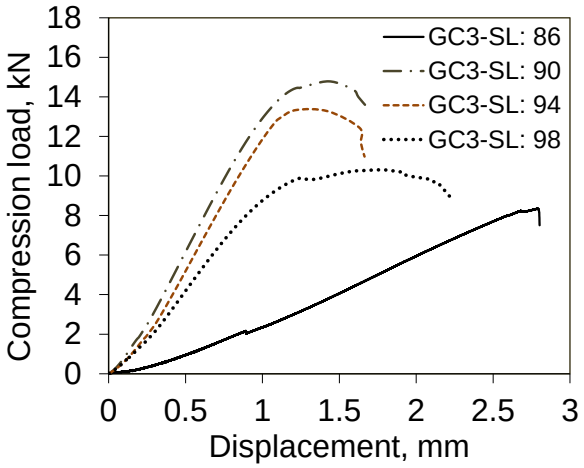

Figure 4.14: Load-displacement compression response of GC3 TCS structure supported in CD

The outcome of the investigation shows that the same design of the TCS structure has variable compression strength if supported in CD. The second major finding was that the single-cell TCS structure shows maximum compression strength/stiffness when the support was laid under the core struts in CD. This means a proper understanding of the forced boundary conditions (i.e. support position) is critical when precisely employing such sandwiches. Finally, increasing the core thickness also led to a significant increase of the compression strength of the TCS structure.

4.3.2 Mechanical behaviour of the TCS structure supported in MD

Three different designs of the TCS structures (GC4, GC5, and GC6) were tested experimentally under quasi-static compression loading conditions. For GC4, GC5, and GC6, three repeated specimens each were tested. The specific dimensions of the TCS structure specimens are shown in Table 3.8.

Figure 4.15, Figure 4.16, and Figure 4.17 show the measured typical load-displacement responses of TCS structures GC4, GC5, and GC6, respectively. For the responses, the TCS structure shows a minimal initial non-linear response, which was probably due to initial machine compliance and the non-perfect parallel face of the upper skin sheet. Next, the TCS structure exhibited a linear response, as shown in Stage 1, up to the first peak load. Then a sudden drop load occurred, as shown in Stage 2; this was due to fibre micro-buckling failure at the lower angle of the corrugated core, which can be seen on the captured photos (Figure 4.18). Subsequently, the core struts and flat core members interlocked together in the fractured zone (the fractured fibre and matrix) due to restrain the lower face sheet. Due to this interlock, in Stage 3 the structural resistance load increased again to second peak load. In this stage, the core struts showed varied visible elastic buckling deformation towards the load axis, as can be seen in the montage photo (Figure 4.18). Then, one of the core struts was damaged close to the lower face sheet, due to the propagation of damage in the load response gradually decreasing until the entire fracture of the core across the width of the sandwich, as seen in the Stage 4 captured photo (Figure 4.18). The fractured core again formed short core struts with an angle of more than 60^{o}. In Stage 5, due to a second local elastic buckling of the core across the width of the TCS structure, the force response trace increased non-linearly again to the third peak load. After reaching the third peak, the load dropped rapidly (see Stage 6) as the TCS structure fractured entirely and caused structural non-stability. It can be concluded that the mechanical

behaviours and damage mechanisms of the TCS structures are quite different when supported in MD compared with CD.

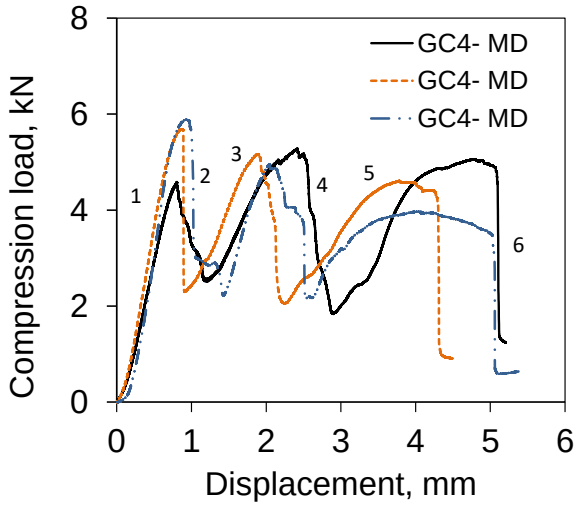

Figure 4.15: Load-displacement compression response of GC4 TCS structure supported in MD

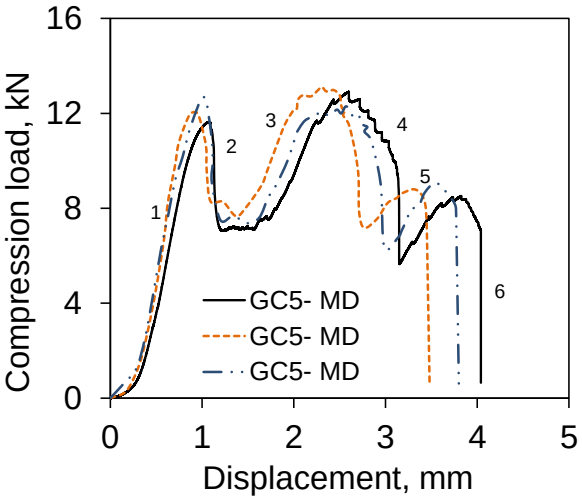

Figure 4.16: Load-displacement compression response of the TCS structure GC5 supported in MD

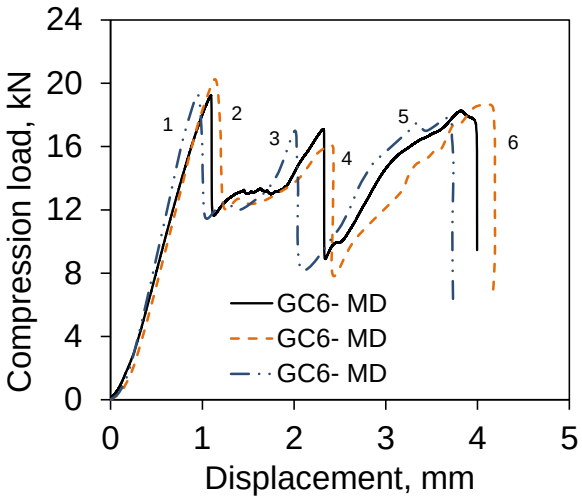

Figure 4.17: Load-displacement compression response of the TCS structure GC6 supported in MD

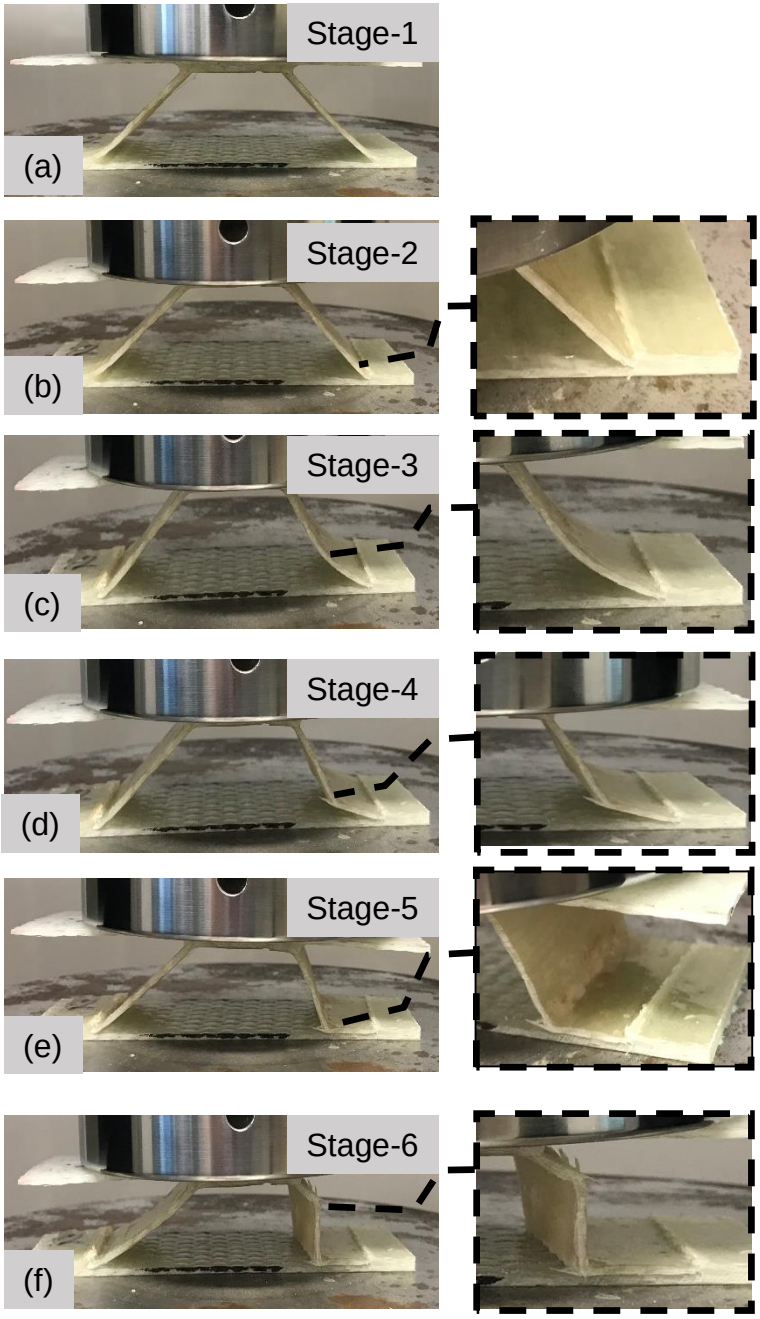

Figure 4.18: Montage of all stages of deformation and damage modes of single-cell GC4 TCS structure under quasi-static compression loading supported in MD

Figure 4.19 shows the quasi-static compressive response of one specimen each of GC4, GC5, and GC6 supported in MD. As shown in Table 3.8, the TCS structures GC4, GC5, and GC6 have different core thicknesses. GC4 exhibited more deformation than GC5 and GC6 due to twice the core elastic buckling (as explained in the previous section). When increasing the core thickness by 50% as in GC5, the strength of the TCS structure increased by 70%. Increasing the core thickness by 100%, as in GC6, enhanced the sandwich strength by 300%. Although the composite core thickness

increased, these responses have comparable trends of load-displacement. It can be concluded that increasing the core thickness significantly has a non-linear effect on the strength of the TCS structure. Therefore, decreasing the core thickness needs be accounted for very cautiously during design of a composite corrugated core sandwich.

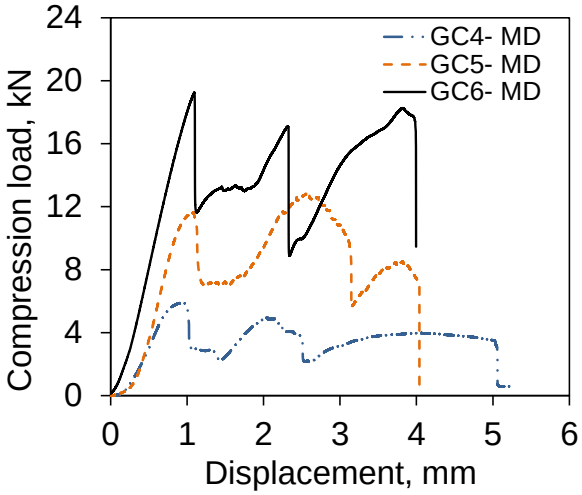

Figure 4.19: Load-displacement compression response of the three different types of TCS structure, GC1, GC2, and GC3, supported in MD

4.3.3 **Comparison between TCS structure supported in CD and MD**

Figure 4.20 shows the load-displacement response of the TCS structures GC2 and GC5 under quasi-static load, using CD and MD support types, respectively. With the CD support type, the case of SL: 90 mm was selected to compare with the MD case because TCS structure with this case has roughly comparable strength in the CD as in the MD support conditions. However, the gradient of the loading response for CD supported is less than for MD supported. In other words, the TCS structure with CD support is more flexible to deform, while the TCS structure shows extra stiffness with MD support.

Furthermore, in the CD condition, the TCS structure exhibited a two stage load-displacement response, but with MD support the TCS structure experienced six stages. The latter showed self-recovering due to the core densification, i.e., TCS structure offered again a strengthening after failure of the core strut. This characteristic makes the TCS structure give superior protection for the small parts and wires laid in the core cavity. However, this feature is missing with traditional cores, such as foam and honeycomb cores. The results also showed that these TCS structures are highly anisotropic, and their mechanical properties when supported in the CD have variable strength/stiffness and are entirely different when supported in the MD. Moreover, in

CD test the lower face sheet showed bending deformation while in MD is compression deformation without noticeable movement. Therefore, the anisotropic behaviour of the TCS demonstrates a significant advantage in employing these TCS structures for different engineering applications.

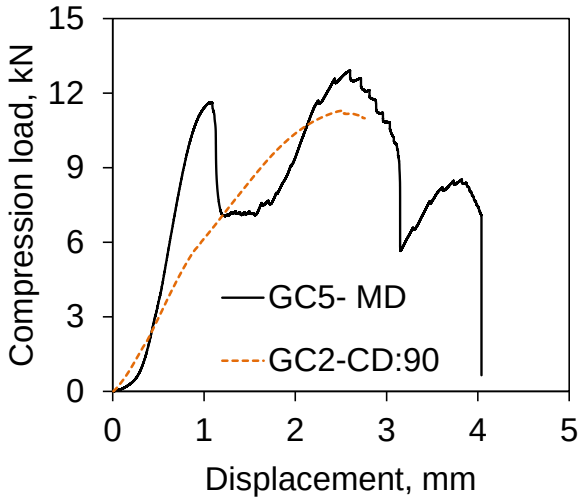

Figure 4.20: The comparison of the load-displacement compression response of TCS structures supported in CD and MD

4.3.4 Damage mechanism of the TCS structure

Visible evaluation damage was carried out on the TCS structures after being exposed to quasi-static compression load. As tGC1 and GC4 have similar geometrical parameters, they were chosen for the damage evaluation of CD and MD support conditions. Table 4.3 shows the damage mode results of the TCS structures of GC1 and GC4. No de-bonding damage was observed (i.e., in-plane shear failure) between the face sheets and corrugated core due to there being a larger contact area between them, and the appropriate properties of adhesive of Techniglue also prevented the de-bonding failure, (Techniglue, 2017). However, the dominant damage mode was core struts fracture in all four CD supported cases. Furthermore, due to force moment in the core angles, a barley whitening trace was observed, as shown in Figure 4.11(b). The fracture mode of the core angles preceded the core struts fracture in the MD supported case, as well as no de-bonding damage being seen. In previous research (Jin et al., 2013, Xu et al., 2016), it was that core struts fracture is the only damage mode of the composite core. However, from the current study, it can be concluded that the core angle damage can also be a dominant damage mode of the core which affects the TCS structure strength/stiffness. Therefore, the latter damage mode needs to be considered

and examined under different loading conditions, particularly when the TCS structure is supported in MD.

Table 4.3: Damage modes of the TCS structure under quasi-static compression loading condition supported in CD and MD

Specimen ID		De-bonding	Core struts fracture	Upper angle damage	Lower angle damage
GC1	CD-SL 86	---	xx	x	x
	CD-SL 90	---	xx	x	x
	CD-SL 94	---	xx	x	x
	CD-SL 98	---	xx	x	x
GC4	MD	---	xx	xx	xx

*Symbol (---) refers to no damage, (x) weighting damage, and (xx) core struts damage

4.3.5 Influence of core relative density on mechanical behaviours of the TCS structure

Estimation of the relative density (ρ_C) of the corrugated core by dividing the density of the corrugated core (ρ) by the overall density of the core (ρ_o) is essential to characterise the mechanical properties of the TCS structure. The relative density of the single-cell core ρ_c is calculated by Equation 4.2:

$$\rho_c = \frac{\frac{h_c}{\sin w}+2t_c*\tan\frac{w}{2}+0.5\left(l_1-t_c*\tan\frac{w}{2}\right)}{h_c*\frac{\cos w}{\sin w}+2t_c*\tan\frac{w}{2}+0.5\left(l_1-t_c*\tan\frac{w}{2}\right)} * \frac{t_c}{h_c} \qquad 4.2$$

Where t_c and h_c are the core thickness and height, respectively, l_1 is the length of the short span, and w is the corrugation angle. With a CD supported condition, the strength of all TCS structures was plotted as shown in Figure 4.21, while with an MD supported condition the average value of the strength of three tests was plotted; this was due to the comparable strength values of the TCS structure specimens of the same group. Note that the first peak load was selected with MD loading condition. Figure 4.21 shows that at minimal core's relative density the TCS structures strength showed small

discrepancy. However, increasing the core relative density led to a linear increase of the TCS structure strength having a large discrepancy with different support conditions. In the case of MD, the strength of the TCS structure showed non-linearity with the core relative density.

Figure 4.22 shows that increasing the core's relative density significantly increased the TCS structure's stiffness, in particular with MD supported conditions. In contrast, with CD supported conditions, the increase of the core's relative density had less effect on the TCS structure's stiffness. This was attributed to high deformability of the TCS structure members with CD support conditions under quasi-static loading. It can be concluded that the core relative density has a significant effect on sandwich strength/stiffness. In addition, the TCS structure behaves as a brittle structure when supported in the MD.

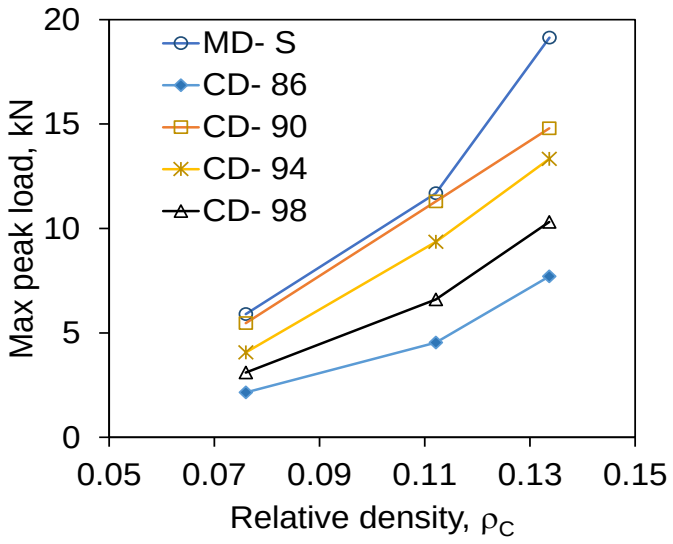

Figure 4.21: The initial peak load related to the TCS sandwiches' supporting conditions of CD and MD

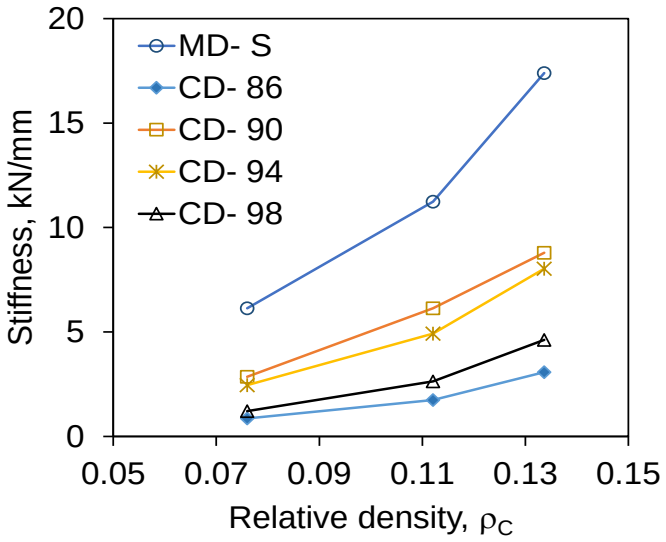

Figure 4.22: Structural stiffness related to the TCS sandwiches' supporting conditions of CD and MD

4.3.6 Influence of relative density on the energy absorption capability of the TCS structure

The energy absorption capacity (U_{AE}) can be considered an indication of materials' and structures' ability to withstand load conditions until their failure. Physically, the energy absorption capability of materials and structures is the area under the curve of the fore-displacement response, which can be calculated by integrating the load-displacement curve up to a load of breaking the specimen. Equation 4.3 has been utilized to calculate the energy absorption of the TCS structure.

$$AE = \int_0^{\delta} p(\delta).\, d\delta \qquad 4.3$$

Where AE is the absorbed energy, *p* is the quasi-static compression load, and δ is the crosshead displacement. Figure 4.23 shows the energy absorbed by the TCS structures GC1, GC2, and GC3 as a function of core relative density under quasi-static compression load. All the CD support conditions have been considered and plotted. Note that in the CD cases the energy absorption involves a small amount of energy absorbed by the lower face sheet, see Appendix B. In the MD support condition, the average value of the energy absorption has been plotted due to convergence of the TCS structure results. At the lowest core relative density, the TCS structure showed minimum energy absorption due to low strength response and earlier sandwich failure. However, with increasing core relative density, the TCS structure energy absorption significantly increased due to high core resistance and tolerable deformation.

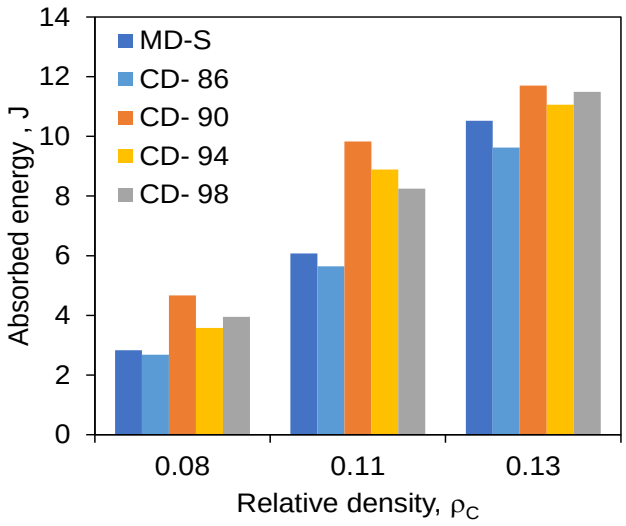

Figure 4.23: Energy absorption ability of the TCS structures related to core relative density supported in CD and MD

4.4 TCS Structure under Low-Velocity Impact

In this section, the impact behaviour, failure mechanism, and energy absorption capability of the TCS structure is considered under low-velocity impact. Different designs of TCS structures were tested. Firstly, the impact energy was chosen at the visible damage threshold energy of the composite parent materials, then impact tests were performed beyond this visible damage threshold energy.

4.4.1 Impact test at visible damage threshold energy

4.4.1.1 Force-time response of the TCS structure

Low-velocity impact tests were performed on three specimens of the TCS structure (GC7) using a flat (FH), hemispherical (HH), and conical head (CH). The kinetic energy of the impact events was approximately the visible damage threshold energy of the composite materials, which was calculated from Equation 3.9.

Figure 4.24 shows the force-time response of TCS structures impacted by these three impactor heads. There was a difference between the impact responses of the TCS structure according to the type of impactor head, such as the initial load slope, peak load, and structural time response. With the FH, the initial slope of the force-time response and impact peak force were higher than for the CH. This was because the FH led to converting the entire impact energy to TCS structure resistance without penetration of the impacted area, and mostly the impact force applied on the core struts. While, with the HH, mostly the impact energy transferred to the core struts compression, followed by member deformation of the TCS structure, such as upper face bending and core strut elastic buckling. It can be seen that, after the first peak force, the response showed a rapid drop; this was mainly due to the elastic core buckling, which was followed by the second peak force. In contrast, as the upper face sheet of the TCS structure semi-penetrated, the impact peak force decreased to a minimum level with the CH. Decreasing the impactor radius means a reduction of the contact stiffness parameters of the impacted area; thus, the upper face sheet is exposed to penetration (see Eq. 3 of Appendix C).

With the FH, the impact time was the minimum due to high resistance of the sandwich, which caused faster bounce back of the impactor head, and the TCS structure showed less deformation, as shown in Figure 4.25. However, due to the larger deformation of the core struts and upper face sheet bending, the impact time with HH was longer than with the FH. Decreasing of impactor radius, as in the CH, led to

increasing the impact time due to the semi-penetration of the TCS structure members (Figure 4.26). It can be concluded that the shape of the impactor heads has a significant influence on the TCS structure's response under low-velocity impact, particularly at the visible damage threshold energy of the composite materials.

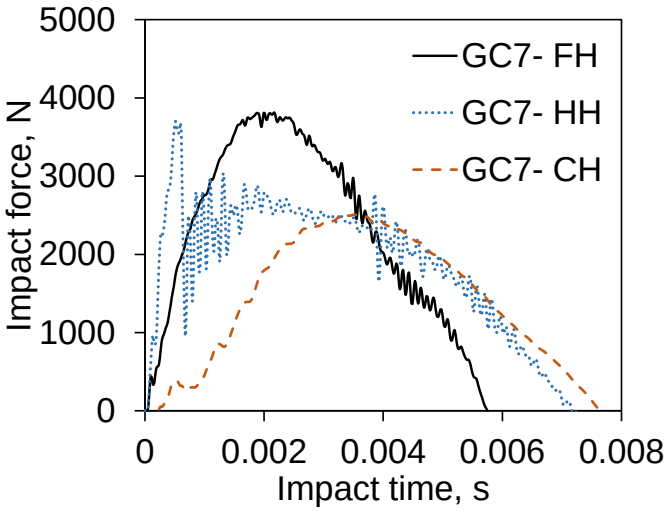

Figure 4.24: Force-time response of GC7 TCS structure under low-velocity impact with flat, hemispherical and conical heads

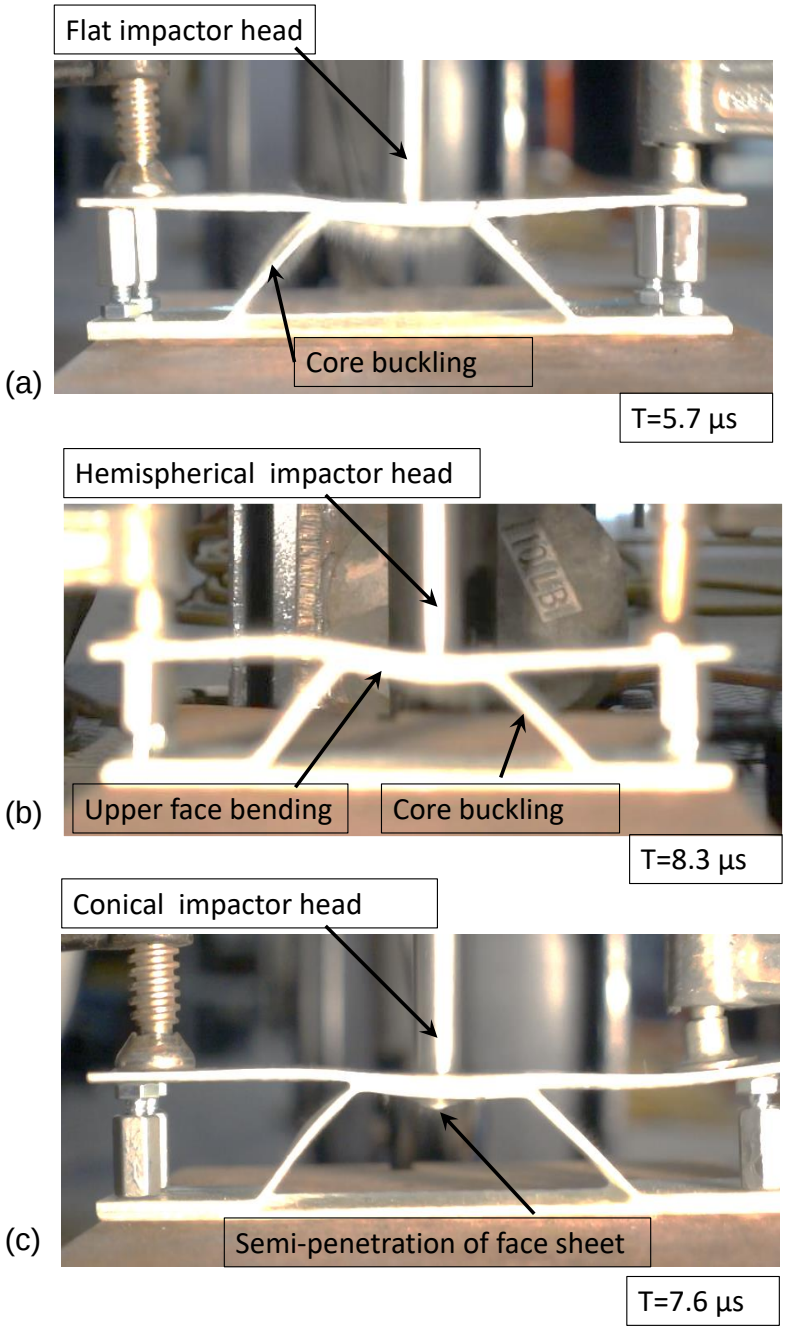

Figure 4.25: Captured photos of impact events of GC7 TCS structures with three different impactor heads, (a) Flat, (b) Hemispherical, and (c) Conical

4.4.1.2 Visible damage evaluation

A visible damage evaluation was performed on the GC7 TCS structures to gain more information about the damage modes post low-velocity impact using the three different impactor heads. Visual inspection of the top view of the impact area revealed that the flat and hemispherical heads caused barely visible impact damage (BVID); in other words, no exterior damage was visible or little damage existed with the FH and HH,

as shown in Figure 4.26. The impact traces of the FH and HH were a white ring trace and a whitened circular damage area, respectively. The white areas were due to matrix cracks and delamination of the top plies of the upper face sheet. However, the conical head caused very little clearly visible impact damage (CVID) in the form of semi-penetration of the top surface, as Figure 4.26 illustrates.

From the captured photos (Figure 4.27) of the transverse section of the TCS structure, the de-bonding damage mode between the upper face sheet and core can be seen for FH and HH. The HH caused internal core damage, which consisted of a small tear in the upper core angle. This was because of the high flexural deformation of the upper flat core member combined with core shear stress. This is contradictory to the observed damage mode with a CH, which showed no de-bonding and no core damage. The most obvious finding to emerge from this study is that the upper face sheet has not shown visible damage at the visible damage threshold energy.

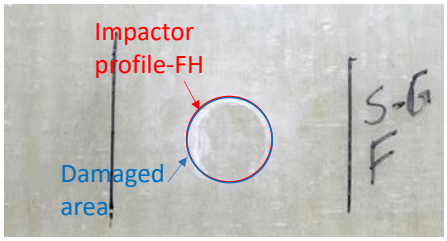

(a)

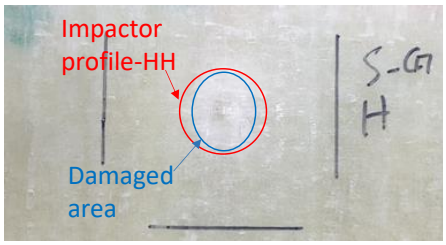

(b)

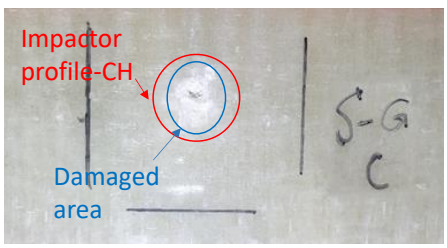

(c)

Figure 4.26: Top view of the impacted area (experimental); (a) Flat, (b) Hemispherical, and (c) Conical heads

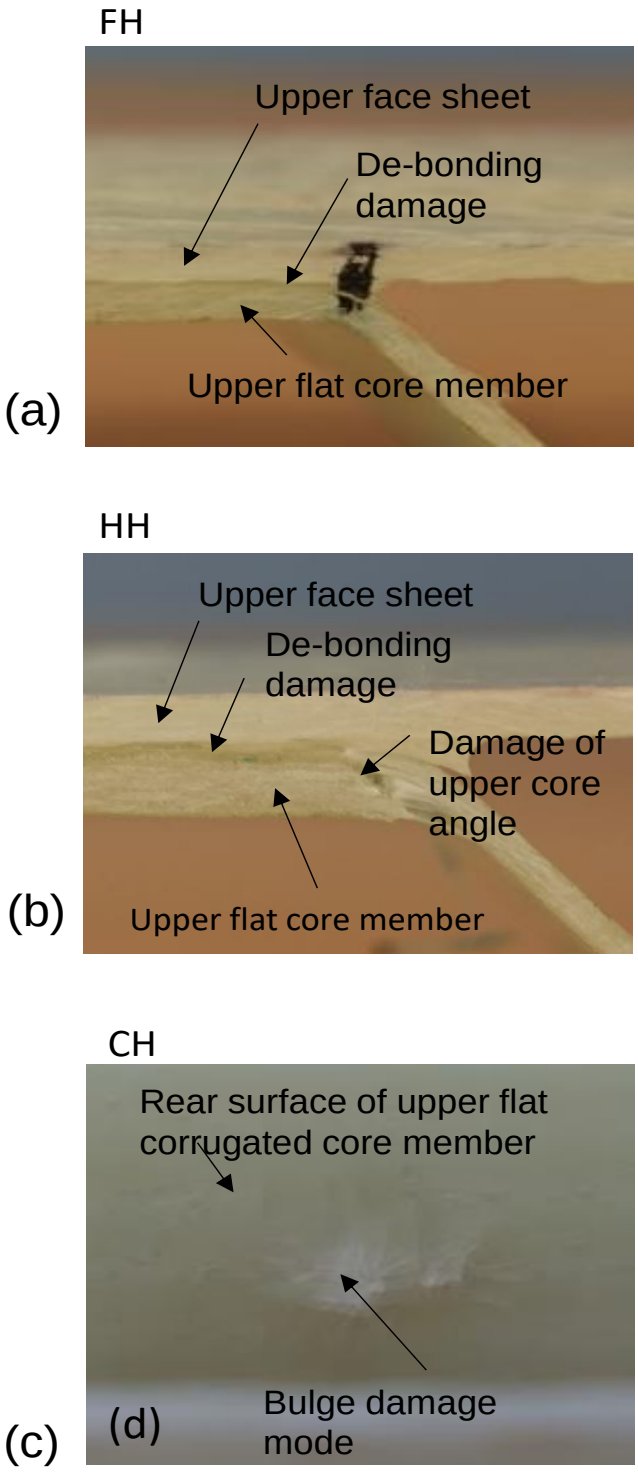

Figure 4.27: Captured photos of transverse section of the GC7 TCS structure, (a-b) Flat and hemispherical heads, respectively, and (c) Damage trace of the internal surface of the core with conical head

4.4.1.3 Microscopic damage evaluation

A microscopic investigation was performed on the impacted area of the GC7 TCS structure, as shown in Figure 4.28. It was decided to inspect the micro-damage of impacted area by using a JCM-6000 Electron Microscopic focused on the cross-sectional of the longitudinal direction (i.e. with core direction). Figure 4.28 (a, and c) provides clear views of matrix damage from the FH and HH, respectively. Furthermore, delamination of glass fibre plies using FH and HH is also evident in Figure 4.28 (b and d, respectively). However, with the CH, local crushing and indentation occurred, including matrix cracks and fibre breakage of the upper plies of the skin sheet impacted, as shown in Figure 4.28 (e). The matrix damage commenced and progressed along the fibre directions. Moreover, as expected, the first plies of the upper face sheet showed more serious fracture than the back plies of the impacted zone, which also showed matrix crack and fibre breakage, see Figure 4.28 (f). It can be concluded that, although the upper skin showed barely visible impact damage, microscopic investigation of the cross-sections of the impact areas showed that the FH and HH can cause more dangerous and hidden damage. Thus, this leads to stiffness degradation of the TCS structure and ultimately may cause catastrophic failures of the structure components. However, this is not the case when using the conical impactor head; it caused visible and intense damage on the impact area.

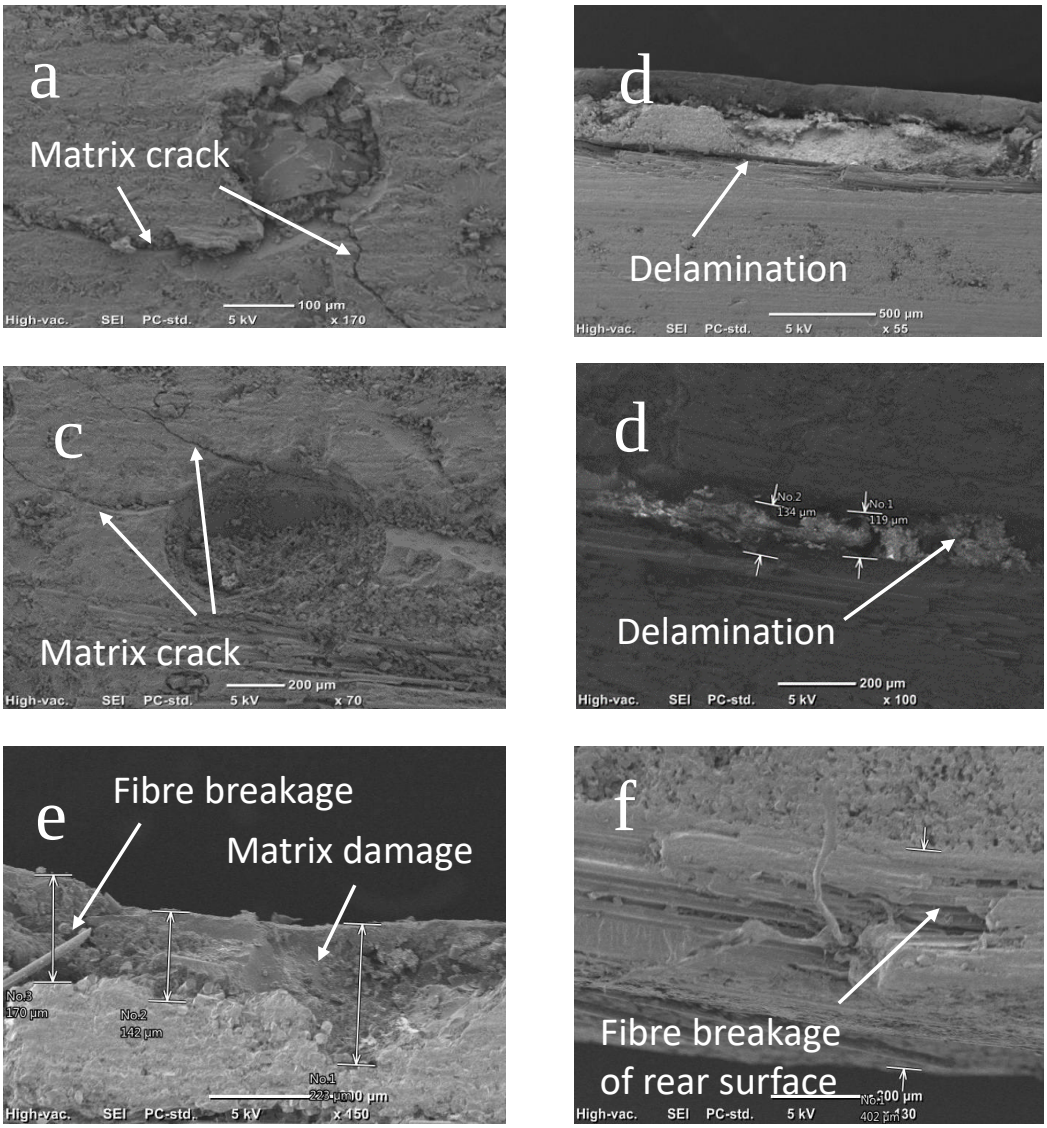

Figure 4.28: Electron-Microscopic images of the cross-section of the impacted damage area of GC7 TCS structure, (a-b) Flat head, (c-d) Hemispherical head, and (e-f) Conical head

4.4.1.4 Energy absorption of TCS structure

During an impact event on structure components, the material failure absorbs a portion of the impact energy while the structural deformations absorb the remaining impact energy. As mentioned previously, the kinetic energy of the tests of the GC7 TCS structure was at the visible damage threshold energy. Figure 4.29 shows the energy absorption of the TCS structure specimens after impacted with three different impactor heads. As seen before, the FH and HH produced the highest impact resistance accompanied with composite core deformation (Figure 4.24), which significantly increased the structural energy absorption (see Eq.7, Appendix C). On the contrary, with the CH, the materials fracture of the TCS structure absorbed the major part of the kinetic energy. This means that the kinetic energy was absorbed in terms of contact energy (see Eq.4, Appendix C) in which the impactor radius is a significant factor. In addition, the contact area of impactor head has effect on the involvement of the composite fibre during impact. The flat head contact higher fibres and they transfer the stress and deformation resulting in highest energy absorption. The least fibre contact and deformation is happened with conical nose, and as a result the least energy absorption. The spherical is between these two cases and its contact start from single point and increase to large area, therefore the absorbed energy will be between the flat head and conical head. It can be concluded that, under low-velocity impact, the TCS structure absorbed different levels of impact energy due to the impactor shape. In addition, the results of this testing indicate that the TCS structure was capable of absorbing impact energy at the visible damage threshold energy without fractures of the sandwich.

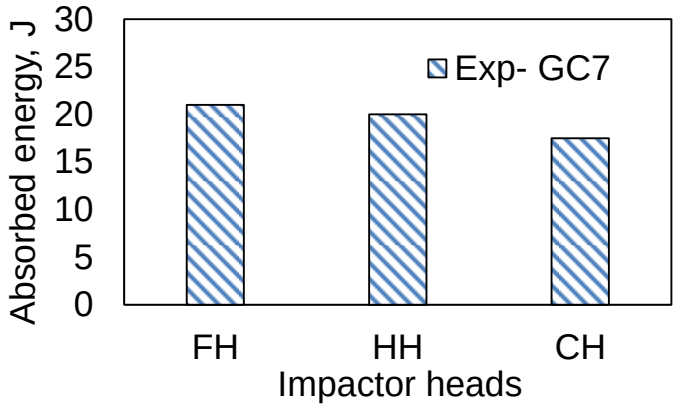

Figure 4.29: Energy absorption of the GC7 TCS structure impacted with three different impactor heads

4.5 Impact Tests beyond Visible Damage Threshold Energy

4.5.1 Influence of core thickness on sandwich impact behaviour

Low-velocity impact tests were performed beyond the visible damage threshold energy on designs of the TCS structure with different core thicknesses. Equation 3.9 was employed to estimate the visible damage threshold energy of the composite parent materials of the TCS structure. GC8 and GC9 specimens had core thicknesses of 1.45 mm and 2.09 mm, respectively. The effect of this core thickness on the impact behaviour of the GC8 and GC9was investigated at a kinetic energy of (40J). Figure 4.26 shows the force-time response of the TCS structure impacted by three different impactor heads FF, HH, and CH, respectively. The force vs. time comparison revealed that the TCS structures for GC8 and GC9 have different magnitudes of peak force with a roughly similar trend of loading response, as shown in Figure 4.30 (a-c). Increasing the core thickness from 1.45 to 2.01 mm led to enhancing the structural impact resistance, and the peak force value increased between 25% and 45% with all impactor types. However, all cases showed an abrupt drop in force after the first initial peak load. This is attributed to local damage of the impact area and initiation of the elastic buckling of the core struts. After this drop in force, the impact resistance increased again to a second peak load followed by another drop in force due to core struts crashing (particularly with FH and HH). The descending impact force was associated with a noticeable fluctuation due to the matrix cracking, fibre breakage, and delamination of the core struts.

The impact force increased again (Figure 4.30 a-b) due to the flexural resistance of the upper face sheet (in most cases). The third force increase can be considered a third delayed impact resistance. This phenomenon indicated premature core crush, which mitigates the impact energy followed by delayed face sheet bending. The impact time of the GC8 TCS structure was shorter than for GC9 due to earlier core crush (Figure 4.30).

The captured photos (Figure 4.31 d-h) also showed a severe fracture of the upper angle of the corrugated core, due to out-of-plane shear and bending coupling force, followed by large deformation of the upper face sheet, with the FH and HH. However, with the CH, the stubby core struts of GC9 showed no core crushing due to semi-penetration, and inertial stabilization of the core struts. As well, no noticeable upper face sheet bending was observed, as shown in Figure 4.31 (i). Moreover, a closer look at the Figure 4.31(d-i) shows a dust cloud on the top skin and the core due to the impact

event, which reflects the shape of impact force distribution on the top surface and perturbations of the surface. It can be concluded that the increase of core thickness can increase the TCS structure's impact resistance and reduce impact time and core buckling; however, it cannot reduce the core crushing.

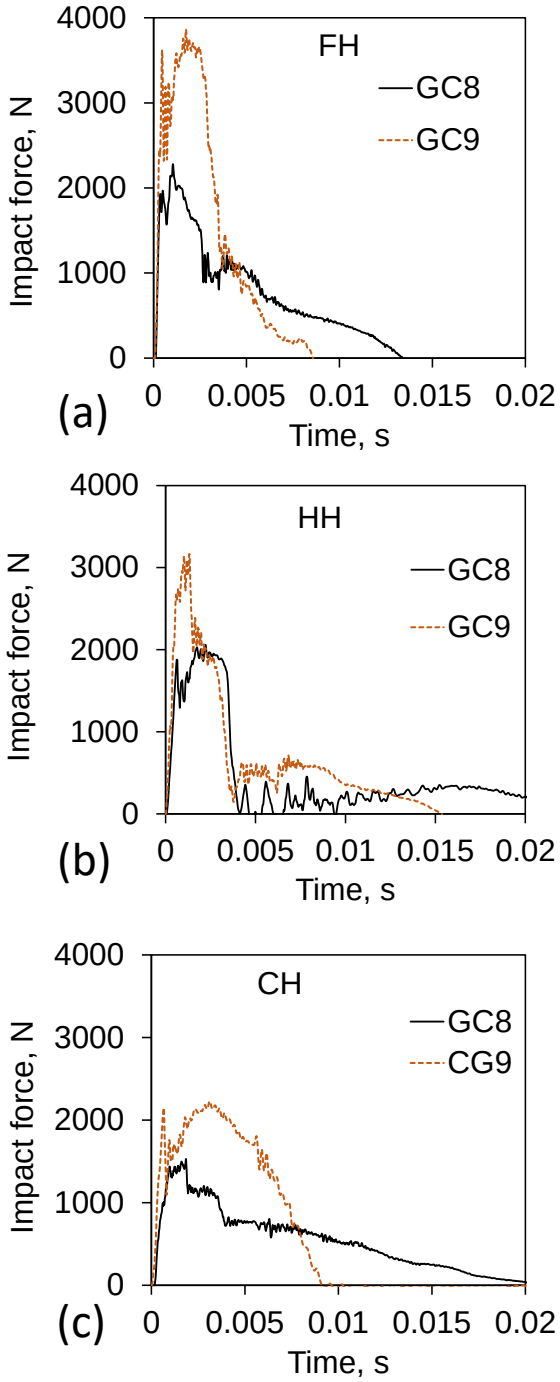

Figure 4.30 Force-time response of the GC8 and GC9 TCS structures, (a) Flat, (b) Hemispherical, and (c) Conical head

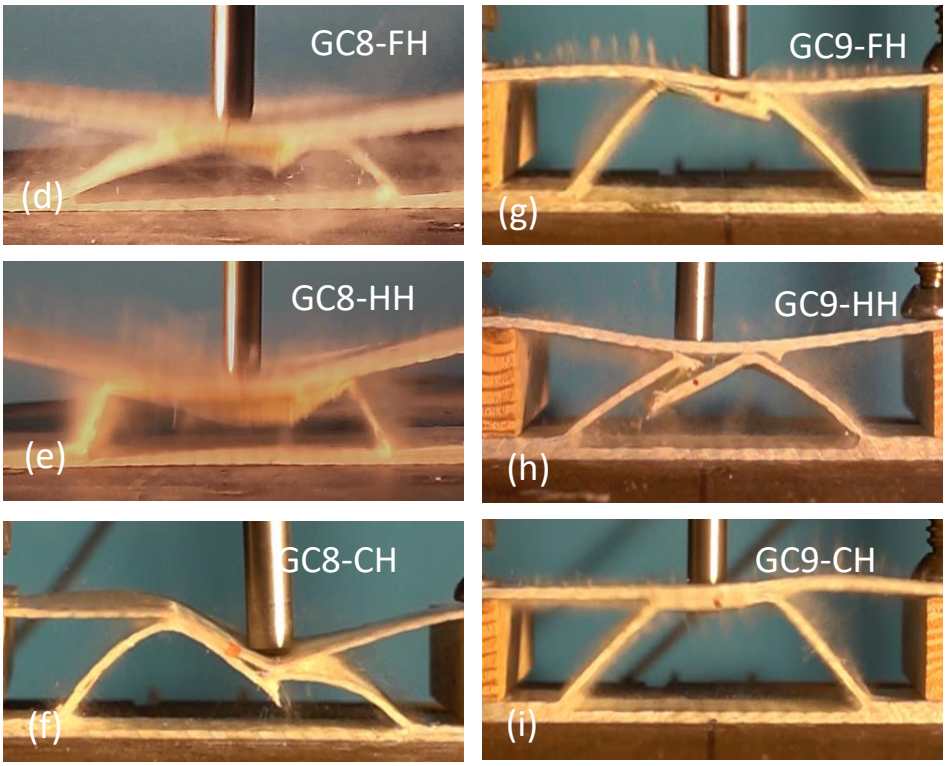

Figure 4.31 Captured photos of impact event of GC8 and GC9 TCS structures, (d-g) Flat, (e-h) Hemispherical, and (f-i) Conical head

4.5.2 Influence of core height and short span length

The influence of the core height and short span length (as in GC9 and GC10) on the TCS structure impact behaviour was investigated under low-velocity impact at constant kinetic energy (40 J). GC9 and GC10 specimens had core heights of 27.5 mm and 30.1 mm, respectively. Figure 4.32 (a-c) reveals that the core height has a direct effect on the impact response of the TCS structure. The initial peak force decreased with increasing core height even though both GC9 and GC10 specimens showed a similar response trend (with FH, HH, and CH). Figure 4.32 (a-c) also shows that the impact time response of the TCS structure in GC10 was either similar or longer than that in GC9 due to the considerable movement of the impactor head and the large deformation of the upper face sheet. Figure 4.33 (d-i) indicates that the upper angle joint of the core is the weakest point in the TCS structure, and severe damage occurred at this point. This damage was due to the coupling of the kinetic out-of-plane shear force and high bending force of the core struts, which exceeded the shear and tensile strength of the parent material. Although the increase of the core height showed a minimal effect on the impact force, however, the impact time and elastic deformation

of the TCS structure increased significantly, which means increasing the mitigation level of the impact energy. On the other hand, the extension of the core height led to a reduced short span length of the core. It can be seen that lowering the span length (L_1) from 33.3 mm (GC9) to 27.1 mm (GC10) has no significant effect on core damage, due to inertial stabilisation of the core struts (Kazemahvazi et al., 2012, Schneider et al., 2015).

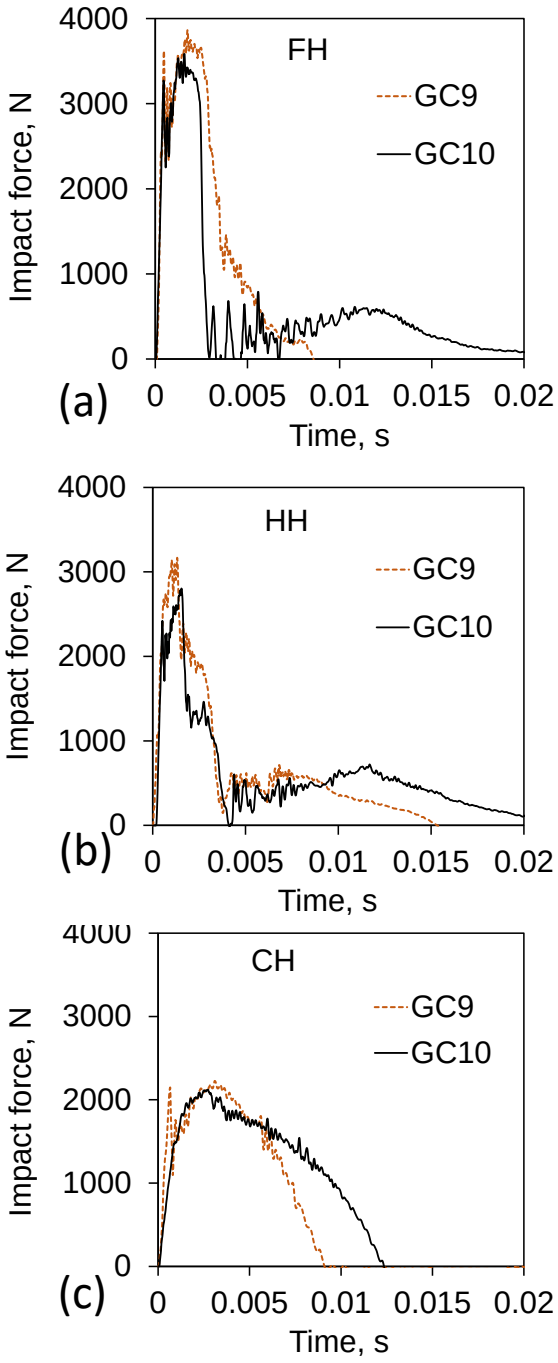

Figure 4.32 Force-time response of the GC9 and GC10 TCS structures (a) Flat, (b) Hemispherical, and (c) Conical head

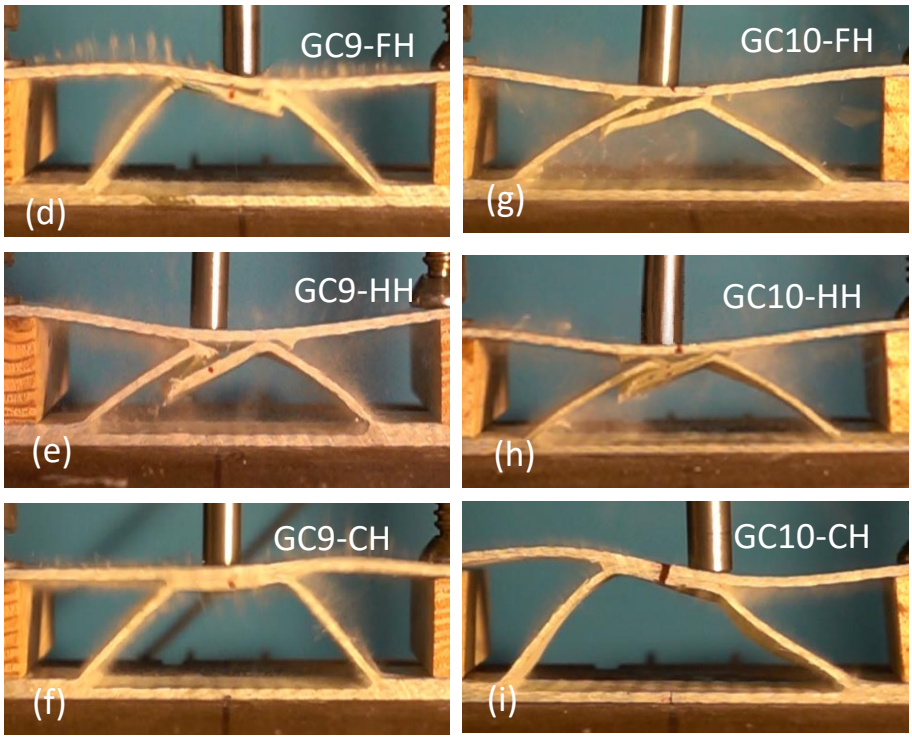

Figure 4.33 Captured photos of impact event of GC9 and GC10 TCS structures, (d-g) Flat, (e-h) Hemispherical, and (f-i) Conical head

4.5.3 Influence of the core thickness's to the TCS structure height ratio on the impact peak force

The sandwich skins have a noticeable influence on impact resistance; particularly, their contribution has been clearly seen in the third stage of the force-time response. Therefore, the thickness of the skins has been considered so as to investigate the relationship between impact resistance and the ratio of core thickness to TCS structure height (i.e., t_c/H instead of t_c/h). Figure 4.34 shows the variations of the peak force of the TCS structures as a function to the ratio of core thickness to TCS structure height. The peak forces increase linearly with the increase of the ratio of core thickness to TCS structure height, regardless of the type of impactor head. The structural peak force resistance exhibited closest values at a lower ratio of core thickness to TCS structure height. This was attributed to instant damage of the core member under the impact event. However, the rate of increase differs, depending on the impactor heads. The discrepancy between the FH and CH slopes increased with the increase of the core thickness to TCS structure height ratio, due to minimal bending of the sandwich TCS structure with FH. While, the impact force with CH was lower than with HH and FH

due to the reduced impactor radius, and thus the contact stiffness parameter decreased (Sevkat et al., 2013). The maximum peak force (3910 N) was obtained with the flat head impactor at a core thickness to TCS structure height ratio of 0.058. On the other hand, the minimum peak force (1010 N) occurred with the conical head impactor at a core thickness to TCS structure height ratio of 0.04.

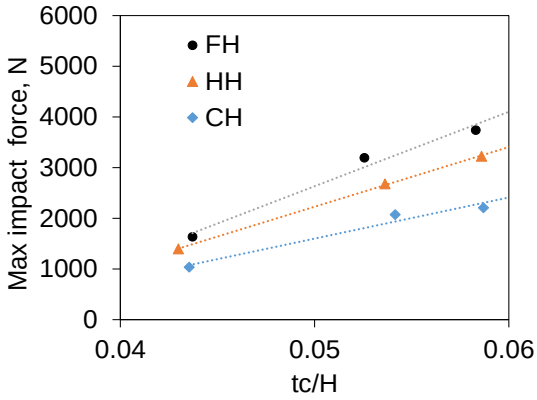

Figure 4.34: Peak force vs. core thickness to the TCS structure height ratio under low-velocity impact

4.5.4 Identifying the critical design parameters

Figure 4.35 shows a Terraplot trace of the influence of the composite core parameters (core thickness, height, and short span length) and total structural weight on the TCS structure's specific strength. It can be seen that a greater core thickness significantly increased the structural specific strength (Figure 4.35 a). This was attributed to an increase of the core cross-section, thus expanding the core struts' shear strength and the delay of the core struts' buckling. However, the structural specific strength minimally improved with an increase of the core height (Figure 4.35 a).

On the other hand, the extension of the short span length led to reduced specific strength of the TCS structure, as shown in Figure 4.35 (b). This was due to the increase in the elastic flexural response of the upper face sheet and flat core members. Figure 4.35 (c) shows that the core height and short span length have a similar effect on the structural specific strength. Figure 4.35 (d) indicates the relationship between the sandwich's specific strength with the aspect ratio of the short span-to-core height (L_1/h) and of the short span-to-long span (L_1/L). It can be seen that the increase of the short span to core height aspect ratio led to a decrease in the structural specific strength. This was due to the increase of the short span width, which led to enhancing the local

bending deformation of the upper face sheet and flat core member, resulting in the reduction of structural impact resistance. The maximum value of the structural specific strength was observed when the short span-to-core height aspect ratio (L_1/h) was close to one. The further reduction of L_1/h may have created stress concentration at the impact area due to the reduced load distributing area. On the other hand, the aspect ratio of the short span to long span had a minimal influence on the TCS structure's specific strength.

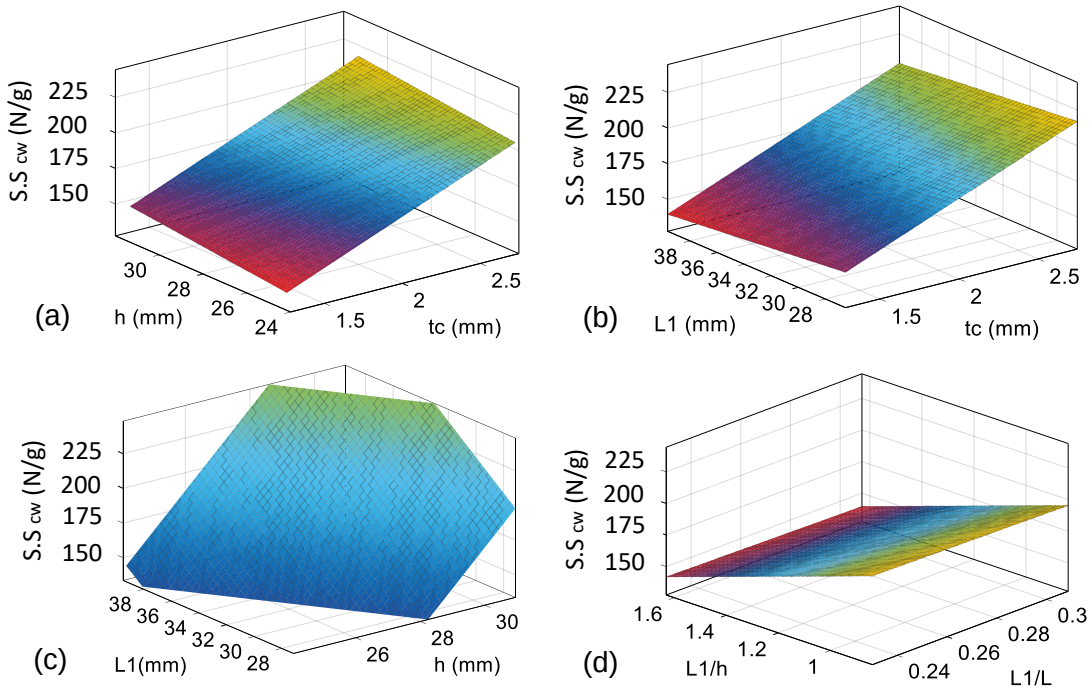

Figure 4.35: TerraPlot response of the TCS structures' specific strength as a function of the core geometrical parameters under low-velocity impact (a) Specific strength vs. core thickness and core height; (b) Specific strength vs. core thickness and short span; (c) Specific strength vs. short span and core height; (d) Specific strength vs. short span to core height ratio and core pitch

The combined effect of the geometric parameters on the energy absorption capability (calculated by Eq. 1) of the corrugation sandwich systems is illustrated in Figure 4.36. The TCS structure's capability to absorb energy was more sensitive to the core height, as well as the core thickness (Figure 4.36 a). The TCS structure absorbed the greatest energy with the highest core height and thickness. The increase in core thickness led to enhancing the structural impact resistance while raising the core height

extended the impact displacement (high deformation). However, a shorter span length (node width) exhibited a minimal influence on the structural energy absorption compared to the core thickness and height (Figure 4.36 b-c). Furthermore, the increase in both aspect ratios slightly increased energy absorption (Figure. 4.36 c). This was because increasing those aspect ratios led to more structural deformation; thus, the sandwich energy absorption was greater. All the above discussions indicate that the most critical design parameter of the trapezoidal composite sandwich is core thickness (tc) followed by core height (h). The optimal design of corrugated core sandwich can be obtained when L1/h approaches unity, as shown in Figure 4.36 (d).

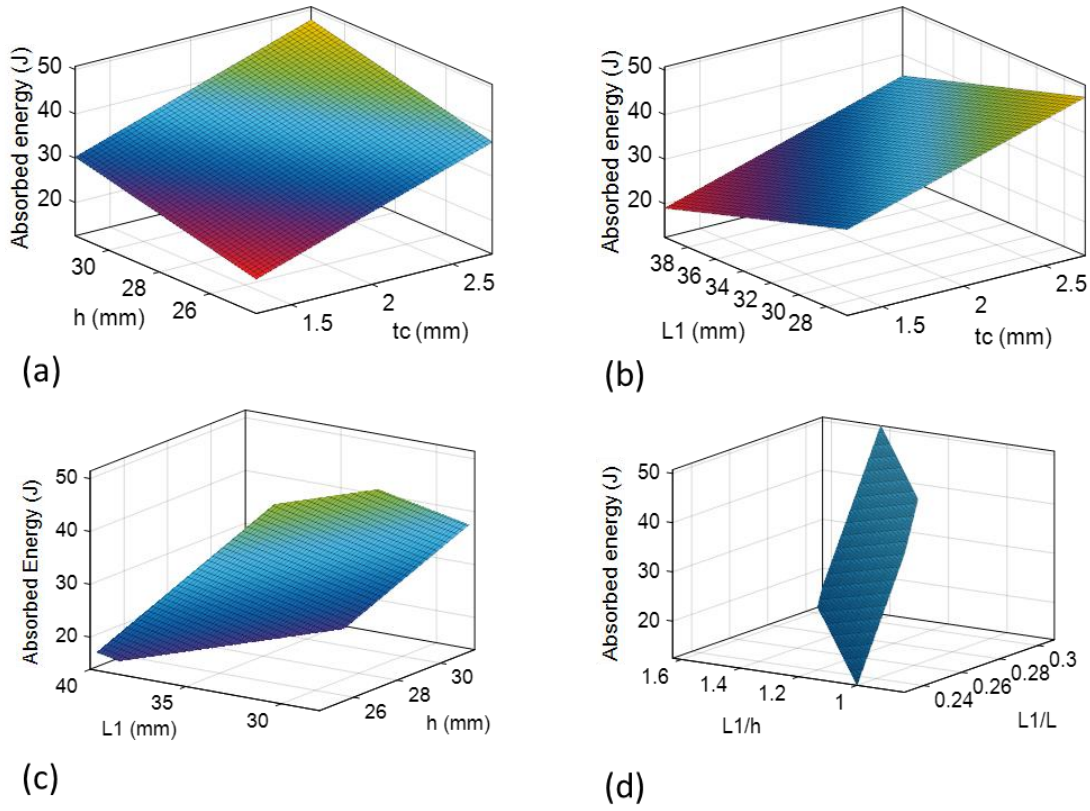

Figure 4.36: Energy absorption ability as a function of the core geometrical parameters under low-velocity impact, (a) Absorbed energy vs. core thickness and core height; (b) Absorbed energy vs. core thickness and short span; (c) Absorbed energy vs. short span and core height; (d) Absorbed energy vs. short span to core height ratio and core pitch

4.5.5 TCS structure impact response relative to theoretical model

The experimental results of the dynamic/impact response of the TCS structuresGC8, GC9, and GC10 were compared with the theoretical outcome. The initial peak forces of the experimental response of the TCS structures were chosen for comparison by assuming that, in this stage, the core struts had not undergone a large deformation. Theoretically, during the loading of the TCS structures, the core struts undergo the axial compression load before deformation and failure. The axial compression load (F) was obtained by utilizing the stress equation of the core struts (Malcom et al., 2013).

$$\sigma_c = \frac{\pi^2 E_c}{12K^2.sf}\left(\frac{t_c.\sin\omega_1}{h_c}\right)^2 \quad 4.4$$

$$F = n.A_c.\sigma_c \quad 4.5$$

Where σ_c and E_c are the core strut stress and Young modulus of the parent materials of the core struts in the fibre direction respectively, K is constant depending on the end condition of the core struts, in this study, it is 0.7, and (*sf*) is the shape factor depending on the geometry of the impactor head, which is found from the experimental results. The t, h, and w are the thickness, height, and angle of the core member, respectively, n is the number of the core strut, and A_c is the cross-section of the core strut.

Table 4.4 shows the variation between the obtained results and the outcome of the axial compression load of Equation 4.5 for TCS structures GC8, GC9, and GC10. With flat impactor heads, there is an acceptable agreement between the experimental results and the theoretical outcome. The variation in the impact force of GC8, GC9, and GC10 with FH was about ± 2%. It can be concluded that the large contact area of the impactor head caused more distribution of the load on the core struts before larger deformation of the core and severe damage of the upper skin sheet. However, with hemispherical heads, the variation ranged between ± 7% and 15%. This was even more with conical impactor heads, between ± 28% and 50%. These variations are due to the local bending and damage of the upper face, with hemispherical and conical heads, respectively.

Therefore, experimental shape factors were produced to approximate results. The equation of the core stress as introduced in Equation 4.4 was normalised by shape factors of 0.9 and 0.7 for the hemispherical and conical heads, respectively, reducing the variation to less than ±10%. Overall, it can be concluded that the theoretical equation for estimation of TCS structures' impact force can be adopted with the flat impactor heads, while for pointed impactor heads, shape factors are needed.

Table 4.4: Comparing the initial impact peak force of experimental and theoretical outcomes

Sample ID	Exp. (N)	Theoretical (N)		% Variation	
		Without shape factor	With shape factor	Without shape factor	With shape factor
GC8-FH	2260	2195	2195	2	2
GC8-HH	2040	2195	1981	-7	2
GC8-CH	1674	2154	1556	-28	7
GC9-FH	3302	3387	3387	-2	-2
GC9-HH	2937	3387	3057	-15	-4
GC9-CH	2147	3246	2345	-51	-9
GC10-FH	2841	2747	2747	-2	3
GC10-HH	2266	2632	2376	-15	-4
GC10-CH	2052	2632	1902	-51.2	7

4.5.6 Influence of the impactor weight on TCS structure behaviours

Figure 4.37 shows no significant disparity in the peak load values obtained from the TCS structure response (GC11) impacted by HH having three different impactor weights, 15.7, 8.4 and 5.4 kg, respectively, when keeping the total energy constant at 54 J. Hemispherical impactor head was used in these tests. There is a considerable discrepancy in the impact time response. The more massive the impactor weight, the longer impact time due to its high momentum which allowed more contact time between the impactor and target, accompanied by semi-penetration, as shown in Figure 4.38 (a). Moreover, with a more massive impactor weight, there is also an oscillation of the load-time curve due to significant damage in the upper face sheet plies and core short span plies. The impact time reduced with decreasing impactor weight due to a rapid rebound of the impactor without penetration (Figure 4.38 b-c).

4.5.7 Influence of the impactor weight on the damage area

Gwydion 2.5 commercial software was employed to further analyse the photos of the impact damage area, which impacted by HH having three different impactor weight. Figure 4.38 (d-f) illustrates an actual 3D damaged area of the TCS structure impacted by large, medium, and small weights. Decreasing the impactor weight from 15.7 to 5.4 kg led to a significant reduction in the damaged area, from 674 to 186 mm^2, due to lessening momentum. In all cases, the damaged zone spread to a wide area of the skin layers, and core short span started from the upper lamina, continuing to the lower lamina. A little trace of the bulge was also detectable in the lower face of the core short span. The image analysis shows that the indentation or the depth of the impacted zone was 0.54 mm with the most massive impactor head and less than that on reducing the impactor weight. For the same level of kinetic energy, the increase of impactor weight extended the impact time and extended the damaged area at the impact zone.

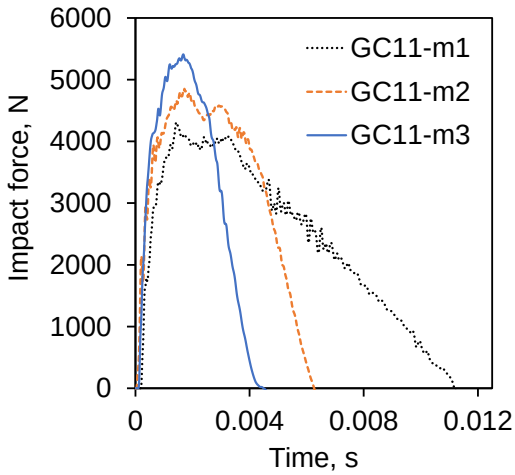

Figure 4.37: Impact force-time curves of GC11 TCS structure exposed to three different impactor weights using HH at a constant level of kinetic energy 54 J

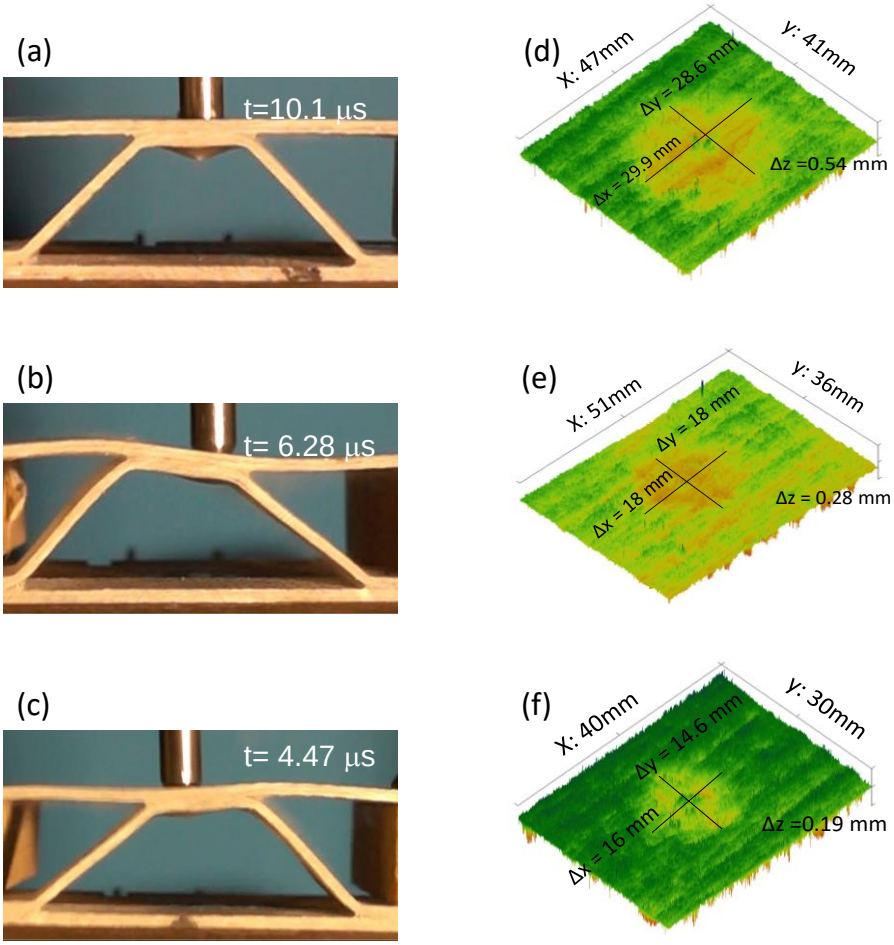

Figure 4.38: Impact event of the GC11 TCS at constant kinetic energy of 54 J using HH with having three different impactor weights,15.7 kg, 8.4 kg and 5.4 kg : (a-c) captured photos of impact event, and (d-f) damaged area of upper face sheet

4.5.8 Influence of TCS structure's weight on impact peak force

Figure 4.39 shows the influence of the total weight of TCS structures GC8, GC9, GC10, and GC11 on the impact peak force. Each value of the experimental dots represents the average value of the three tests. It is quite interesting that the outcomes have a non-linear relationship. Whereas the TCS structure's impact resistance increased about 130% on increasing the TCS structure's weight by 100%, however, increasing the TCS structure's weight to 200% led to a significant increase of the impact force to 420%. This phenomenon is an indication of the high structural efficiency of these TCS structures. This efficiency of the structure is a sign of robustness with a relatively light design. Moreover, the output from the empirical formula can be utilized for estimating the TCS structures' impact force by TCS structure weight. It needs to be noted that this deduced formula is valid with TCS structures having same parent materials and being roughly similar in the thicknesses of their upper face sheets and corrugated cores.

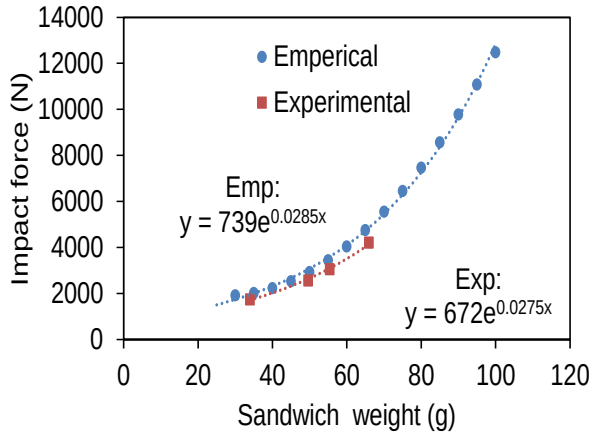

Figure 4.39: Experimental and numerical maximum impact force vs. TCS structure weight

4.5.9 Comparing composite corrugated core with other cores

The most relevant mechanical property of the structures to consider is the specific energy absorption (SEA), this is to improve the energy absorption and design more efficient mechanisms of collapse of the structures (Zhang et al., 2017). The specific energy absorption is the energy absorbed per unit mass of the materials. However, there is a lack of understanding of TCS structures' specific energy absorption under low-velocity impact, compared with the specific energy absorption of other traditional

cores. Table 4.5 shows the SEA behaviour of various sandwich cores. It can be seen that the proposed composite corrugated core has SEA of 0.88 J/g at 2400 N, which is higher than the other composite sandwiches including foam core (0.2 J/g at 2500 N) and hollow plastic ball core (0.6 J/g at 2700 N). Although, rubber foam ball core and composite honeycomb core exhibited high impact forces of 5800 N and 4000 N, respectively, the proposed trapezoidal composite corrugated core, interestingly, showed the highest SEA value. Furthermore, the proposed trapezoidal composite corrugated core showed excellent performance terms of SEA compared to triangular and foam aluminium core and steel sinusoidal core.

Table 4.5: Comparison of the current study's single-cell composite corrugated core with published core sandwiches

Sandwich skins	Core type	I.F(N)	SEA (J/g)
Glass fibre composite	Trapezoidal composite corrugated core (present study)	2400*	0.88*
Carbon fibre composite	Foam core (Anderson and Madenci, 2000)	2500	0.2**
Carbon fibre composite	Plastic ball core (Zhang et al., 2017)	2700	0.60
Carbon fibre composite	Rubber foam ball core (Zhang et al., 2017)	5800	0.20
Carbon fibre composite	Composite honeycomb core (Anderson and Madenci, 2000)	4000	0.15**
Aluminium	Aluminium honeycomb core (Shin et al., 2008)	2100	0.1**
Aluminium	Aluminium foam core (Shin et al., 2008)	2600	0.05**
Steel	Steel sinusoidal core-$_{AACC}$ (Zhang et al., 2014)	4200	0.04**

(*) average value, and (**) calculated value

4.5.10 Comparison of impact behaviour of multi-cell with single-cell TCS structures

All previous tests were performed on single-cell TCS structures at a constant level of kinetic energy. However, in practical applications, a TCS structure possesses multiple cells. Therefore, a fabricated multi-cell TCS structure, GC12, was measured with different levels of impact energy (25 J, 32.5 J, and 40 J). This was to gain a conspicuous idea about the multi-cell impact response and to compare this with single-cell TCS structures. Figure 4.40 (a-c) shows the impact force-time curve and structural energy absorption of GC12. It can be seen that the structural response showed a comparable response to the single-cell TCS involving initial peak load, due to the contact force of the upper face sheet, followed by a small drop of the force and again increasing to the second peak load. After the second peak force, the force-time curve descended gradually due to the low level of the impact kinetic energy (25 J), which was at about the visible damage threshold of the TCS structure. Subsequently, the TCS structure strongly resisted the impact loading.

The multi-cell TCS structure's force-time response showed a single and double plateau region with 32.5 J and 40 J, respectively. The first plateau region was attributed to elastic core buckling and de-bonding between the upper face and core short span, as shown in Figure 4.41 (b and c). The second plateau region was due to a delay in upper face flexural bending (Figure 4.41c). The corresponding impact time of the multi-cell TCS structure increased with a greater impact energy level.

The absorbed energy capability of the TCS structures was estimated by Equation 4.3. From Figure 4.41 (a-c), the multi-cell TCS structure absorbed impact energy due to deformation of the sandwich (as with 25 J). However, with 32.5 J and 40 J, the TCS structure's defamation was accompanied by fracture modes, such as the back face of the upper skin and the core short span de-bonding, fibre break, and bulge damage, as shown in Figure 4.41. Compared to the single-cell TCS structure, the multi-cell one not only increased the impact force but also provided functional, structural integrity and composite action between adjacent cells. Moreover, the multi-cell TCS structure showed a non-linear ductile behaviour, which cannot be seen in the traditional core sandwich (Ude et al., 2013, Han and Cho, 2014). Therefore, it can be concluded that a single-cell TCS structure shows the worst scenarios for impact behaviour and damage mode compared to a multi-cell TCS structure under low-velocity impact.

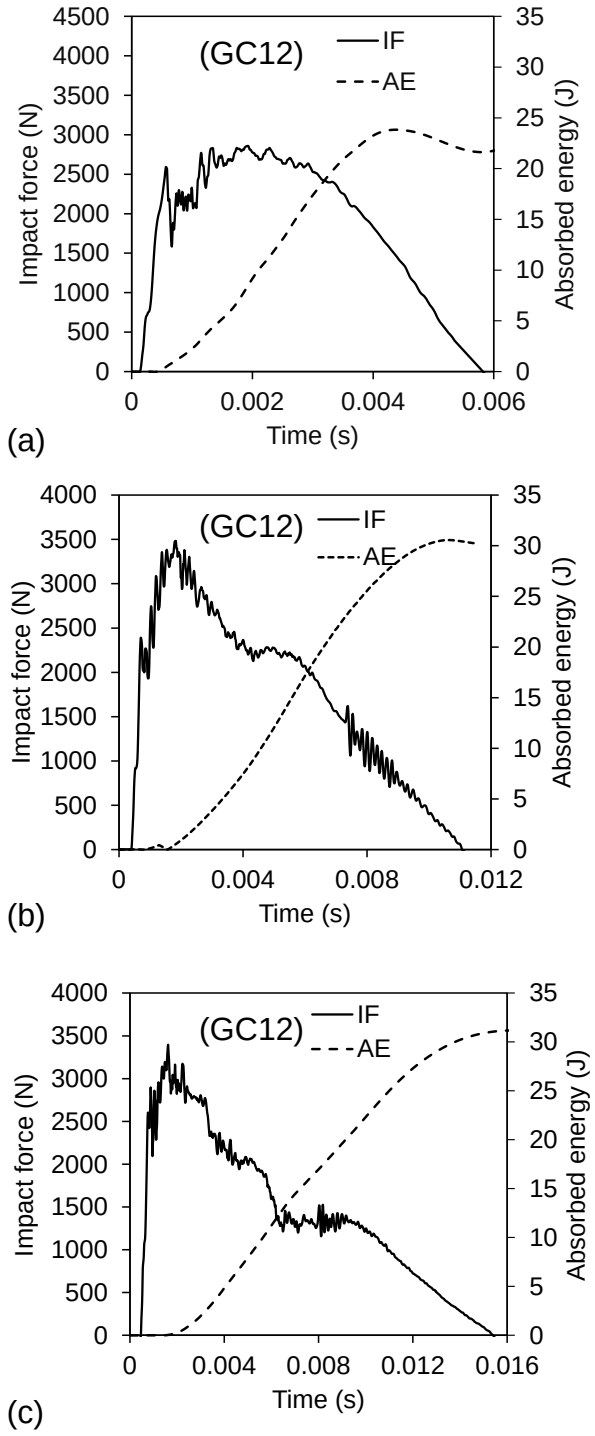

Figure 4.40: Impact load-time response of GC12 TCS structure with three different kinetic energies: (a) 25 J; (b) 32.5 J; and (c) 40 J

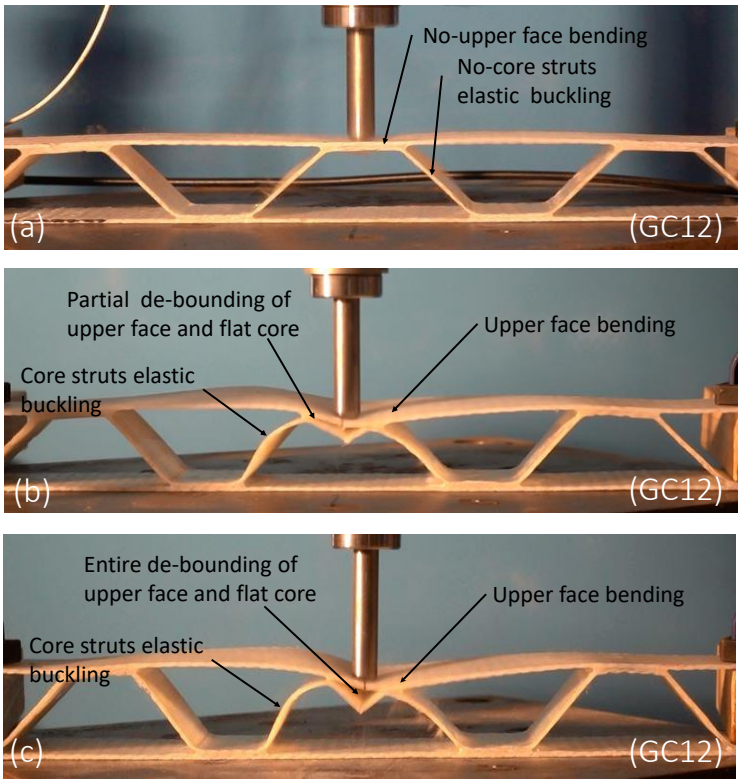

Figure 4.41: Captured photos at the impact event of GC12 TCS structure: (d) 25 J; (e) 32.5 J; and (f) 40 J

4.6 Summary

This chapter presented the experimental outcomes for TCS structures. First of all, the mechanical properties of the woven E-glass fibre reinforced epoxy composite materials and epoxy resin were identified by tensile, compression, shear tests. These tests showed that the woven E-glass fibre reinforced epoxy composite has an elastic linear response and is a brittle material. As well, their mechanical properties were summarized for use in FE modelling of the TCS structure under different loading conditions.

The quasi-static compression mechanical behaviour and failure mechanisms of the TCS structure were investigated for the single-cell TCS structure supported in both core direction (CD) and machine direction (MD). This experimental investigation showed that the TCS structure possesses variable strength/stiffness when supported in CD, and height strength/stiffness was obtained when the supports were under the core struts, i.e. under the lower core angle. In addition, increasing the core thickness led to significantly increased strength/stiffness. However, such TCS structures showed

various mechanical behaviours when supported in MD, possessing higher stiffness compared to the former.

Moreover, the failure mode of the CD supported TCS structure showed core strut damage followed by deformation of the core angles, while the MD supported TCS structure showed damage of the lower core angle, followed by several stages of core strut damage. It can be inferred that the TCS structure is a highly anisotropic composite sandwich, which promotes utilizing it in numerous engineering applications. In addition, the compressive strength of the trapezoidal composite corrugated core was compared with the Ashby chart that includes several sandwich cores having different design and materials. It was found that the trapezoidal composite corrugated core significantly exceeds the other core with different designs and materials.

Experimental tests were extended to investigate the impact behaviour and damage mechanism of the TCS structure under low-velocity impact at and beyond the visible damage threshold impact energy of the parent materials. Results revealed that the visible damage threshold impact energy of the TCS structure is higher than that of the composite parent materials by about 25%. Moreover, the effects of the core parameters, specifically core thickness and core height, were also investigated. The core thickness significantly affected the impact behaviour of the TCS structure. An increase in the core thickness led to increasing the TCS structure's impact strength/stiffness, however increasing the core height led to a greater energy absorption capability of the TCS structure. In addition, increasing the impactor weight at the same level of kinetic energy led to an extended damage area. In terms of the specific energy absorption (SEA), the trapezoidal composite corrugated core showed superiority compared to other cores having different designs and materials. Finally, the impact behaviour and energy absorption capability of a multi-cell TCS structure were investigated. The main conclusion was that the multi-cell core showed an excellent impact behaviour and energy absorption; in addition, the single-cell composite core showed the worst scenario for the damage mode. Therefore, it is recommended to use multi-cell TCS structures instead of single-cell for the next investigation under low-velocity impact.

Chapter 5

Developing finite element model of the designed TCS structure

5.1 Introduction

This chapter aims to develop a model for the simulation of a designed TCS structure using finite element (FE) modelling. The simulation includes the analysis and investigation of all the critical parameters of the TCS structure under quasi-static compression load and low-velocity impact. This modelling has been incorporated into the research for this thesis because experiments may not provide the means to investigate the independent effects of all critical parameters, such as deformation and stress concentration at the composite corrugated core members. In addition, experimental tests are more expensive than numerical modelling.

Firstly, the FE model was correlated with the experimental tests and then samples of the model were used to investigate the requested parameters. Furthermore, the numerical modelling was extended to optimize the geometrical parameters of the TCS structure under quasi-static compression load. Finally, the numerical model was also used to analyze the impact and failure mechanism of the TCS structure at low-velocity impact with different loads/kinetic energies.

5.2 Modelling the Designed TCS Structure

In this study, the commercially available FEA software ANSYS was used to simulate the TCS structure which was designed and investigated by experiments as described in previous chapters. The ANSYS tools of APDL and Workbench explicit dynamics were employed to simulate the designed TCS structure (See Appendix D).

A three dimensional configuration (3-D) of the TCS structure GC1 under compressive quasi-static load was simulated using ANSYS APDL as shown in Figure 5.1. The dimensions of the GC1 model are given in Table 3.1.

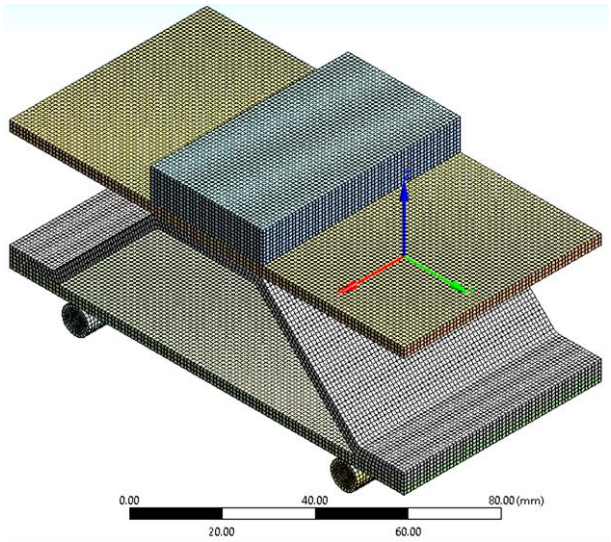

Figure 5.1: Meshing of the GC1 TCS structure with ANSYS APDL

Meanwhile ANSYS Workbench explicit dynamics was employed to simulate the GC7 corrugated core sandwich under low-velocity impact. In this case, the APDL developed model of the TCS structure was introduced to the Workbench explicit dynamics code with three different impactor head, as shown in Figure 5.2.

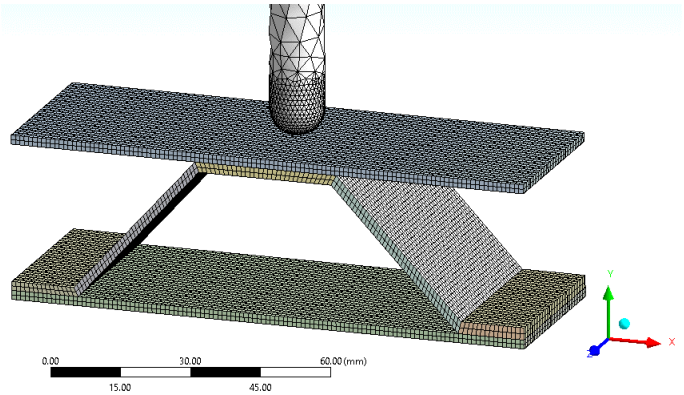

Figure 5.2: Three dimensional (3D) FE model of the GC7 TCS structure together with the HH impactor head the unit modelled by APDL then converted to Workbench explicit dynamics

5.2.1 Description of chosen element

In this study, an eight-node Solid-Shell element (SOLSH190) was chosen to mesh the TCS structures, as shown in Figure 5.3. This solid shell element is appropriate to model shell structure components with variable thickness, and it is also competent for the analysis of laminated composite materials involving various fibre orientations. Furthermore, the SOLSH190 is defined by three degrees of freedom and can create stress and strain outputs in both local (xyz) and global (XYZ) co-ordinate directions in a composite plate (Ansys_help, 2019).

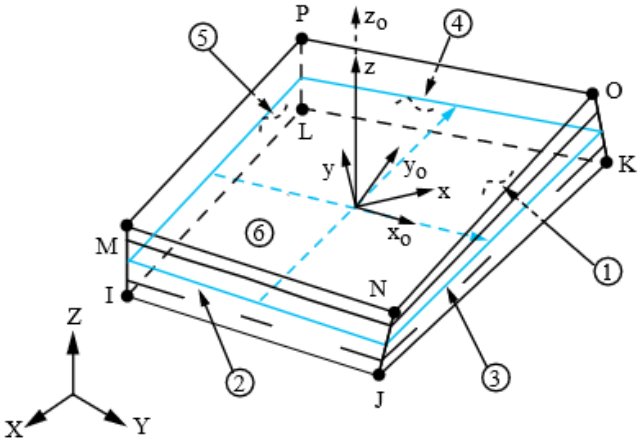

Figure 5.3: Three dimensional view (3-D) of the solid shell element (SOLSH190) with eight nodes (Ansys_help, 2019)

5.2.2 Mechanical properties of the materials

As presented in Chapters 3 and 4, the mechanical properties of the woven E-glass fibre reinforced laminate composite were obtained for analysis. Woven E-glass fibre reinforced epoxy is an orthotropic material whose mechanical properties are given in Table 4.2. This material was used to simulate the trapezoidal composite corrugated core sandwich in both implicit and explicit models while steel was selected as the impactor head for different load cases. It is worth noting that composite laminates are brittle, which means they show some elasticity behavior and then break. Therefore, material non-linearity is not activated in this modelling.

5.2.3 Mesh size

The mesh size used to simulate the corrugated core sandwich needs to be carefully considered due to the TCS structure's geometrical complexity. Moreover, the mesh

quality significantly affects the stability and accuracy of the numerical outcome. Therefore, mesh sensitivity analysis were performed on the laminated composite plate model with different element sizes, i.e., coarse, medium, and fine meshes, then the results were compared with the experimental coupon testing. In the first model, the element size was 2 mm, then decreased to 1 mm for the second and 0.5 mm for the third. In addition, the aspect ratio criteria was chosen with the element size of the model.

Table 5.1 shows the aspect ratio of the element size, which is the measurement of the deviation of the mesh's longest edge to the mesh's shortest height; the ideal value for the aspect ratio is 1. The target of these three iterations was to achieve solution accuracy within a reasonable computation time. Table 5.1 illustrates that decreasing the element size to 1 mm leads to an average aspect ratio of 1.029, and the computation time increased by 50%. Figure 5.4 indicates that at a 1 mm element size, the numerical result is in good agreement with the experimental result. In the final model, the element size was reduced to 0.5 mm, however, the computation time increased by 200% compared with the second iteration, and the numerical results showed an unnoticeable improvement, as presented in Figure 5.4. Consequently, the element size of 1 mm was chosen for the composite corrugated model sandwich numerical model in both implicit and explicit simulations. The total number of the elements in the single-cell composite corrugated core sandwich model were 136600 (SOLIDSH191), and this increased when increasing the core thickness and adding impactor head. It needs to be stated that 1 mm was chosen for the upper and lower face sheets and the corrugated core. This is because the element edges of the combined parts (upper and lower face sheets with corrugated core) need to be comparable to gain uniform node-to-node contact pairing. With the explicit model, the impactor head meshed as a rigid part, using an 8 node solid element (SOLID185).

Table 5.1: Statistics of element size details of laminate composite plate model

Iteration	Elem. size (mm)	Elem. no	Aspect ratio			
			Min.	Max.	Ave.	Time (min.)
1	2	1500	1.0028	2	1.5	20
2	1	6000	1.0028	1.26	1.09	30
3	0.5	24000	1.0028	1.05	1.02	90

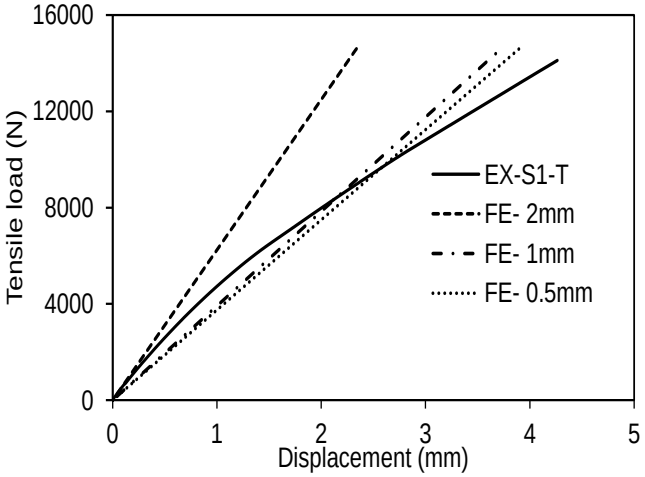

Figure 5.4: Load-displacement response of FE model of composite laminate plate

5.2.4 Non-linearity

In finite element modelling, a nonlinear structural behavior needs to be considered when the geometry, material and changes in boundary conditions are nonlinear (Madenci and Guven, 2006). In the research for this thesis, due to the large deformation of the core struts and upper face sheet, the TCS structure the model was considered to have non-linear geometry by activation of the large deformation of the solution control.

The contact between the laminae also needs to be carefully considered due to the composite laminate's orthotropic mechanical properties. The contact status between the laminae is counted as a close gap (Stolarski et al., 2018). The woven E-glass fibre reinforced epoxy composite ply is represented as an independent thin volume for entire structure members, as illustrated in Figure *5.5* (b). This was done to obtain a detailed structure deformation under loadings and to get accurate results from the numerical simulation. The fibres have been set in the middle of the model laminae (volumes) and the fibre orientation of the model was adjusted to align with the fabricated TCS structure in the experiment. In addition, the surface-to-surface cohesive nodes component was employed between the laminae as a contact of the ply-to-ply interface, as shown in Figure *5.5* (b). The surface-to-surface cohesive contact nodes have zero thickness and the mechanical properties of epoxy. This feature permits the generalization of two adjacent plies' (laminae's) specific traction-separation behaviour (Aymerich et al., 2009).

In addition, the contact of the glued parts of the TCS structure was also considered as a close gap. The surface-to-surface "contact pair" was employed for the contact pair of the TCS structure parts (upper face sheet, corrugated core, and lower face sheet) by selecting the elements (TARG170) and (CONT174) as the target and contact element surfaces, respectively.

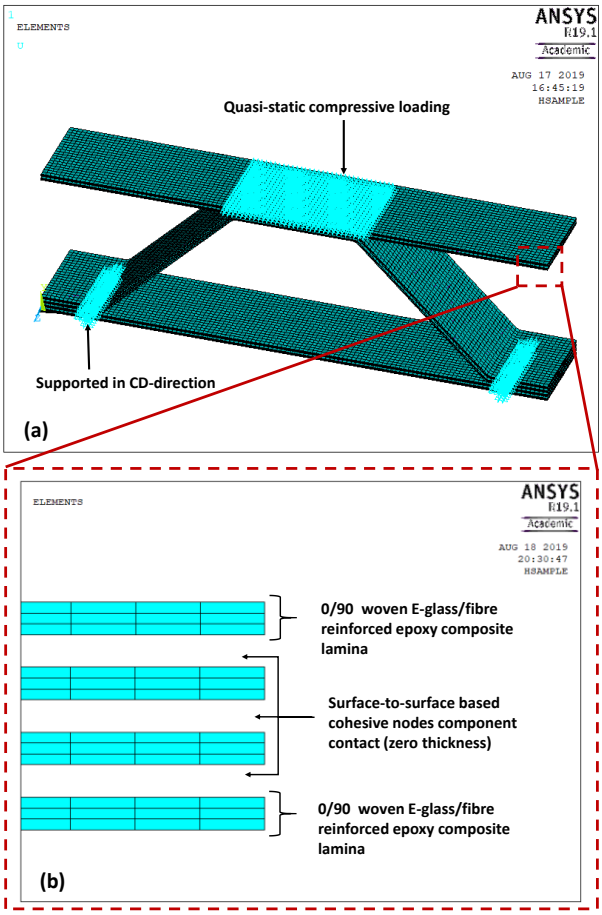

Figure 5.5: (a) The 3D FE model of the laminae of the TCS structure, (b) The surface-to-surface cohesive nodes component between the laminae as a contact of ply-to-ply interface

5.2.5 Failure criteria

The prediction of the failure mode under a specified stress or strain remains one of the unresolved issues in the numerical analysis of fibre composite laminate's mechanical properties. Therefore, numerical modelling should be based on criteria. In the (3D) finite element modelling (3D-FEM), the damage initiation of the TCS structures under loading condition was evaluated by utilizing Hashin's failure criteria (He et al., 2016, Hashin, 1980, Hashin, 1981). The Hashin approach applies four damage initiation

mechanisms: fibre tension, fibre compression, matrix tension, and matrix compression. In this modelling, the woven E-glass fibre laminate was modelled as an orthotropic elastic material. Additionally, the damage criteria were estimated based on the stress state in the fibre direction.

Failure modes of the fibre under tension: ($\hat{\sigma}_{11} \geq 0$)

$$F_f^t = (\frac{\hat{\sigma}_{11}}{X^T})^2 + \alpha(\frac{\hat{\tau}_{12}}{S^L})^2 \quad (5.1)$$

Failure modes of the fibre under compression: ($\hat{\sigma}_{11} \leq 0$)

$$F_f^c = (\frac{\hat{\sigma}_{11}}{X^C})^2 \quad (5.2)$$

Failure modes of the matrix under tension: ($\hat{\sigma}_{22} \geq 0$)

$$F_m^t = (\frac{\hat{\sigma}_{22}}{Y^T})^2 + (\frac{\hat{\tau}_{12}}{S^L})^2 \quad (5.3)$$

Failure modes of the matrix under compression: ($\hat{\sigma}_{22} \leq 0$)

$$F_m^c = (\frac{\hat{\sigma}_{22}}{2S^T})^2 + \left[\left(\frac{Y^C}{2S^T}\right)^2 - 1\right]\left(\frac{\hat{\sigma}_{22}}{Y^C}\right) + \left(\frac{\tau\sigma_{12}}{S^L}\right)^2 \quad (5.4)$$

where $\hat{\sigma}_{11}$ and $\hat{\sigma}_{22}$ are the effective normal stress tensors, and $\hat{\tau}_{12}$ is the shear stress tensor components within the plane of the composite. The X^T, X^C are the tensile and compressive strengths in the longitudinal direction, Y^T, Y^C are the tensile and compressive strengths in the transverse direction, S^L, S^T are longitudinal and transverse shear strengths. The term α is a coefficient factor that shows the contribution of the shear stress to the fibre tensile mode; the case can be considered as fully shear stress when α is 1. If the terms in the equation are equal to or higher than 1, the damage mode criteria are met, and the next damage estimation process will begin.

The damage mode is determined by calculating equivalent stresses and strains in a linear degradation after the damage initiation arrives at any of the four failure modes (Li et al., 2017).

Fibre tension:

$$\delta_{eq} = L^c\sqrt{\langle\varepsilon_{11}\rangle^2 + \alpha\varepsilon_{12}^2} \quad , \qquad \hat{\sigma}_{11} \geq 0 \quad (5.6)$$

$$\sigma_{eq} = \frac{\langle \sigma_{11} \rangle \langle \varepsilon_{11} \rangle + \alpha \tau_{12} \varepsilon_{12}}{\delta_{eq}/_{L^c}} \quad , \qquad \varepsilon_{11} \geq 0 \qquad (5.7)$$

Fibre compression

$$\delta_{eq} = L^c \langle -\varepsilon_{11} \rangle \ , \qquad \hat{\sigma}_{11} \leq 0 \qquad (5.8)$$

$$\sigma_{eq} = \frac{\langle -\sigma_{11} \rangle \langle -\varepsilon_{11} \rangle}{\delta_{eq}/_{L^c}} \quad , \qquad \varepsilon_{11} \leq 0 \qquad (5.9)$$

Matrix tension

$$\delta_{eq} = L^c \sqrt{\langle \varepsilon_{22} \rangle^2 + \varepsilon_{12}^2} \ , \qquad \hat{\sigma}_{22} \geq 0 \qquad (5.10)$$

$$\sigma_{eq} = \frac{\langle \sigma_{22} \rangle \langle \varepsilon_{22} \rangle + \tau_{12} \varepsilon_{12}}{\delta_{eq}/_{L^c}} \ , \qquad \varepsilon_{22} \geq 0$$

Matrix compression

$$\delta_{eq} = L^c \sqrt{\langle -\varepsilon_{22} \rangle^2 + \varepsilon_{12}^2} \ , \qquad \hat{\sigma}_{22} \leq 0 \qquad (5.11)$$

$$\sigma_{eq} = \frac{\langle -\sigma_{22} \rangle \langle -\varepsilon_{22} \rangle + \tau_{12} \varepsilon_{12}}{\delta_{eq}/_{L^c}} \ , \qquad \varepsilon_{22} \leq 0 \qquad (5.12)$$

Where L^C is the characteristic length, which is based on the element geometry and is introduced to normalize the elements with different size ranges.

5.3 Numerical Simulation of the TCS Structure under Quasi-Static Compression Load

5.3.1 Predicted response of the TCS structure supported in CD

A 3D FE modelling was performed on the GC1 TCS structure with APDL code. The simulation procedures were performed with a quasi-static compression load condition on the upper face sheet of the TCS structure. The normal displacement of the upper face sheet was controlled with the solution time instead of the applied force. This is to alter the asymptotic simulation load to a realistic quasi-static loading condition. The real contact points of the rollers and the lower face sheet of the sandwich were represented as having no degrees of freedom of the elements in that position.

Figure 5.6 shows the quasi-static compression load-displacement of the FE model correlated with the experimental results of a single-cell of GC1 sandwich with various support span lengths (SL). It can be seen that the FE force-displacement responses are comparable to the measured outcome in the linear stage (first stage). However, the case of the SL: 98 mm support length exhibited some disagreement with experimental results (see Figure 5.6) due to sliding the lower sandwich skin on the contact points with roller support in the experimental test. In addition, the FE model effectively predicted the non-linear stage response (second stage) of the TCS structures. This non-linear load displacement is attributed to the geometrical non-linearity of the corrugated core sandwich structures. In the second and third stages, a small deviation was seen between the numerical prediction and the experimental outcome due to a few reasons. These comprised the thickness tolerance of the tested specimens, the curvature in the inclined members (in core angles), and the existence of voids on the surfaces of the manufactured corrugation system. It can be inferred that the numerical modelling significantly simulated the sandwich deformation under a quasi-static loading condition.

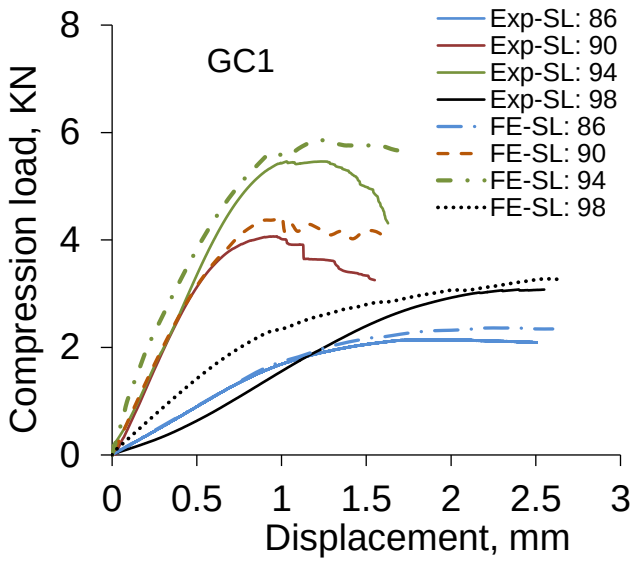

Figure 5.6: Force displacement response of the experimental and FE models of the GC1 TCS structure supported in CD

Figure 5.7 presents the GC1 TCS structure deformation and stress distribution on the sandwich members of the numerical model supported by CD for the cases of SL: 86 mm, SL: 90 mm, SL: 94 mm, and SL: 98 mm. The numerical models powerfully

showed the core struts' buckling and the lower face sheet positively and negatively bending (i.e., sagging and hogging). Furthermore, it can be seen how the core strut buckling caused local failure of the composite lamina due to exceeding the ultimate strength of the parent materials, as shown in Figure 5.8. It can be concluded that the FE images clearly showed that the support position in CD significantly affects the stress concentration of the TCS structure.

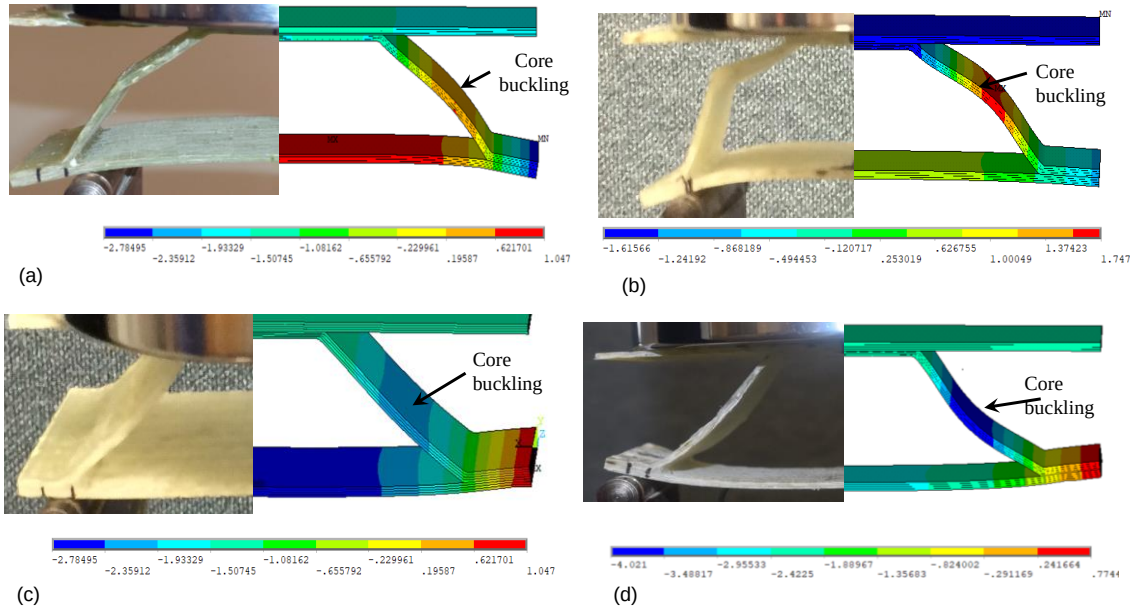

Figure 5.7: Experimental and numerical deformation of the GC1 TCS structure model under quasi-static load supported in CD, a) SL: 86 mm, b) SL: 90 mm, c) SL: 94 mm, and d) SL: 98 mm

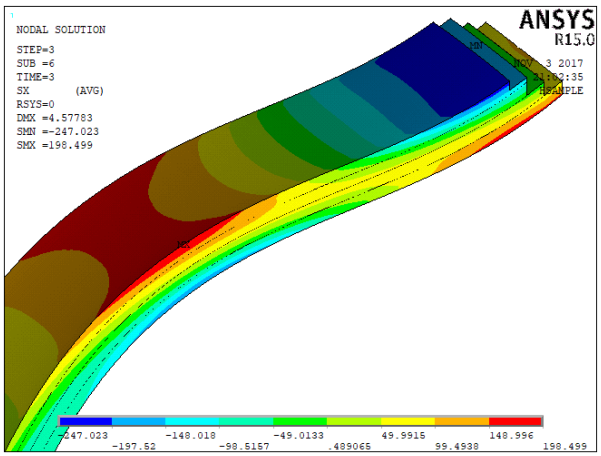

Figure 5.8: Failure stress of the composite lamina of the buckled core struts of CG1 TCS structure under quasi-static compression load with SL: 90 mm

The numerical model was also employed to investigate the deformation of the GC4 TCS structure under quasi-static compression load supported in the MD, as shown in Figure 5.9. Although the numerical outcome was slightly overestimated, the TCS structure's deformation and core struts buckling were similar to the experimental results. In addition, it showed the damage position on the core struts was due to exceeding the ultimate strength (in X-direction) of the parent materials. It can be concluded that the FE numerical model excellently predicted the complex mechanical behaviour of the TCS structures, and the FE model's results were able to confirm the experiment results. This significant correlation between the FE and experimental models strengthens the idea that this FE model can be employed to study various parameters of TCS structures under different load conditions.

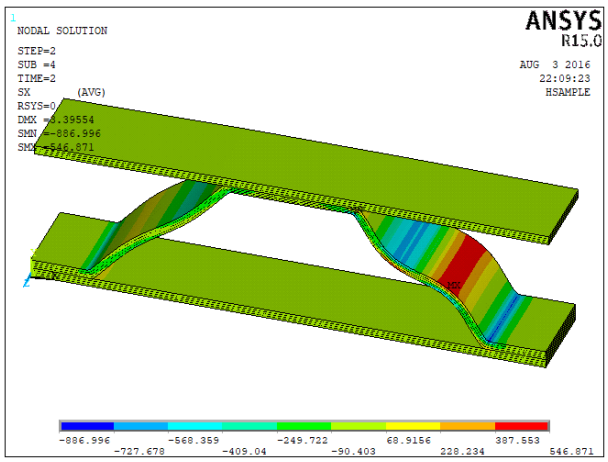

Figure 5.9: Numerical deformation of the GC4 TCS structure model under quasi-static load supported in MD

5.3.2 Effect of the support span length on stress concentration of single-cell TCS structure under quasi-static compression loading

The FE model was employed to find the stress distribution on the GC1 and GC4 TCS structures, which is not achievable through an experimental method. The geometrical profile of the TCS structure core (see the TCS structure design in Section 3.3.4) was divided into five zones. The first zone (Z1) is the lower horizontal members of the core, the second (Z2) is the lower angles of the core, the third (Z3) is the inclined members of the core (core struts), the fourth (Z4) is the upper angles of the core, and last (Z5) is the upper horizontal members of the core (short span), as shown in Figure 5.10. The stress magnitude was taken on each node along the top surface of the

corrugated core of each zone. The stress magnitude was taken in the X direction (σ_x) (i.e., the fibre direction). This was due to the high core buckling and the flattening of the core upper angle, which caused high tensile stress in that direction.

Figure 5.10 shows an unnoticeable stress concentration in Z1 of the core at SL: 86 mm and SL: 90 mm, and MD support due to free motion of that part. However, at SL: 94 mm and SL: 98 mm, tensile stress was caused on Z1 of 150 MPa and 156 MPa above the roller supports, respectively. This was attributed to the reaction force of the fixed supports.

In Z2, the supports SL: 90 mm and SL: 94 mm and MD caused stress concentrations of 215 MPa and 290 MPa, respectively, which means they exceeded the ultimate tensile and compression strength of the parent materials. This is due to the produced force moment that resulted from the core struts' buckling to the outward corrugated shape. However, the lower core angle revealed minimal stress concentration with SL:86 mm and SL:98 mm, due to the large displacement of the lower core angle and the support position being comparatively far from the lower angle of the core.

It can be seen that all the cases revealed stress concentration on the core struts at Z3 (Figure 5.10). The concentration stress of the cases SL: 90 mm and SL: 94 mm exceeded the ultimate strength of the parent materials due to large displacement elastic buckling of the core struts. While with SL: 86 mm and SL: 98 mm the concentrated stress showed a minimal value and it was less than the ultimate strength of the woven E-glass fibre reinforced epoxy composite parent materials due to flexible deformation of the structure. However, with the MD support, as the axial displacement of the lower face sheet was restricted, the core struts showed midpoint buckling (second harmonic), i.e., they showed a tensile and compressive stress form.

In all the cases, the quasi-static compression load on the TCS structure caused core buckling, thus, it produced force moment in the upper angle. As a result, the composite core at Z4 experienced either tensile or compression stress concentration. This means that during all loading conditions on the TCS structure, the upper angle is the critical zone and the core will experience stress concentration. However, results revealed that at Z5 of the core there was no stress concentration. This was due to applying uniform distributed load on the upper sandwich skin.

It can be concluded that the TCS structure showed various forms of stress distribution based on the supporting situation of the lower face sheet of the structure.

In addition to the ultimate strength produced in the core struts, the core angles experienced a high stress concentration reaching failure stress of the composite parent materials. From the literature (Kazemahvazi and Zenkert, 2009, Kazemahvazi et al., 2009, Rejab and Cantwell, 2013, Xu et al., 2016, Schneider et al., 2015), the researchers found that the failure stress was concentrated in the struts of the trapezoidal composite corrugated core. This is because they performed simple liner analysing of the core struts. However, the FE analysis showed that the failure stress can be concentrated in both core struts and core angles (w_1 and w_2). Therefore, these core angles of the TCS structure needs to be strengthened and enhanced with high-performance materials or with optimization of the core geometry.

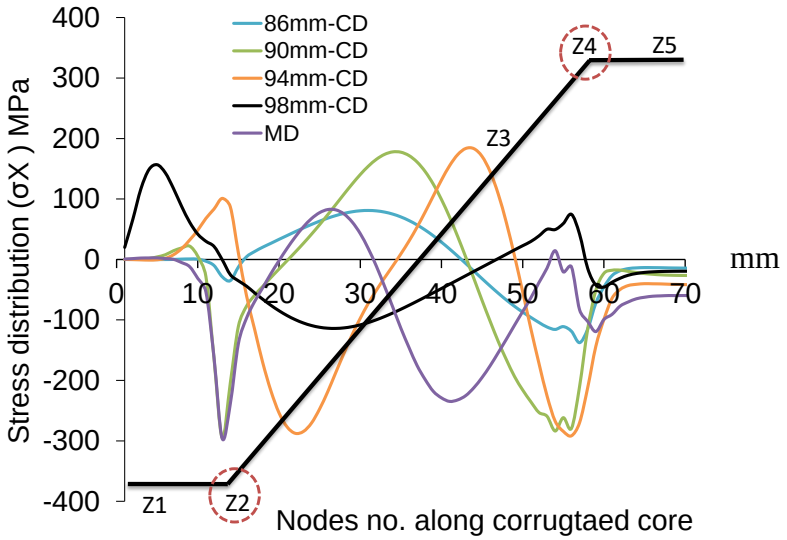

Figure 5.10: Stress distribution on the composite core of the GC1 TCS structure model when supported in the CD and MD directions along corrugated core

5.4 Numerical Core Optimization of the TCS Structure

Designers aim to improve structural strength by producing optimal designs. In a number of studies, single and multi-objective optimization were employed to design sandwich panels (Kalantari et al., 2010, Baroutaji et al., 2015, Hou et al., 2013). The latter approach has become the goal of recent research into designing TCS structures, because of this approach's capability to optimize two or more objectives simultaneously (Ashby, 2000, Omkar et al., 2009, Swanson and Kim, 2002).

The high strength-to-weight ratio of composite materials prompted engineers to use such materials in fabricating TCS structures. However, to date, there are no available standard specifications or design codes for TCS structures, such as for the

core's height, short span, or long span. This chapter set out to predict which composite corrugated core design is optimal by a multi-objective optimization method. For this, the design constraints are the applied load and the stress concentration in the composite core members, without increasing core thickness and changing core angle.

Due to the complexity of a trapezoidal corrugated core's geometry and the long procedures required via the traditional algorithm (Design sensitivity analysis, Genetic Algorithms, and Reliability-Based Design Optimisation) to optimize this, the numerical models offered through ANSYS Workbench were employed. The response surface optimization code of Workbench was used to optimize the design objectives: core height (P1), core short span (P4), and core long span (P5), as shown in Figure 5.11. P1 and P4 ranged between 10 mm and 60 mm and P5 ranged between 40 mm and 150 mm. Maximum stress (P6) on the composite core was selected as the design constraint.

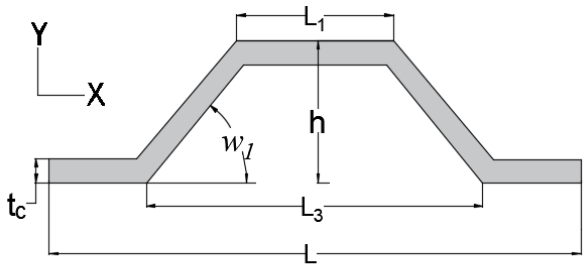

h	Core height (P1)
L_1	Core short span (P4)
L_3	Core long span (P5)
w_1	Constant core angle (45^0)
L	Unit cell length
t_c	Constant core thickness (2 mm)

Figure 5.11: Geometric parameters of the trapezoidal composite corrugated core

The maximum stress value was targeted at 210 MPa, which was obtained from the average values of the ultimate tensile and compression strength of the composite core's parent materials. The maximum axial displacement of the upper face sheet of the numerical model was fixed at 1 mm for all optimization iterations. This value was achieved from the experimental results that showed a roughly 1 mm axial displacement at the peak load response. The Hashin failure criteria were employed to identify the material allowable or the ultimate limit of the composite core material design constraints. The safety factor of the composite was 1 (Clarke, 2014), nominated from the materials' properties (see Section 4.4) using the characteristic strength of the fibre.

As the support in MD caused severe composite core damage, the core model was supported by fixed and rigid support to represent the MD support.

Figure 5.12 (a) shows the variation of maximum stress on the composite corrugated core with the core short span (P4) and core height (P1). It can be observed that the minimum critical value of maximum stress (210 MPa) was recorded for the composite core with 30 mm as the value of both P4 and P1. Figure 5.12 (b) shows the variation of maximum stress (210 MPa) on the composite corrugated core with the core long span (P5) and core height (P1). It can be seen that the minimum critical value of maximum stress (210 MPa) was recorded for the composite core that had a 30 mm value for P1 and a 90 mm value for P5. Utilizing proper core geometrical parameters can decrease stress concentrations without imposing any extra sandwich weight or costs.

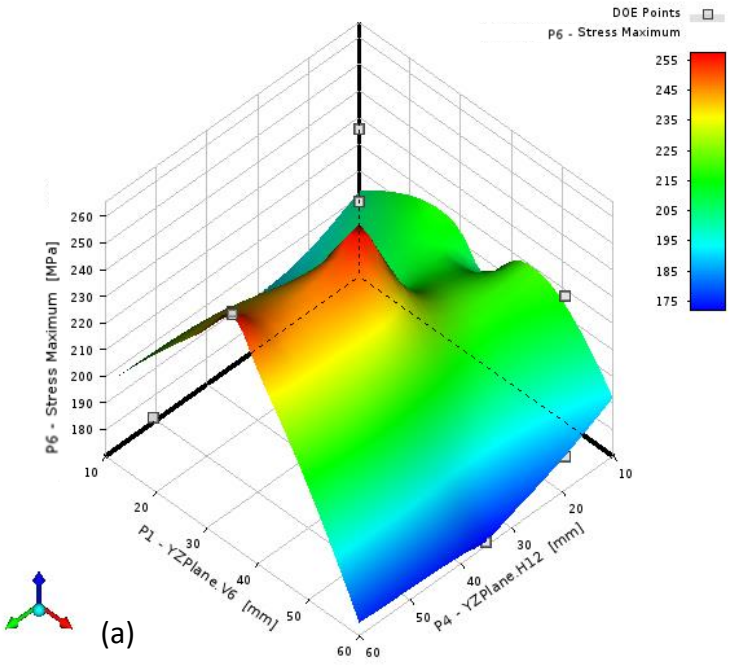

Figure 5.12: (a) 3D plot of variation of maximum stress on the composite corrugated core with the core height (P1) and core short span (P4)

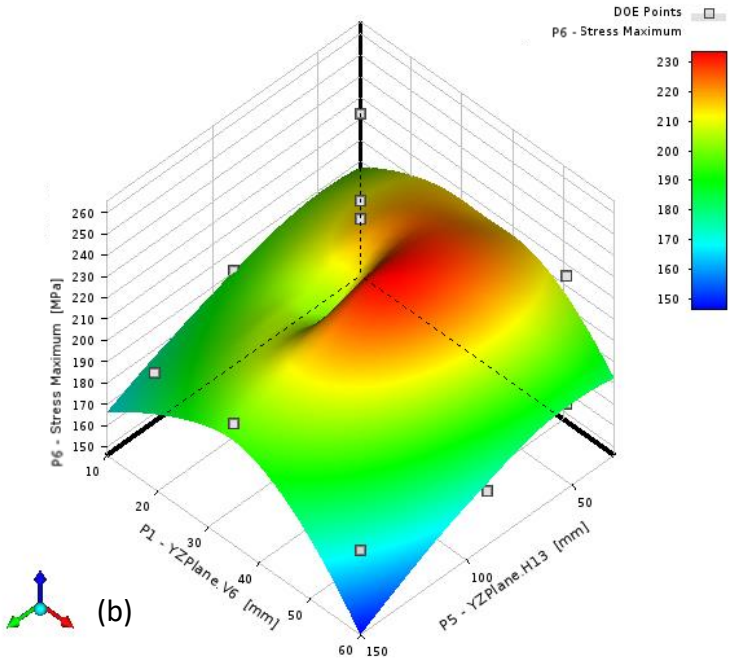

Figure 5.12: (b) 3D plot of variation of maximum stress on the composite corrugated core with the core height (P1) and core long span (P5)

From Figure 5.12: (a-b), a two dimensional (2D) figure was plotted to represent each objective of the optimal design related to the maximum stress constraint, as shown in Figure 5.13 (a). It also shows the majority of the design points for fabricating the trapezoidal composite cores ranged between 10 mm and 35 mm; the other points out of this range could not be taken due to the high value of the maximum stress (P6). However, although the stress concentration showed a minimal value with 10 mm of core height, it is not recommended as an appropriate point for design. This is because decreasing the P1 value leads to decreasing the elastic stiffness constant of the composite core in the transverse direction (Lok and Cheng, 2000).

Figure 5.13 (b) shows the design points of the core short span (P4) with the design constraint value (P6). The curve exhibited fluctuation with an increased length of the core short span. The appropriate design points ranged between 15 mm and 35 mm, and at roughly 30 mm the stress concentration on the core was the minimal value. The final design objective is the long span (P5) of the core, which was plotted against the maximum stress concentration (P6) on the composite core as shown in the Figure 5.13 (c). It can be seen that the design point ranged between 80 mm and 140 mm for P5. However, although the curve fluctuated when P6 increased, the minimal value of the stress concentration was obtained at 90 mm. It can be concluded from Figure 5.13 that

the optimal design point is 30 mm for each of P4 and P5, and 90 mm for P6, in which case they come roughly close to the value for the ultimate strength of the core parent material. The stress concentration value might be minimised by increasing some design parameters, such as core thickness, as discussed in Chapter 4. However, increasing the core thickness increases the sandwich weight/density (Chang, 2004), and does not meet optimal core design. The optimized core geometrical parameters were chosen for fabricating the composite corrugate sandwich core hybridized with high-performance fibre, as discussed in the next chapter.

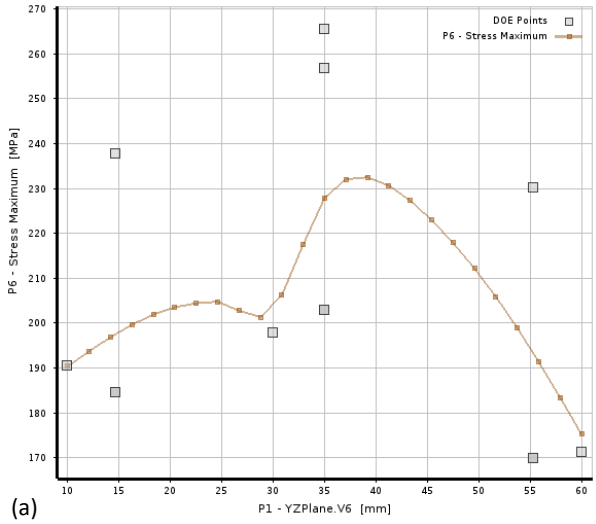

(a)

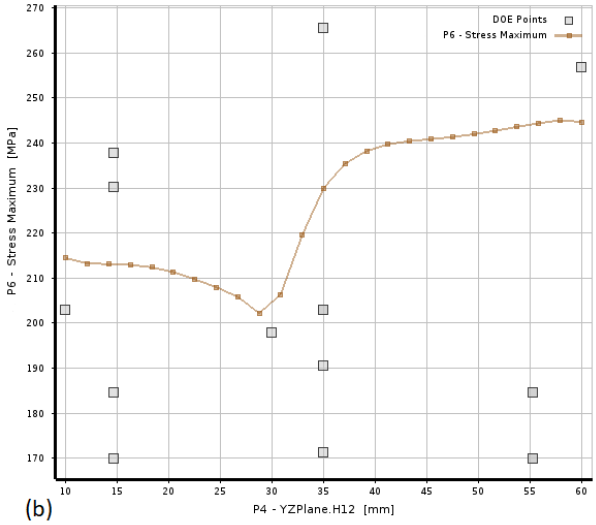

(b)

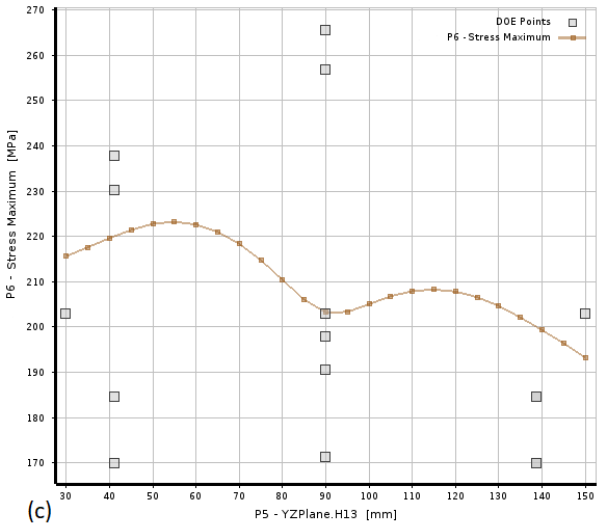

Figure 5.13: Core geometric design objective related to stress design constraint (a) Maximum stress vs. core height (b) Maximum stress vs. core short span, and (c) Maximum stress vs. core long span

5.5 Numerical Response of the TCS Structure under Low-Velocity Impact

5.5.1 Impact test at threshold kinetic energy

FE analysis was also performed on the TCS structures under low-velocity impact at the visible damage threshold energy of the composite parent materials. Similar boundary conditions to the experimental tests were applied, such as different impactor heads, impactor velocities, and edge supports of the sandwich. As well, the Hashin failure criteria was utilized in the TCS structure numerical modelling.

5.5.1.1 Impact force

Explicit dynamic FE analysis was performed to simulate the low-velocity impact of the GC7 TCS structure under low-velocity impact. Figure 5.14 (a-d) shows the comparison of experimental results and FE analysis prediction. The FE model results significantly correlated with the experimental results involving the impact behaviour of such a sandwich in the term of force slope, peak force and impact time. Moreover, the simulated results were also affected by the shape of the impactor head. This comparison demonstrated that the explicit dynamic FE model when employing the Hashin criteria accurately predicted the impact behaviour of the TCS structure under low-velocity impact.

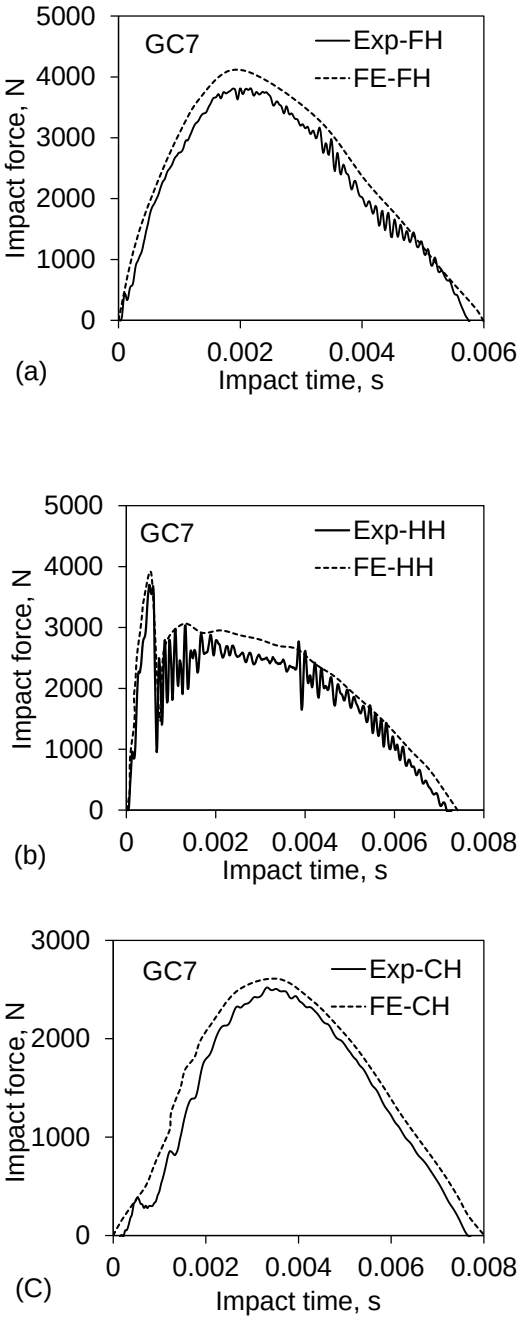

Figure 5.14: Experimental and numerical force-time response of the GC7 TCS structure at visible damage threshold energy, (a) FH, (b) HH, and (c) CH

5.5.1.2 Failure mode

Assessment of the impact models showed different patterns of damage prediction due to the three impactor heads, as shown in Figure 5.15. The damage traces of the numerical models correlated to the captured photos of the experimental tests (Section 4.5). It was decided to compare the matrix compressive failure criterion in the FE model with the experimental outcome. The matrix compressive failure criterion value

ranged between 0 and 1. The value of 0 means no failure, while 1 and above indicate full damage of the matrix (Ansys_help, 2019).

With the FE modelling of the flat head, circular damage is spotted on the impacted area, which refers to matrix damage. This is identical to the impactor head profile as seen in Figures 5.14 a) and d). The damage trace of the hemispherical head showed a larger circular damage area due to the large local bending of contact area under the impact load (Figure 5.15 (b and e)). The conical impactor head caused smaller local damage of the impact area and a semi-penetration (Figure 5.15 (c and f)). Moreover, damage trace (decrepitate) was seen on the rear surface of the impacted area. The damage traces of the hemispherical and conical heads were less than for the impactor profile (i.e., cross-section) by approximately 10% and 30%, respectively. It can be concluded that the built FE model provided strong numerical confirmation about the damage modes of the trapezoidal composite corrugated core sandwich under low-velocity impact.

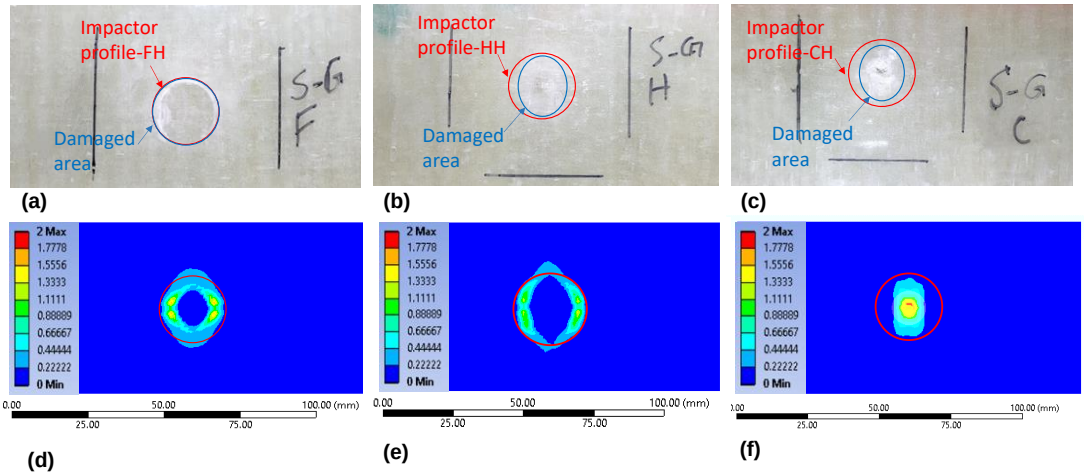

Figure 5.15: Damage trace of experimental results and numerical model of upper face sheet of the TCS structure under low-velocity impact: (a and d) FH, (b and e) HH, and (c and f) CH

5.5.1.3 Energy absorption

During an impact event, the TCS structure undergoes complex and elastic deformation combined with impact damage. Figure 5.16 shows the experimental and numerical energy absorption of the GC7 TCS structure impacted with flat, hemispherical, and conical impactor heads at the visible damage threshold energy. The structural energy absorption was at its maximum for the impact events with the flat and hemispherical

heads. This is attributed to elastic buckling of the core struts' deformation and upper face sheet bending, which significantly improved the structural energy absorption (see Appendix C, Eq.7). These findings enhance our understanding of how the largest amount of the impact energy dissipated in structural elastic deformation of the composite core struts. In contrast, in the case of the conical head, most of the kinetic energy was absorbed in the local damage of the impacted area, as explained in Section 4.6.

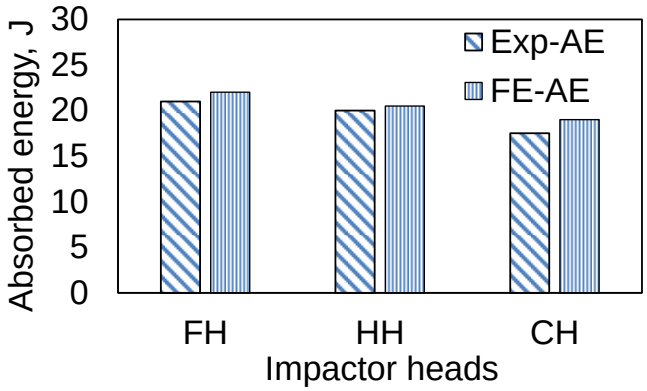

Figure 5.16: Experimental and numerical energy absorption capacity of the GC7 TCS structure relative to FH, HH, and CH at the threshold kinetic energy

5.5.2 Impact test beyond the threshold kinetic energy

5.5.2.1 The effect of different impactor weight

The numerical model was developed to perform low-velocity impact on the GC11 TCS structure beyond the visible damage threshold energy of composite parent materials of 54 J. At constant kinetic energy 54 J, the damage area of the upper face sheet as a function of the impactor weight of the numerical model was correlated with the experimental tests. These experimental tests have been previously explained in Section 4.7. The impact traces were captured by a Sony-RX100 camera and processed by Gwydion 2.5 commercial software. Figure 5.17 illustrates the impact event, actual 3D damaged area, and FEA damaged area of the GC11 TCS structure impacted by three different impactor weights. From Figure 5.17 (d-f), it is clear that a decrease of impactor weight from 15.7 kg to 8.6 kg and to 5.4 kg leads to a significantly decreased damaged area, 552 mm^2 to 249 mm^2 and to 175 mm^2, respectively. This is attributed to decrease of impactor momentum. Moreover, a visible damage trace was seen with the larger impactor weight; and barely visible impact damage was seen with the

medium impactor weight. In contrast, the smaller impactor weight could not create any visible damage on the TCS structure. Figure 5.17 shows that the FE model significantly predicted the damage area of the TCS structure, relative to impactor weight. Moreover, it demonstrates how the damaged area spread widely on the upper face sheet of the composite core.

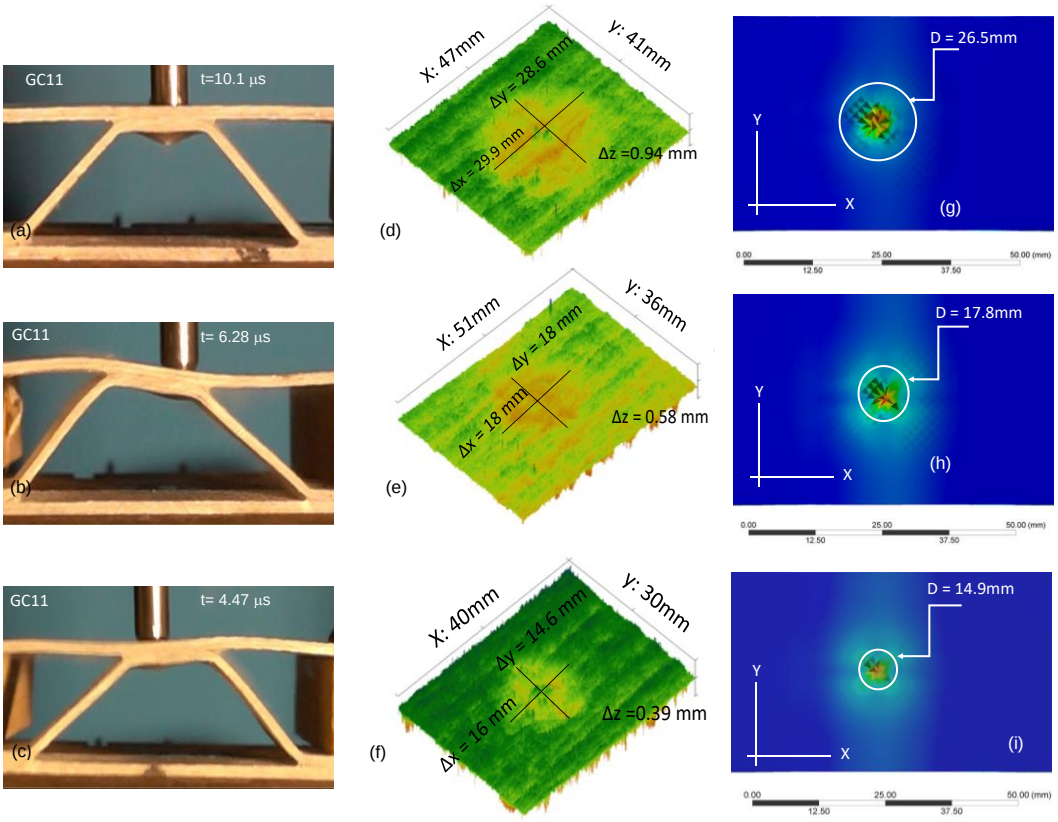

Figure 5.17: Impact event, actual 3D damaged area, and FEA damaged area of GC11 TCS structure impacted by a large, medium, and small weight: (a-c) impact event, (d-f) damage trace of experiment, and (g-h) damage trace of modelling

Then the FE model was developed for corrugated core thicknesses of 3 mm and 2 mm, and the impact energies were kept at 40 J and 27 J, respectively. Kinetic energy was also above the visible damage threshold energy of the composite parent materials. Figure 5.18 shows that the impactor weight has a non-linear influence on the damage area. It can be concluded that, at low-velocity impact, a large impactor weight can cause a large scale of damage in comparison to a small impactor weight at the same magnitude of kinetic energy. Moreover, a visible damage trace was seen with the

former impactor weight; in contrast, the medium and small impactor weight could not create any visible damage on the composite corrugated core sandwich.

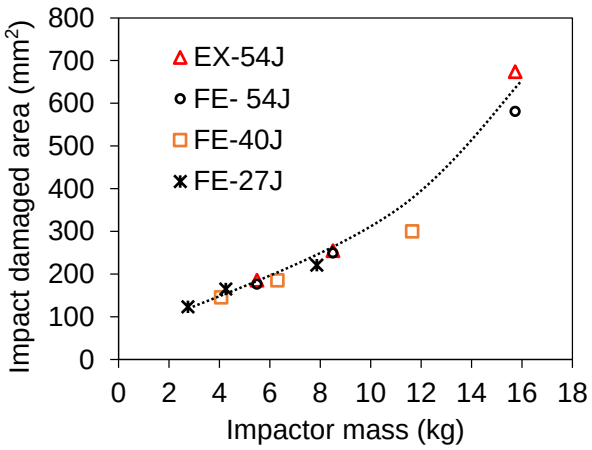

Figure 5.18: Damage area of TCS structures vs. the impactor weight at the same level of impact energy

5.6 Summary

In this chapter, FE modelling of TCS structure by ANSYS code was developed (See Appendix D). The numerical predictions were correlated with the experimental results to verify the accuracy of these FE models. The developed model was employed to analyze the stress concentration on the composite corrugated core members. The FE analysis showed that the failure stress could be concentrated in both core struts and core angles (w_1 and w_2). Through the FE analysis, an optimal design was found for the TCS structure with a given sandwich weight.

Numerical analysis was also employed to investigate the impact behaviours of the TCS structure under low-velocity impact, and this was confirmed by experimental results. The FE model whose numerical results are in good agreement with those achieved by experiment was also used to study the effect of the impactor weight on the damage area of the TCS structure under low-velocity impact. This numerical analysis contributed to developing the model for investigating the TCS structure's mechanical properties with specific loading conditions, such as vibration and fatigue, a project in future work.

Chapter 6

Case study of the TCS structure under low-velocity impact

6.1 Introduction

This chapter comprises two different case studies. The first aims to test a multi-cell TCS structure under low-velocity and higher impact energy. This is to demonstrate the application of fundamental knowledge developed on single-cell structures to multi-core structures. In addition, in this case study, the effect has been studied of the core height-to-pitch ratio (i.e., core relative density), as shown in Figure 6.1, on the impact behaviour of a full-scale multi-cell TCS structure. The second case study aims to demonstrate the superior performance of a multi-cell TCS structure in specific stiffness/strength, energy absorption, and damage resistance under low-velocity impact without increasing the structural weight/thickness ratio. Therefore, for this case, a novel TCS structure has been fabricated and tested. Multi-cell TCS structures were hybridized using kevlar and zylon high-performance fibres to improve the impact performance. These multi-cell TCS structures were fabricated with four layers of glass fibre with one layer replaced either by kevlar or zylon fibre to create hybrid multi-cell TCS structures i.e., with 25% high-performance fibre and 75% traditional fibre. Three different energy levels of low-velocity impact tests were performed to achieve the goals. The impact behaviour, damage mode, specific absorbed energy, and residual strength after the impact of the multi-cell TCS structure were re-investigated using a low-velocity impact test with 30 J, 40 J and 50 J kinetic energy levels, which are above the threshold limit. The details of these two case studies demonstrate how to design high-performance and lightweight TCS structures.

6.2 Case Study One: Full-scale Multi-Cell TCS Structures under Low-Velocity Impact

Three full-scale TCS structures, GC13, GC14, and GC15, were fabricated, as shown in Figure 6.1 and tested under low-velocity impact at a high level of impact energy of 150 J. The geometrical dimensions of the tested TCS structures are summarized in Table 6.1. In this case, the TCS structures were simply supported in the machine direction (MD) to observe the maximum impact damage. The drop weight impactor height was increased to 5 m (impact velocity = 10 m/s), the impactor weight was 3 kg, and a 12 mm hemispherical impactor head was used. According to the kinetic energy equation (K.E= ½*m*v^2), the impactor head has the kinetic energy of 150 J at the impact. The new experimental setup involved a 5 m tube to guide the impactor head with 2*20 m connection wires to connect the force transducer. A piezoelectric (PCB-200B04) load cell to measure the instance impact force and an accelerometer (PCB-5014B) with data logger was used to measure the acceleration of the impactor head. The force-time, acceleration and displacement of the impactor (by double integration of the acceleration) were obtained by SIEMENS - LMS SCADAS frame system.

Table 6.2 shows the details of the experimental setup of this group of the multi-cell TCS structures.

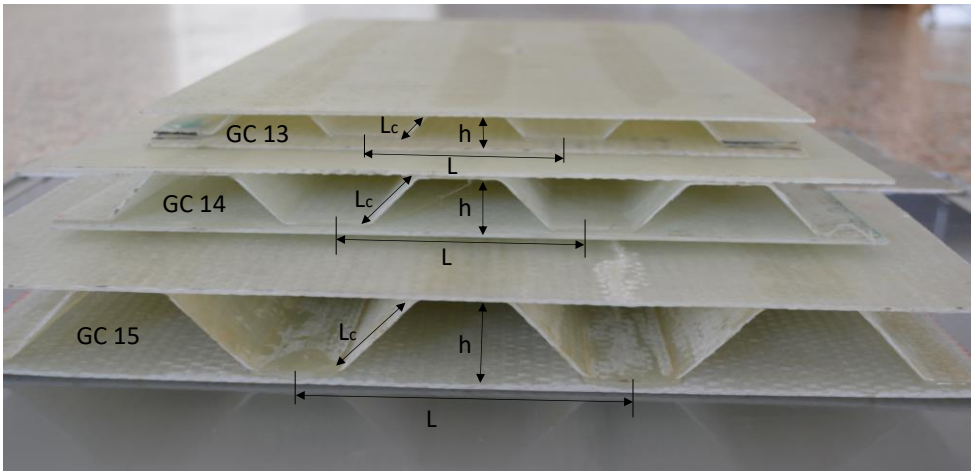

Figure 6.1: Full scale of three different designs of the multi-cell TCS structures GC13, GC14, and GC15

Table 6.1: The geometric parameters and variation of the large scale TCS structures subjected to low-velocity impact at high level of kinetic energy

Specimen ID	Qty	t_c	h	t_u & t_l	L_c	L	Sandwich density	Core height/ pitch (h/L)
		mm	mm	mm	mm	mm	g/mm^3	mm/mm
GC13	1	1.9	12	2	14.2	80	0.057	0.15
GC14	1	1.9	22	2	28.3	100	0.036	0.22
GC15	1	1.9	32	2	42.5	118	0.025	0.27

Table 6.2: Drop weight test setup of the GC14, GC15, and GC16 TCS structure configurations

Impact setup	Impactor head	Impactor mass (kg)	Impactor velocity (m/s)	Kinetic energy (J)
i	HH	3.06	10	150

6.2.1 Impact behaviour of full-scale TCS structure

Figure 6.2 shows the force-time of the impacted full-scale multi-cell TCS structures. It can be seen that an increase in the core height-to-pitch ratio of the TCS structures (i.e., decreasing the sandwich density) decreased the peak force; however, the impact time increased. The impact force of GC13 decreased by 16% and 36%. However, the impact time was increased by 45% and 75% with the increase of core height-to-pitch of the GC14 and GC15 TCS structures, respectively. At a low core height-to-core pitch ratio, the TCS structure acts as a monolithic plate.

The damage modes of the TCS structures were different from the core height-to-pitch ratios. In the case of TCS structure GC13, the upper face sheet, corrugated core, and lower face sheet were penetrated. For GC14, both the upper face sheet and corrugated core were penetrated, and the lower face showed larger de-bonding with the lower members of the core. This is attributed to the increasing flexural bending of the core struts, which resulted from an increase of core height-to-pitch. Similarly, for

GC15, due to the high flexural bending of the core struts, the TCS structure was not penetrated. However, GC15 exhibited wrinkling damage of the upper face sheet; this is attributed to the high flexural bending of the composite corrugated core. Table 6.3 shows the failure modes of the impacted full-scale multi-cell TCS structures under low-velocity impact at a high level of kinetic energy.

Figure 6.3 shows the energy absorption of the full-scale multi-cell TCS structure of GC13, GC14, and GC15. When the peak force of the impact events decreased, the energy absorption ability of the TCS structures increased. This is due to the increase in the sandwich deformation and impact time (due to a higher core height-to-pitch ratio). It can be concluded that at a low ratio of core height-to-core pitch, the TCS structure acts as a monolithic plate, showing maximum force impact, minimum impact time, catastrophic damage of the impacted area, and minimum energy absorption. Increasing the core height-to-pitch ratio leads to an increase in the TCS structure's energy absorption.

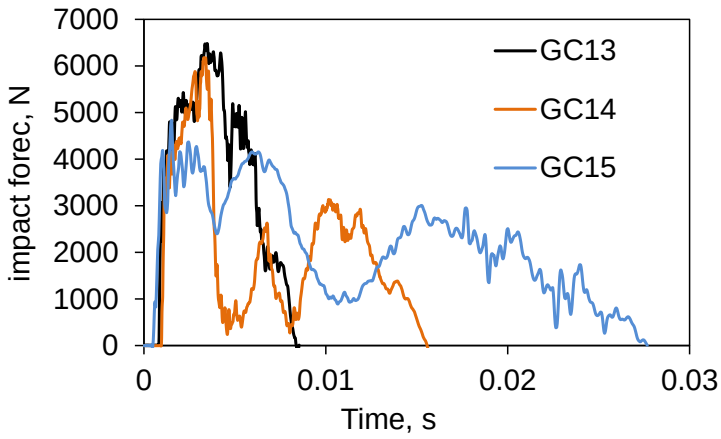

Figure 6.2: Force-time response of the impacted full-scale multi-cell TCS structures GC13, GC14, and GC15

Table 6.3 The damage modes of the full-scale multi-cell TCS structures

Failure mode	Specimen		
	GC13	GC14	GC15
Upper face penetration	x	x	-
Core face penetration	x	x	-
Lower face penetration	x	-	-
Lower face bulge and de-bonding	-	x	-
Impact trace	-	-	x
Wrinkling of upper face	-	-	x

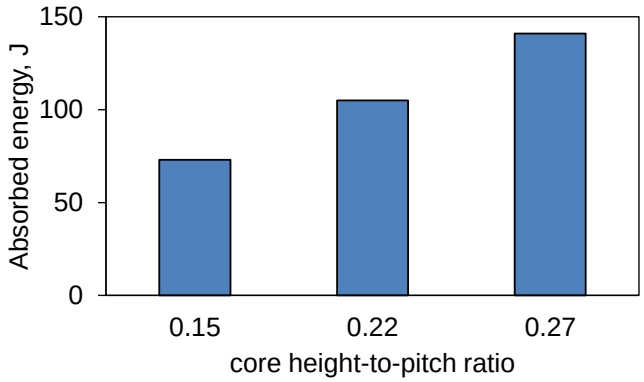

Figure 6.3: Absorbed energy of the TCS structures relative to core height-to-pitch ratio

6.3 Case Study Two: Hybrid Multi-Cell TCS Structure under Low-Velocity Impact

In this case study, low-velocity impact tests on multi-cell TCS structure (GG) and hybrid TCS structures (GK) and (GZ), were conducted. Figure 6.4(a) shows the schematic design of the three TCS structures GG (glass-glass), GK (glass-kevlar), and GZ (glass-zylon) which were fabricated in this research. Firstly, three different multi-cell corrugated core types were made; in the first core configuration, just woven E-glass fibre was used and reinforced with the epoxy matrix Kinetix R246TX. In the second corrugated core configuration, three layers of woven E-glass fibre and one layer of kevlar fibre was used to fabricate a hybrid glass-kevlar core i.e., 75% glass fibre and 25% kevlar fibre. The same procedure was used in the fabrication of the third corrugated core, three plies of woven E-glass fibre were stacked with one layer of zylon fibre to fabricate a hybrid glass-zylon corrugated core, i.e., 75% glass fibre and 25% zylon fibre.

Figure 6.4(b) shows the ply stacking of the hybrid core laminates. The fibre layers were ordered as one layer of the glass followed by a layer of kevlar and two layers of E-glass (GKGG) to ensure the bonds of the kevlar ply with the E-glass plies. The same order of laminae configuration was also utilized to arrange the hybrid E-glass-zylon corrugated configuration (GZGG). Note that the ply of the woven fibre layers started from the top to the bottom of the corrugated core. The mechanical properties of the fibre plies are summarized in Table 6.4. Then, four plies of woven E-glass fibre were stacked and the epoxy matrix was reinforced with Kinetix R246TX to fabricate the upper and lower skins of the sandwich. The geometrical parameters and weights of the TCS structures are summarized in Table 6.6.

In this experimental study, the impact standard (ASTM-D7136, 2012) was followed for the low-velocity impact testing. The threshold damage kinetic energy of the composite parent materials was decided using $E = t * C_E$, where, *t* is the specimen thickness (i.e. thickness of upper face sheet plus the thickness of core), *E* is the potential energy of impactor head prior to dropping , and C_E is the specific ratio of impact energy to specimen thickness (6.7 J/mm) (Li et al., 2017).The hemispherical head ϕ =12mm was connected to three different impactor masses (m) at constant impact velocity ($v = \sqrt{2gh}$) to obtain three different kinetic energies $K.E = \frac{1}{2}mv^2$, where *g* is the gravitational acceleration, and *h* and *m* are the height and impactor

weight, respectively. The selected magnitude 30 J of kinetic energy was above the visible damage threshold energy by 30%. This was to ensure that the impact caused damage to the specimen. Then the kinetic energy was linearly increased to 40 J and 50 J for subsequent impact testings. Table 6.4 shows the impactor weight, initial impact velocity and kinetic energy of the conducted tests.

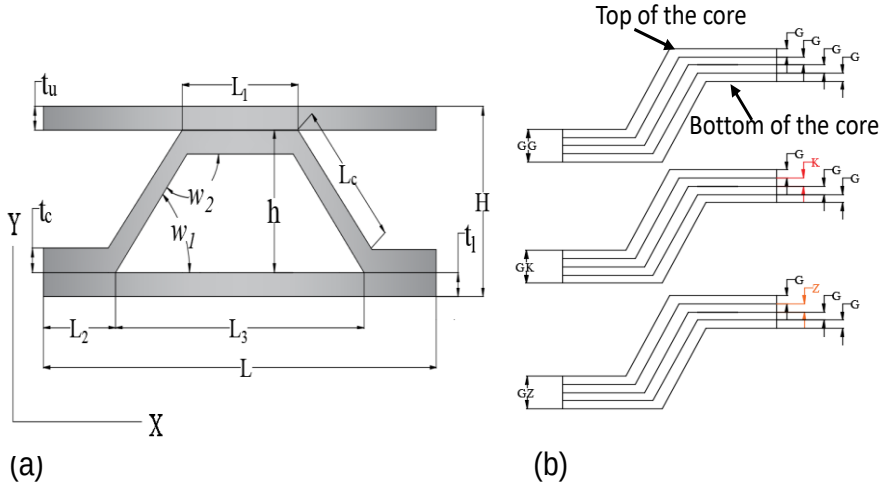

Figure 6.4: (a) Schematic diagram of TCS structure, and (b) Ply order of the corrugated core for TCS structure GG, GK, and GZ

Table 6.4: Mechanical properties of the woven E-glass, kevlar, and zylon ply

Properties	Unit	Glass	Kevlar	Zylon	Reference
Density	g/cm^3	2.54	1.45	1.56	(Colan-Australia, 2017, Toyobo, 2005, Gurit, 2018)
Tensile strength	GPa	3.4	3.6	5.8	(Colan-Australia, 2017, Toyobo, 2005, Gurit, 2018)
Tensile modulus	GPa	72	109	270	(Colan-Australia, 2017, Toyobo, 2005, Gurit, 2018)
Elongation at break	%	4.8	2.4	2.5	(Colan-Australia, 2017, Toyobo, 2005, Gurit, 2018)

Table 6.5: The geometrical parameters of the composite corrugated core sandwich fabricated with high-performance synthetic fibre

Specimens ID	Qty	t_c	h	L_1	t_u & t_l	H	W
		mm	*mm*	mm	mm	mm	Kg/m^3
GG	3	1.5	30	30	1.82	33.4	259
GK	3	1.45	30	30	1.8	35.7	243
GZ	3	1.55	30	30	1.85	38.7	250

Table 6.6: Low-velocity impact test process of the TCS structures GG, GK, and GZ configurations

Setup	Impactor head	Impactor weight (kg)	Impactor velocity (m/s)	Kinetic energy (J)
i	HH	3	4.47	30
ii	HH	4	4.47	40
iii	HH	5	4.47	50

6.3.1 Four-point bending of the TCS structure after impact

After the low-velocity impact testing was carried out on GG, GK, and GZ, four-point bending tests, as shown in Figure 6.5, were performed on the impacted TCS structure according to (ASTM-D5467/D5467M, 2017) standard. However, four-point bending tests were also conducted on non-impacted (NI) samples for comparison. The tests were conducted by using an MTS 10 kN testing machine at a displacement rate of 0.5 mm/min. A Quantum XMX1615B - strain gauges bridge amplifier was used for strain measurements. Strain gauges of the type FLA-5-11 were glued to the upper face sheet of the TCS structure beside the impacted area and parallel to the corrugated core direction (i.e., MD).

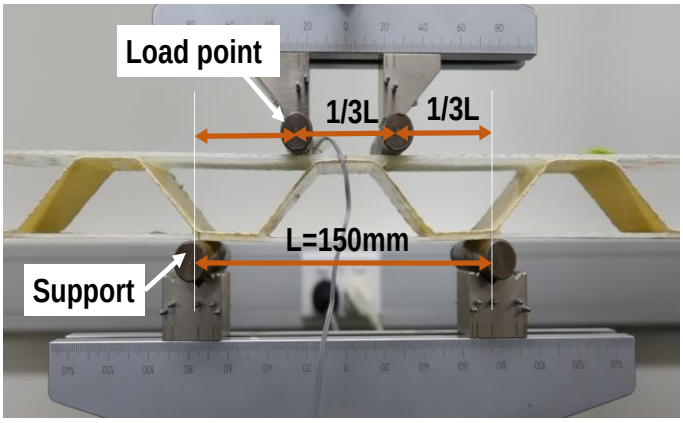

Figure 6.5: The four-point bending test on the TCS structure

6.3.2 The effect of ply combination on impact response

Figure 6.6 (a) shows the impact response of the TCS structures GG, GK, and GZ subjected to 30 J of kinetic energy. The peak value and the corresponding impact time showed identical magnitudes for all three specimens. The force curve trace showed a sharp linear increase with an increase in the impact time until the peak load. Before reaching the peak value, the force-time trace showed a tiny drop between 1000 and 1500 N; this is attributed to a thin core thickness, which may have caused the elastic core struts' buckling. With the increase of impact time, the kinetic energy was mitigated and the impact force response gradually reduced due to the deformation of the sandwich and elastic buckling of the core (Figure 6.6 (b-d)). Between 0.004 s and 0.006 s, the impact force exhibited an oscillation due to the degradation of the materials' stiffness at the upper face sheet, leading to local damage under the impactor nose. It can therefore be seen that the high-performance fabric has no potential effect on the impact behaviour of the TCS structure at a low level of impact energy.

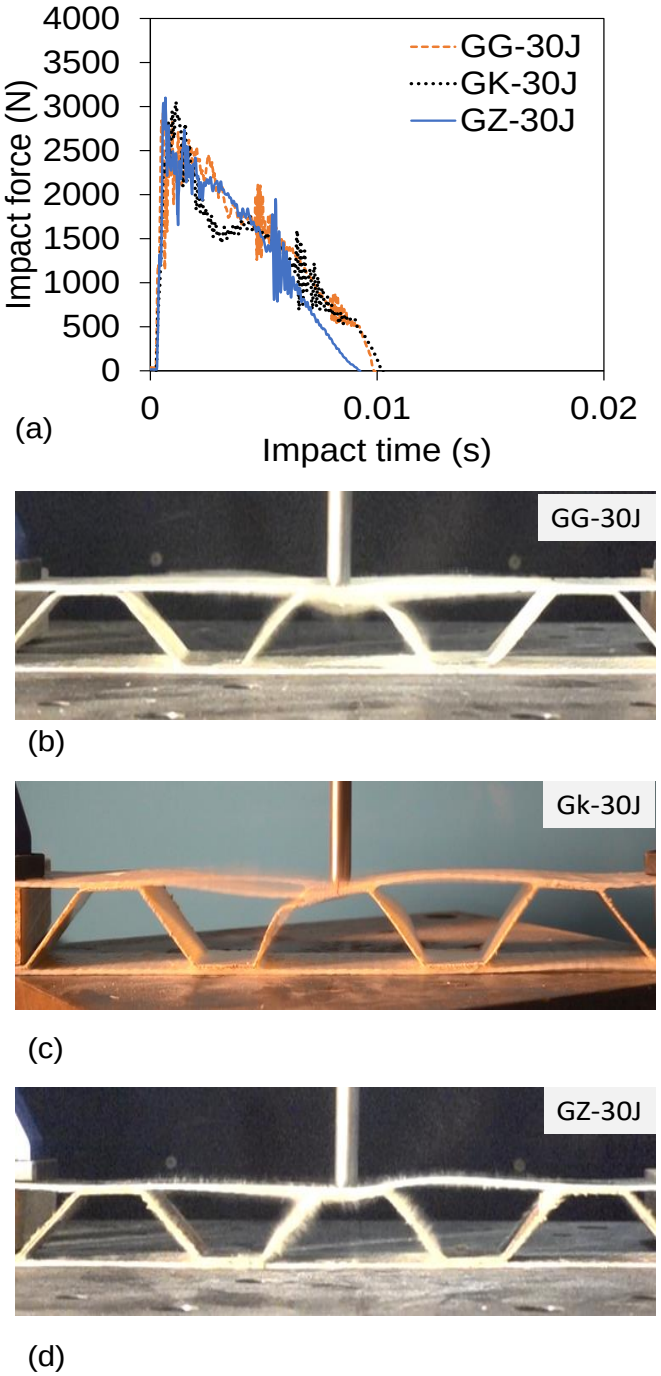

Figure 6.6: TCS structures GG, GK, and GZ subjected to 30 J (a) Impact force-time response, and (b-d) Captured image at the end of the impact

Figure 6.7(a) illustrates the force versus time response of the TCS structure impacted by 40 J kinetic energy. It can be seen that the sandwiches exhibited different responses at this kinetic energy level. For TCS structure GG, the first stage ended at 0.008 s, which reflects the TCS structure's resistance until the core fracture, and then the force increased again to about 500N. For TCS structure GK, the response after the

peak force showed a plateau for a longer time compared to TCS structure GG. This is due to the large elastic core buckling followed by local core damage (Figure 6.7c). However, TCS structure GZ exhibited a better response due to the core enhancement by high-performance fibre ply. Moreover, TCS structure GZ exhibited an increase in the impact of resistance with no core damage (Figure 6.7d).

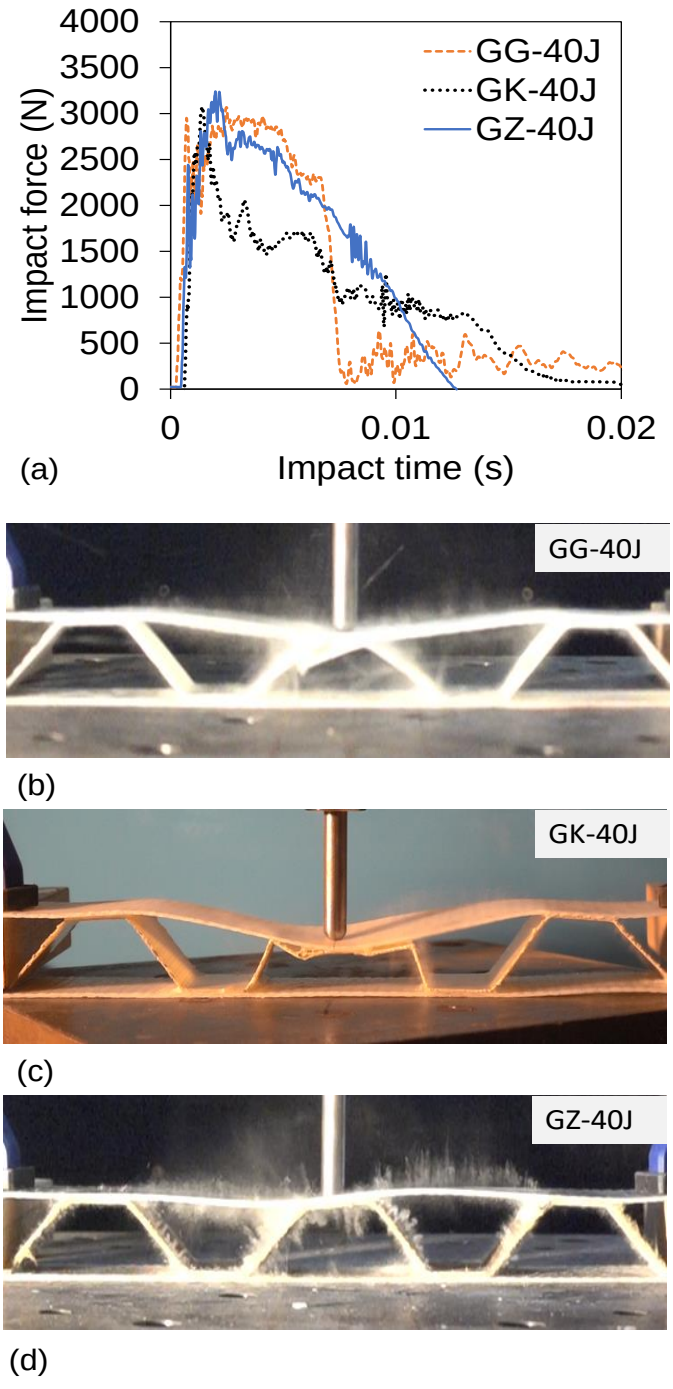

Figure 6.7: TCS structures GG, GK and GZ subjected to 40 J (a) Impact force-time response, and (b-d) Captured image at the end of the impact

Figure 6.8a shows the impact response of the fabricated TCS structures under 50 J of kinetic energy. The TCS structures GG and GK exhibited comparable force-time responses at 50 J. Figure 6.8 (b and c) show that TCS structures GG and GK absorbed the impact force by the corrugation angle fracture and core buckling damage, respectively. The peak force of TCS structure GZ also linearly increased, then the force dropped due to elastic core buckling and upper face deformation (Figure 6.8d). Moreover, the force response showed the repeated fluctuation of the force due to the local external damage of the upper face sheet plies. Furthermore, the dust plumes on the sandwich members indicated the contribution of the adjacent core in resisting impact force.

In general, one layer of kevlar ply can improve TCS structure resistance up to 3% (from 2968 N to 3055 N) at 30 J, 5% (from 2909 kN to 3056 kN) at 40 J and 7% (from 3015 kN to 3220 kN) at 50 J. On the other hand, one layer of zylon ply can improve sandwich resistance up to 5% (from 2968 kN to 3101 kN) at 30 J, 12% (from 2909 kN to 3242 kN) at 40 J and 25% (from 3015 kN to 3759 kN) at 50 J. Therefore, it can be concluded that the high-performance zylon fibre has only a minimal influence up to the impact energy of the visible damage threshold, but it can improve the impact resistance of the TCS structure in high impact energy incidents. The impact resistance of zylon fibre reinforced cores was shown to be superior impact compared to glass and kevlar in high energy impact situations.

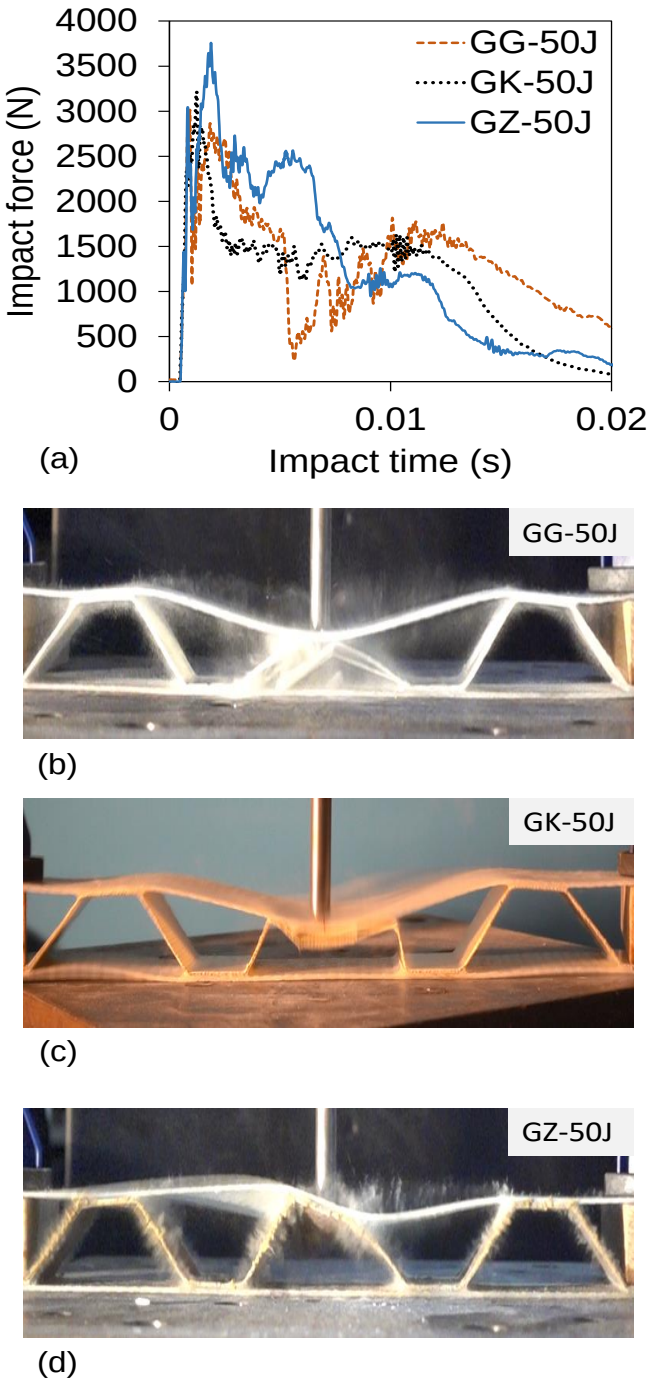

Figure 6.8: TCS structures GG, GK, and GZ subjected to 50 J (a) Impact force-time response, and (b-d) Captured image at the end of the impact

6.3.3 The effect of ply combination on failure modes

An in-depth understanding of the failure mode of TCS structures is one of the important aspects required for designing any engineering structures. Therefore, it is necessary to inspect TCS structures after an impact event. A non-destructive examination was performed with the naked eye to understand the failure mode.

Various types of damage and failure modes were revealed, such as white trace and upper face indent due to stress concentration at the impacted area. The de-bonding of the top face sheet and the upper flat core member also emerged as a major failure mode. Moreover, the core shear failure or core struts damage appeared due to global buckling. In some cases, combined damage modes were observed.

Table 6.7 summarizes the damage and fracture modes of the different TCS structures under low-velocity impact. Table 6.7 also indicated that all TCS structure types exhibited a white circular damage trace on the upper face sheet due to matrix damage at 30 J kinetic energy. However, other members of the TCS structure have shown no noticeable damage traces.

The TCS structures GG, GK, and GZ showed de-bonding of the upper face with a flat core member at an increased impact energy of 40 J and 50 J. Moreover, the GG structure depicted severe core shear failure (severe internal core fractures) at the upper angle for both these impact energies. This is due to exceeding the limit of the core's threshold shear stress, and inertial stabilization of the core struts. On the other hand, the GK structure exhibited global core buckling associated with the core strut damage at the middle section of the web for the same level of impact energy. Although an external damage trace was clearly observed on the top face sheet of the hybrid TCS structure GZ, discernible damage was not found to internal core members.

Interestingly, this observation indicates that one layer of zylon ply enhanced impact resistance by preventing core crushing. Moreover, the TCS structure GZ converted most of the impact energy to large deformation to maintain structural integrity. The TCS structure GZ showed significant superiority compared to a hybrid carbon aluminium corrugated core sandwich (He et al., 2016) by preventing the penetration effect under low-velocity impact at 50J kinetic energy. In summary, the rupture of the upper corrugation angle was the acute failure mode of TCS structure GG, which was eliminated by kevlar and zylon ply. Moreover, for TCS structure GZ, most of the damage was prevented by absorbing impact energy compared to GG and GK. The failure of GZ was external, as evident from the damage on the upper face sheet while GG showed severe internal damage that was difficult to detect by visual inspection.

Table 6.7: Damage and fracture modes of the TCS structure under different impact kinetic energy

Specimen ID	White trace	De-bonding failure	Core rupture upper angle	Core buckling fracture	Upper skin indent
GG-30J	x	o	o	o	o
GK-30J	x	o	o	o	o
GZ-30J	x	o	o	o	o
GG-40J	x	x	⁂	o	o
GK-40J	x	x	o	x	o
GZ-40J	x	x	o	o	x
GG-50J	x	x	⁂	o	o
GK-50J	x	x	o	x	o
GZ-50J	x	x	o	o	x

Note: (o) refers to no damage, (x) refers to damage, and (⁂) refers to a severe fracture.

6.3.4 The effect of impact energy on damage area

To further examine the properties of employing the high-performance fibre in fabricating the TCS structure subjected to low-velocity impact, it is important to qualitatively investigate the external damage area (i.e. indentation damage of the upper skin) and the kinetic energy of the impact. Figure 6.9 shows that an increase of the kinetic energy increases the impact trace for all TCS structures; however, the slope of the GZ core is steeper than the other two configurations. This indicates the GZ core distributed the impact force in a wider area than GK and GG did at the same level of kinetic energy.

This can be further examined in Figure 6.10, which shows that the TCS structures GG, GK, and GZ roughly exhibited similar magnitudes of the impact area, ranging from 12 to 17 mm^2 at the low kinetic energy of 30 J. At 40 J and 50 J, the impacted area of GG showed minimal magnitude when compared with GK and GZ. This was due to early severe damage to the upper corrugation angle. The core buckling and the delayed core struts damage slowly increased the indentation area on the GK sandwich at 40 J and 50 J (Figure 6.10). However, the high resistance of the zylon fibre ply led to preventing internal core damage; thus, it transferred all impact energy (40 J and 50 J) into a wider area that increased local contact damage or minimized stress

concentration of the upper skin sheet (Figure 6.10). Thus, using the high-stiffness synthetic fibre leads to a decrease in the common internal core crushing, enhancing the TCS structure impact behaviour, and distributing the resulting stresses on the upper face sheet to external damage. The advantage here is that the upper face sheet can be repaired easily after any impact situation.

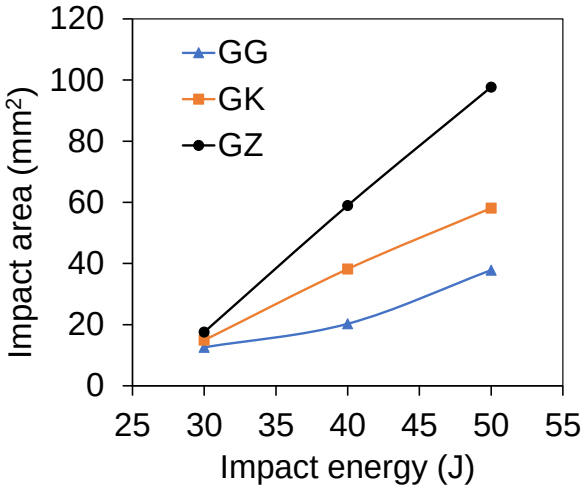

Figure 6.9: Impacted area of the upper face sheet of TCS structures GG, GK and GZ concerning the kinetic energy

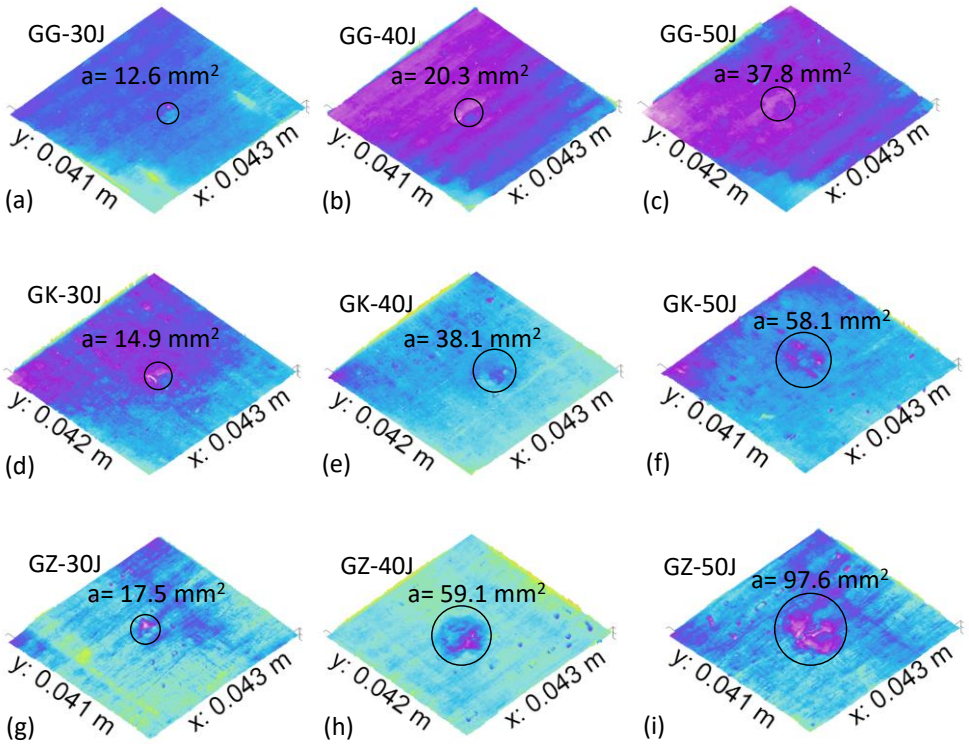

Figure 6.10: Impact trace of TCS structures GG, GK, and GZ under different impact energy analysed by Gwyddion code

6.3.5 The effect of ply combination on specific energy absorption

Since TCS structure cores are exposed to impact events during their service life, understanding the specific energy absorption (SEA) capacity is an important aspect of their design. SEA is often employed to compare the behaviour and weight benefits in a lightweight design. Normalising the total absorbed energy by the sandwich weight leads to obtaining the specific absorbed energy ($SEA = AE/w$) in J/g, where AE represents absorbed energy (i.e., the total area under the force-displacement curve) and w is the sandwich weight.

Figure 6.11 shows a comparison of the specific absorbed energy of the TCS structures GG, GK and GZ under different kinetic energies. GG exhibited roughly similar SEA with the increase of impact energy from 30 J to 40 J and 50 J. However, the TCS structures containing high-performance fibre ply showed a significant increase of SEA with the increase of impact energy. The increasing magnitude of SEA for GZ indicates that it is more effective for designing TCS structures to withstand at high impact energy. Furthermore, Table 6.8 compares the SEA from the current study with other types of core structures under low-velocity impact, from the literature. From the table, it is found that GK and GZ can offer better specific energy than the other traditional core materials such as expanded polypropylene, aluminium, rubber and plastic. Employing high-performance synthetic fibres in TCS structures can provide high specific energy while maintaining a lower weight.

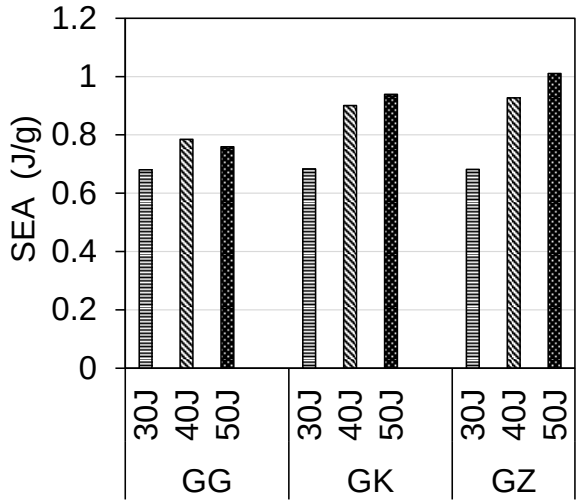

Figure 6.11: Comparison of specific energy absorption for different TCS structures

Table 6.8: Comparison of specific energy absorption among different materials

Sandwich types	Reference	Peak force (kN)	SEA (J/g)
GG core TCS structure	Current study	3.1	0.76
GK core TCS structure	Current study	3.3	0.93
GZ core TCS structure	Current study	3.8	1.01
Expanded polypropylene foam (EPP-F) core sandwich	(Zhang et al., 2017)	2.3	0.8
Aluminium honeycomb (Al-H) core sandwich	(Zhang et al., 2017)	2.4	0.8
Rubber ball (R-B) core sandwich	(Zhang et al., 2017)	5.8	0.2
Plastic ball (P- B) core sandwich	(Zhang et al., 2017)	2.8	0.6

6.3.6 The effect of ply combination on residual load carrying capacity

The four-point bending tests were conducted to measure the residual static load carrying capacity of the specimen after the impact test. The specified test setup transmitted loads into the core from the upper face sheet. These tests were carried out both for non-impacted (NI) and impacted TCS structures according to (ASTM-D5467/D5467M, 2017) standard. The tests were stopped after hearing the first crushing sound of the TCS structures.

Figure 6.12(a-c) shows the force-displacement response of GG, GK, and GZ after impact. All the impacted TCS structures at 30 J exhibited a very similar load-displacement response compared to the non-impacted specimens. However, the load carrying capacity of GG reduced by 63% and 79% and stiffness dropped by 75% and 89% at 40 J and 50 J, respectively due to the core fracture. The bending resistance of the GK sandwich core also decreased with the increase of impact energy due to the existence of core struts damage. The load carrying capacity of GK decreased by 37% and 60%, and stiffness dropped by 17% and 25% at 40 J and 50 J, respectively. On the other hand, GZ showed better resistance compared with GG and GK. The bending loads capacity reduced by 15% and 23% and the stiffness dropped by 2% and 20% at 40 J and 50 J, respectively. This was due to the replacement of one layer of GG fibre by the high-performance GZ fibre which increased impact resistance and protected the core from the damaging effect of impact force.

Figure 6.13 shows the residual load-strain response on the upper face sheet of the TCS structures under four-point bending after low-velocity impact. Interestingly, all specimens except GG at 40 J and 50 J showed tensile strain (Figure 6.13a-c) in the upper face sheet. As the structure's core bent (no fracture), the upper face sheet moved upward with an increasing of the four-point bending loads; the middle of the upper face sheet showed the tensile strain. Furthermore, core struts (non-damage of the upper angle of the core) attempted to buckle the core in the inner/outer region of the trapezoidal area. On the other hand, the compressive strain in TCS structure GG at 40 J and 50 J (Figure 6.13a) was due to the core rupture followed by de-bonding between upper skin and core when subjected to a low-velocity impact that created positive moment (compressive strain) at the top skin under four-point bending.

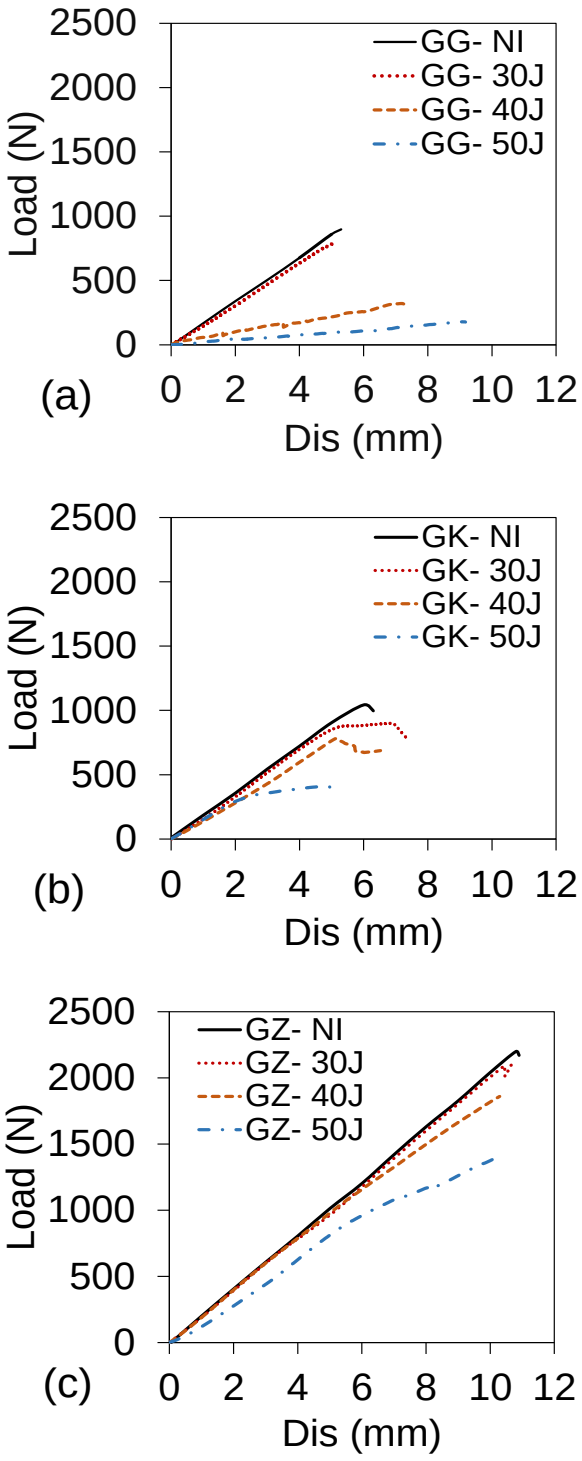

Figure 6.12: Force-displacement response of non-impacted and impacted TCS structures under four-point bending (a) GG, (b) GK, and (c) GZ

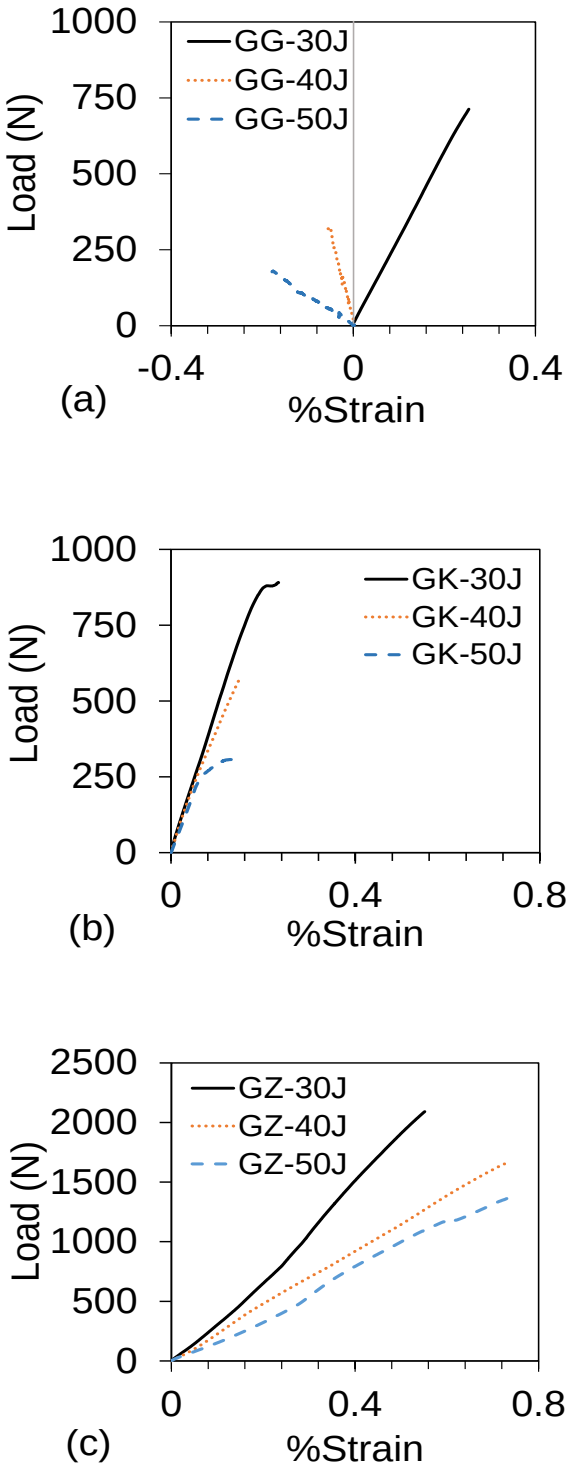

Figure 6.13: Load-strain response of the TCS structures under four-point bending after impact a) GG, b) GK, and c) GZ

Figure 6.14(a) shows the variation in the residual capacities of TCS structures GG, GK, and GZ with respect to impact energy. At 30 J, the residual capacity of all specimens is very similar to the initial strength. This was due to the low level of applied energy, just above the threshold limit, as discussed before. A significant drop was noticed between 30 J and 40 J because the specimen exhibited de-bonding and buckling at 40 J. However, the reduction of the capacity was comparatively lower between 40 and 50 J than between 30 and 40 J as no major changes in failure mode were observed between 40 and 50 J, as indicated in Table 4.

Figure 6.14(b) shows the normalised variation of the residual capacity with respect to the applied energy. This normalised variation is useful to compare the rate of changes in capacity with applied energy. It can be seen that the rate of reduction of the capacity is the lowest for GZ, followed by GK and GG. In other words, at 50 J kinetic energy, the residual strength and stiffness of GZ was 37% and 5% more than GK and 56% and 69% more than GG, respectively. This implies that the replacement of one layer of glass fibre by high-performance zylon is effective in maintaining the initial capacity of the TCS structures.

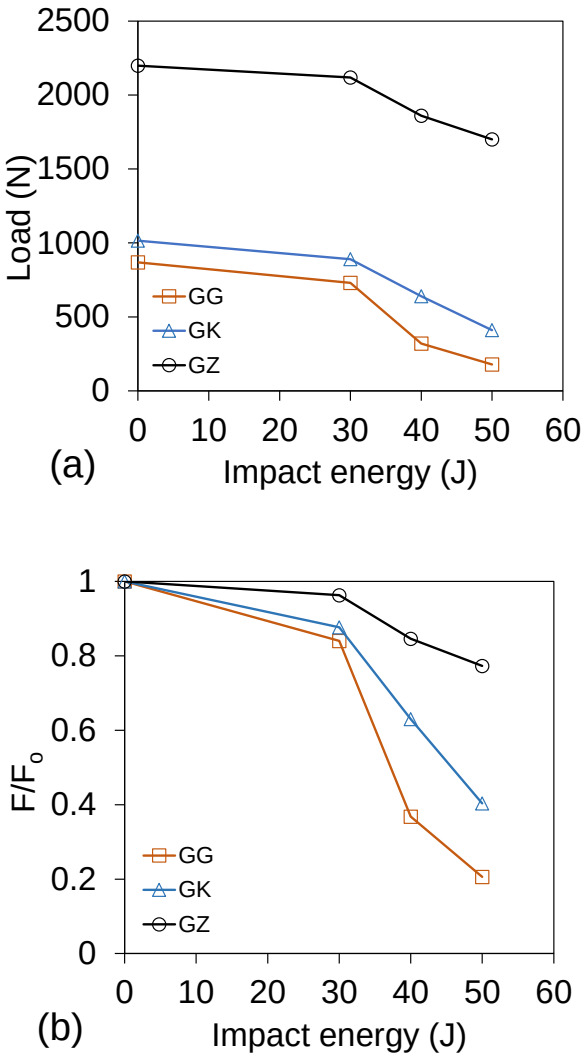

Figure 6.14: Residual strength of TCS structures GG, GK, and GZ under four-point bending a) Residual capacity Vs. impact energy, and b) Normalised residual capacity vs. impact energy

6.3.7 The empirical modelling

Experimentation is the preferred choice to understand the residual capacity after the impact event of the hybridized TCS structures. However, a systematic reduction of a large number of data points and multiple curve fitting to reduced data to a parameter model has been developed for prediction of the residual capacity of the structure. Figure 6.14(b) showed the variation of the normalised residual capacity (F/F_0) with the increase of impact energy which can be predicted by Eq. (1). In Eq. (1) α and β are the material constants while E is the kinetic energy of the impactor. The material constant α is the function of β which can be determined by Eq. (2). The magnitude of β is dependent on the impact strength of the material and an increase of impact capacity

reduces the β value. In the present study, the magnitude of β is 1 for GG and this reduced to 0.54 for GK and to 0.15 for GZ. It is worth mentioning that Eq. (1) and Eq. (2) were developed based on the kinetic energy ranging from 30 J to 50 J. Table 6.9 displays the calculated residual capacity using an empirical equation and compares it with the experimental results. It can be seen that the empirical equation can estimate the residual capacity within 10% of the experimental results.

$$\frac{F}{F_o} = 7\alpha e^{-\beta E} \quad (1)$$

$$\alpha = 0.15e^{1.9\beta} \quad (2)$$

Table 6.9. Comparison between experimental and empirical results of impact force

Sandwich type	Experimental (F/F_o)	Empirical eq. (F/F_o)	% Variation
GG-30J	0.839	0.807	3.9
GG-40J	0.368	0.392	6.4
GG-50J	0.205	0.191	7.2
GK-30J	0.876	0.872	0.5
GK-40J	0.630	0.591	6.2
GK-50J	0.403	0.400	0.9
GZ-30J	0.963	1.01	4.8
GZ-40J	0.845	0.908	7.3
GZ-50J	0.773	0.801	3.6

The proposed model can be improved further by considering the effect of a multi-layer replacement instead of the one-ply examined in the current study. Moreover, the influence of a wide range of impact energy, geometrical parameters and material properties needs to be included for establishing a robust model. Further studies are recommended in the aforementioned areas.

6.4 Summary

In this chapter the outcomes of the experimental results of two case studies were discussed. The first case dealt with the low-velocity impact on the full-scale multi-cell TCS structure at a high level of impact energy. The TCS structures had different core height-to-pitch ratios. The results revealed that the full-scale TCS structure has a shown high impact resistance and energy absorption energy compare with a single-cell TCS structure. In addition, increasing the core-height-to-pitch ratio minimized the sandwich damage mechanism, which means that the TCS structure can significantly protect the small apparatuses that were laid in the core cavity.

In the second case, the hybridized core sandwiches using high-performance fibre were tested under low-velocity impact, then tested by four-point bending tests. Firstly, the impact behaviour of the novel composite core of the TCS structures was investigated. This was followed by the investigation of the damage modes of the core and impact area of the upper face sheet, then the energy dissipation of the TCS structures was studied. Finally, the residual capacity after impact was investigated under the four-point bending tests.

The results showed that the concept of hybridizing a glass fibre core with high-performance zylon is more effective when TCS structures are subjected to an impact energy well above the threshold limit for damage. Replacing 25% of the glass fibre by kevlar and zylon fibres eliminated severe core failure. Moreover, the failure in the glass-glass combination was internal and therefore difficult to detect by visual inspection. This limitation can be overcome by glass-zylon hybridization as the failure is external due to its superior energy absorption ability.

The glass-zylon hybridization also distributed the impact force over a wider area on the upper face sheet compared to the glass-kevlar or glass-glass combination. This distribution minimized stress concentration and enhanced the impact capacity of the TCS structures. Employing high-performance ply in the TCS structure core provided high SEA without increasing structural weight. This achievement can be considered as a significant enhancement for the TCS structures, particularly for severe impact situations. The results also revealed that the glass-kevlar and glass-zylon combination offered better SEA than other traditional core materials such as expanded polypropylene, aluminium, rubber and plastic.

The four-point bending after impact also showed the loss of strength and stiffness of TCS structures due to impact events. The strength was lower in glass-zylon hybridization than in glass-kevlar and glass-glass combinations. At an applied energy of 50 J, the residual strength and stiffness of the glass-zylon was 37% and 5% more than for glass-kevlar and 56% and 69% more than the glass-glass combination, respectively. The proposed empirical equations estimated the residual capacity within 10% accuracy.

Finite element simulation for the hybrid core of TCS structures with high-performance synthetic fibre was not conducted due to time limitations. This can be performed in the future to gain more information about these new hybrid corrugated core of the TCS structures. In addition, repairing the damaged area of the impacted zone of the upper face sheet is another important point which can be considered for future investigations.

Chapter 7

Conclusions and Future Work

7.1 Introduction

Composite core sandwich structures have made inroads into aerospace, marine, and automotive applications during the past few decades and have largely replaced traditional sandwich structures. The main objectives of this research work were to investigate in depth the mechanical behaviours of innovative fabricated trapezoidal composite corrugated core sandwich (TCS) structures under various static and dynamic loading conditions. The impact behaviour and performances of single-cell TCS structures have been tested in the worst case scenario and compared with multi-cell TCS. In addition, a comprehensive FE analysis has been undertaken to analyse TCS structures under static and dynamic loading. Subsequently, an effective approach has been established to perform a parametric study to optimize the sandwich core design. Two case studies have been performed to understand the behaviour and performance of full-scale hybrid multi-cell TCS structures. This chapter presents the major findings of this study. Recommendations for further research are also detailed.

7.2 Major Conclusions

The following sections summarize the major conclusions of this research work.

7.2.1 Design and manufacture TCS structures

- An innovative TCS structure was designed and manufactured with woven E-glass fibre reinforced epoxy composite materials. The TCS structure was modified geometrically and woven E-glass fibre reinforced epoxy was later hybridized with high-performing fibre: kevlar and zylon, separately, for comparison purposes. Most importantly, the TCS structure unit cell's total weight was kept to a minimum as much as possible.

7.2.2 The TCS structures under quasi-static compression load: experimental

- As detailed in Chapter 4, the woven E-glass fibre reinforced epoxy composite single-cell TCS structure performed well, as anticipated, under quasi-static compression load. It behaved as a ductile structure when supported in CD. However, it showed brittle structural behaviour supported in MD. These findings prove that TCS structures are highly anisotropic and their mechanical behaviour is superior compared to traditional foam and honeycomb sandwich. It was seen that an increase in core thickness significantly increased the TCS structure's compression strength/stiffness and energy absorption capability. Results also demonstrate such TCS structures offer better mechanical properties than several cores used in aerospace applications, such as CFRP lattice core.

7.2.3 TCS structures under low-velocity impact: experimental

The woven E-glass fibre reinforced epoxy composite TCS structures have been tested with low-velocity impact at the visible damage threshold energy and roughly 30% greater than the visible energy level of the composite parent materials to understand the damage behaviour of these TCS structures.

- Superior impact performances were observed for TCS structures under low-velocity impact. Specifically, the TCS structures showed high impact resistance and absorbed impact energy more than the visible damage threshold energy without noticeable core damage.
- At visible damage threshold energy, the impactor shape was noted to influence the force-time response of the woven E-glass fibre reinforced epoxy composite TCS structure. Flat hemispherical and conical, heads were compared. Apart from the conical head, barely visible damage traces were left on the composite upper face sheet. Furthermore, microscopic inspection of the cross-sections of impact areas showed hidden damage to the flat and hemispherical impactor heads.
- The impact behaviour of TCS structures with changing core geometry and laminate configuration was investigated. The kinetic energy was raised to 30% over the visible damage threshold energy due to there having been no observed core damage with impact energy at the visible damage threshold. The resulting impact situations have shown the rigour of the novel TCS structures proposed in this study.

- The core thickness (tc) was found to be the most critical design parameter followed by the core height (h). The increase of core thickness (tc) increased the composite sandwich strength by reducing core buckling. However, the increase of core height (h) minimized impact resistance by increasing the elastic deformation of the sandwich. The design of the TCS structure can be optimal if the L1/h ratio approaches unity. The main damage mode of the TCS structure was the core failure at the junction of short span and core strut (at the location of w2 angle), followed by flattening of the lower angle (w1) of the core.
- In the literature, the existing theoretical formula cannot reliably predict impact forces for hemispherical and conical impactor heads. This study introduced an impactor head shape factor into the existing formula for reliable prediction. The modified equation predicted impact forces within 10% accuracy of the experimental results when the shape factors of 1, 0.9 and 0.7 were applied for flat, hemispherical and conical impactor heads, respectively.
- The proposed composite core exhibited a superior strength to weight ratio compared to traditional sandwich cores such as honeycomb, truss, foam, triangular, and sinusoidal.
- In comparison to the single-cell TCS structure, the multi-cell TCS structure not only increased the impact force but also provided functional and structural integrity and composite action between adjacent cells. Moreover, the multi-cell TCS structure showed better scenarios in terms of fracture compared to the single-cell TCS structure.
- A large impactor weight caused a significant damage area under the impactor head and increased the impact time for the same level of impact energy, while there was no significant disparity in the peak load values.

7.2.4 Finite element simulation of TCS structure

There has been a large knowledge gap in the FEA of TCS structures for impact loading simulation. This researcher has completed notable FE modelling work on the simulation of woven E-glass fibre reinforced epoxy composite TCS structures using the commercially available FEA program ANSYS-R9.1 under quasi-static and low-velocity impacts. The following conclusions are drawn from the FE simulation:

- The implicit and explicit dynamic 3D FE model showed an excellent correlation with the experimental results and significantly predicted the mechanical

behaviour, damage area, and energy absorption capability of the TCS structures. The FE model can be successfully extended to design improvements and optimizations further.

- The 3D FE model showed an excellent analysis of stress concentration and revealed that the upper core angle experienced a high stress concentration reaching the failure stress of the parent materials; it is a weak point in the TCS structure.
- With numerical optimization of the TCS structure, the superlative design point is 30 mm each of the core height (P1) and short span (P4), and 90 mm of the core long span (P5). With these values, the ultimate stress of the TCS structure (P6) comes close to the value of the ultimate stress of the core parent material.

7.2.5 Case studies of TCS structures under low-velocity impact

- Finally, two case studies of full-scale woven E-glass fibre reinforced epoxy composite and hybrid TCS structures have been undertaken to prove the concept of TCS structures.
- The full-scale multi-cell TCS structure performed as anticipated and followed the performances shown by the single-cell TCS structures. However, the full-scale TCS structure showed the highest impact resistance, the highest energy absorption energy and superior performance compared to single-cell TCS structures. Furthermore, in the full-scale TCS structure, the increase of the core height-to-pitch minimized the TCS fracture; this superior feature can be exploited to protect the small apparatuses that were laid in the core cavity.
- In the second case, it is interesting to see that the hybridization of the laminate showed superior performances. From the experimental results, the following conclusions have been drawn:
- Replacing 25% of the glass fibre by kevlar and zylon fibres of TCS structures core eliminated severe core failure. The core failure in the TCS structure GG was internal damage that was difficult to detect by visual inspection, while the GZ hybridized core showed an external failure. Furthermore, this external damage of the GZ hybrid TCS structure makes it easily repairable which has not been achievable with traditional sandwich structures.
- Employing kevlar and zylon ply in the TCS structure core provided high specific energy absorption without increasing the structural weight; it offered better SEA

than the other traditional core materials such as expanded polypropylene, aluminium, rubber, and plastic.

- The residual strength and stiffness of the TCS structure GZ were 37% and 5% more than the GK and 56% and 69% more than the GG combinations, respectively, when the applied energy was 50 J. Furthermore, the proposed empirical equations estimated the residual capacity within 10% accuracy.

Finally, it can be concluded that the innovative TCS structure proposed in this study has shown its superior performances to traditional metallic core sandwich structures. The most important feature of this innovative TCS structure is its notable strength to weight ratio. The reinforced composite construction has made the TCS structure strong and lightweight, which makes this structure the most impeccable alternative core structure for high-end aerospace, marine and automobile applications.

7.3 Research contributions

- Design and fabrication of woven E-glass fibre composite: single-cell, multi-cell, full-scale, and hybrid composite TCS structures with a low-cost handmade technique.
- Identification of the effect of support conditions (CD and MD) under the lower face sheet of the TCS structure on its mechanical behaviours, which was not previously determined in the existing literature.
- Clarification of the status of trapezoidal composite corrugated core compared with other composite core types under quasi-static load condition.
- Identification of the effect of the core geometrical parameters: core thickness, height, and short span on the mechanical behaviour and damage mechanism of TCS structures under low-velocity impact, and 3D plotting to explain the relation between them.
- Construction of an accurate FE model of the TCS structure under quasi-static and low-velocity impact.
- Determination of an optimized geometry of trapezoidal composite core under quasi-static condition using FE model.
- Establishment of a novel hybrid TCS structure using high-performance fibre with woven E-glass fibre, which is an innovative core design not be found in the literature. This hybrid TCS structure prevented core damage while maintaining

the structure's residual strength. This is highly significant as currently used structures suffer from unseen core damage and can consequently be prone to unexpected catastrophic failure.

7.4 Recommendations for Future Work

This study presented the experimental investigation and FE modelling of woven E-glass fibre reinforced epoxy composite TCS structures under quasi-static compression load and low-velocity impact. The following are the recommended areas for further investigation based on the results of this research work:

- Further experimental tests should be performed to fully characterize the mechanical behaviours of TCS structures under bending, tensile, and torsion loading conditions. In addition, long term behaviour needs to be established through fatigue, creep and other environmental type testing.
- The FE modelling work that has been presented in this study needs to be extended to predict micro-failure of the TCS structures under low-velocity impact behaviours.
- High-velocity impact tests need to be carried out on a range of hybrid TCS structures to characterize the damage mode.

References:

ANDERSON, T. & MADENCI, E. 2000. Experimental investigation of low-velocity impact characteristics of sandwich composites. *Composite Structures,* 50**,** 239-247.

ANSYS_HELP. 2019. *www.ansyshelp.ansys.com* [Online]. [Accessed].

ASHBY, M. 2010. Material Selection in Mechanical Design (Volume III). Third. Butterworth Heinemann, UK.

ASHBY, M. F. 2000. Multi-objective optimization in material design and selection. *Acta Materialia,* 48**,** 359-369.

ASTM-D379 2013. Standard test method for shear properties of composite materials by the V-Notched beam method USA: ASTM International

ASTM-D3039 2017. standard test Method for tensile properties of polymer matrix composite materials USA: ASTM International

ASTM-D5467/D5467M 2017. Standard test method for compressive properties of unidirectional polymer matrix composite materials using a sandwich beam USA: ASTM International

ASTM-D6641 2014. Standard test method for compressive properties of polymer matrix composite materials using a combined loading compression (CLC) test fixture USA: ASTM international

ASTM-D7136 2012. Standard test method for measuring the damage resistance of a fiber-reinforced polymer matrix composite to drop-weight impact event. USA: ASTM International.

AYMERICH, F., DORE, F. & PRIOLO, P. 2009. Simulation of multiple delaminations in impacted cross-ply laminates using a finite element model based on cohesive interface elements. *Composites Science and Technology,* 69**,** 1699-1709.

BAPANAPALLI, S. K., MARTINEZ, O. M., GOGU, C., SANKAR, B. V., HAFTKA, R. T. & BLOSSER, M. L. 2006. Analysis and design of corrugated core sandwich panels for thermal protection systems of space vehicles. *AIAA paper,* 1942**,** 2006.

BAROUTAJI, A., GILCHRIST, M. D., SMYTH, D. & OLABI, A. G. 2015. Analysis and optimization of sandwich tubes energy absorbers under lateral loading. *International Journal of Impact Engineering,* 82**,** 74-88.

BARTOLOZZI, G., BALDANZINI, N. & PIERINI, M. 2014. Equivalent properties for corrugated cores of sandwich structures: A general analytical method. *Composite Structures,* 108**,** 736-746.

BARTOLOZZI, G., BALDANZINI, N., PIERINI, M. & ZONFRILLO, G. 2015. Static and dynamic experimental validation of analytical homogenization models for corrugated core sandwich panels. *Composite Structures,* 125**,** 343-353.

BEZAZI, A., FRIOUI, N. & SCARPA, F. 2011. Tensile static, fatigue and relaxation behaviour of closed cell electret PVDF foams. *Mechanics of Materials,* 43**,** 459-466.

BOONKONG, T., SHEN, Y. O., GUAN, Z. W. & CANTWELL, W. J. 2016. The low velocity impact response of curvilinear-core sandwich structures. *International Journal of Impact Engineering,* 93**,** 28-38.

BULL, D., SPEARING, S. & SINCLAIR, I. 2015. Investigation of the response to low velocity impact and quasi-static indentation loading of particle-toughened

carbon-fibre composite materials. *Composites Part A: Applied Science and Manufacturing,* 74**,** 38-46.
CHANG, W.-S. 2004. Elasto-plastic analysis of corrugated sandwich steel panels.
CHEN, Y., HOU, S., FU, K., HAN, X. & YE, L. 2017. Low-velocity impact response of composite sandwich structures: Modelling and experiment. *Composite Structures,* 168**,** 322-334.
CLARKE, J. L. 2014. *Structural design of polymer composites: Eurocomp design code and background document*, CRC Press.
COLAN-AUSTRALIA 2017. Composite reinforcements fabric and tape product range, www.colan.com.au.
CÔTÉ, F., DESHPANDE, V. S., FLECK, N. A. & EVANS, A. G. 2006. The compressive and shear responses of corrugated and diamond lattice materials. *International Journal of Solids and Structures,* 43**,** 6220-6242.
DAVIES, G. & OLSSON, R. 2004. Impact on composite structures. *The Aeronautical Journal,* 108**,** 541-563.
DAYYANI, I., FRISWELL, M. I., ZIAEI-RAD, S. & FLORES, E. S. 2013a. Equivalent models of composite corrugated cores with elastomeric coatings for morphing structures. *Composite Structures,* 104**,** 281-292.
DAYYANI, I., FRISWELL, M. I., ZIAEI-RAD, S. & SAAVEDRA FLORES, E. I. 2013b. Equivalent models of composite corrugated cores with elastomeric coatings for morphing structures. *Composite Structures,* 104**,** 281-292.
DAYYANI, I., SHAW, A. D., SAAVEDRA FLORES, E. I. & FRISWELL, M. I. 2015. The mechanics of composite corrugated structures: A review with applications in morphing aircraft. *Composite Structures,* 133**,** 358-380.
DEAR, J. P., LEE, H. & BROWN, S. A. 2005. Impact damage processes in composite sheet and sandwich honeycomb materials. *International Journal of Impact Engineering,* 32**,** 130-154.
DEFRANCISCI, G., CHEN, Z. M., RHYMER, J., FUNAI, S., DELANEY, M., FUNG, S., LE, J., WHITE, S. & KIM, H. 2012. Impact Damage Formation on Composite Aircraft Structures. Department of Structural Engineering, University of California San Diego.
DELASSUS, P., BROWN, W., HOWELL, B. & MARSH, K. 1997. Encyclopedia of Packaging Technology. John Wiley and Sons, Inc., New York, NY.
DHARMASENA, K. P., WADLEY, H. N. G., LIU, T. & DESHPANDE, V. S. 2013. The dynamic response of edge clamped plates loaded by spherically expanding sand shells. *International Journal of Impact Engineering,* 62**,** 182-195.
DJAMA, K., MICHEL, L., GABOR, A. & FERRIER, E. 2019. Mechanical behaviour of a sandwich panel composed of hybrid skins and novel glass fibre reinforced polymer truss core. *Composite Structures,* 215**,** 35-48.
DONGMEI, W. 2009. Cushioning properties of multi-layer corrugated sandwich structures. *Journal of Sandwich Structures & Materials,* 11**,** 57-66.
ELKINGTON, M., BLOOM, D., WARD, C., CHATZIMICHALI, A. & POTTER, K. 2015. Hand layup: understanding the manual process. *Advanced Manufacturing: Polymer & Composites Science,* 1**,** 138-151.
EVANS, A. G., HUTCHINSON, J. W., FLECK, N. A., ASHBY, M. & WADLEY, H. 2001. The topological design of multifunctional cellular metals. *Progress in Materials Science,* 46**,** 309-327.
FAN, H., YANG, W. & ZHOU, Q. 2011. Experimental research of compressive responses of multi-layered woven textile sandwich panels under quasi-static loading. *Composites Part B: Engineering,* 42**,** 1151-1156.

FAN, H., ZHOU, Q., YANG, W. & JINGJING, Z. 2010. An experiment study on the failure mechanisms of woven textile sandwich panels under quasi-static loading. *Composites Part B: Engineering,* 41**,** 686-692.

FARSHIDI, A., BERGGREEN, C. & SCHÄUBLE, R. 2019. Numerical fracture analysis and model validation for disbonded honeycomb core sandwich composites. *Composite Structures,* 210**,** 231-238.

FENG, D. & AYMERICH, F. 2013. Damage prediction in composite sandwich panels subjected to low-velocity impact. *Composites Part A: Applied Science and Manufacturing,* 52**,** 12-22.

FRANCESCONI, L. & AYMERICH, F. 2018. Effect of Z-pinning on the impact resistance of composite laminates with different layups. *Composites Part A: Applied Science and Manufacturing,* 114**,** 136-148.

GAO, L., SUN, Y., CONG, L. & CHEN, P. 2013. Mechanical behaviours of composite sandwich panel with strengthened pyramidal truss cores. *Composite Structures,* 105**,** 149-152.

GHOLAMI, M., ALASHTI, R. A. & FATHI, A. 2016. Optimal design of a honeycomb core composite sandwich panel using evolutionary optimization algorithms. *Composite Structures,* 139**,** 254-262.

GURIT 2018. Guide to composites, www.gurit.com. Switzerland.

HALDAR, A. K., GUAN, Z. W., CANTWELL, W. J. & WANG, Q. Y. 2018. The compressive properties of sandwich structures based on an egg-box core design. *Composites Part B: Engineering,* 144**,** 143-152.

HAN, M. S. & CHO, J. U. 2014. Impact damage behavior of sandwich composite with aluminum foam core. *Transactions of Nonferrous Metals Society of China,* 24**,** s42-s46.

HASHIN, Z. 1980. Failure criteria for unidirectional fiber composites. *Journal of applied mechanics,* 47**,** 329-334.

HASHIN, Z. 1981. Fatigue failure criteria for combined cyclic stress. *International Journal of Fracture,* 17**,** 101-109.

HE, W., LIU, J., TAO, B., XIE, D., LIU, J. & ZHANG, M. 2016. Experimental and numerical research on the low velocity impact behavior of hybrid corrugated core sandwich structures. *Composite Structures,* 158**,** 30-43.

HERUP, E. J. & PALAZOTTO, A. N. 1998. Low-velocity impact damage initiation in graphite/epoxy/Nomex honeycomb-sandwich plates. *Composites Science and Technology,* 57**,** 1581-1598.

HOU, S., ZHAO, S., REN, L., HAN, X. & LI, Q. 2013. Crashworthiness optimization of corrugated sandwich panels. *Materials & Design,* 51**,** 1071-1084.

HOU, Y., NEVILLE, R., SCARPA, F., REMILLAT, C., GU, B. & RUZZENE, M. 2014. Graded conventional-auxetic Kirigami sandwich structures: Flatwise compression and edgewise loading. *Composites Part B: Engineering,* 59**,** 33-42.

HUANG, J., GONG, X., ZHANG, Q., SCARPA, F., LIU, Y. & LENG, J. 2016. In-plane mechanics of a novel zero Poisson's ratio honeycomb core. *Composites Part B: Engineering,* 89**,** 67-76.

HUANG, J., ZHANG, Q., SCARPA, F., LIU, Y. & LENG, J. 2017. In-plane elasticity of a novel auxetic honeycomb design. *Composites Part B: Engineering,* 110**,** 72-82.

ISO-527-1 2012. *Plastics- Determination of tensile properties* switzerland, International standard

IVAÑEZ, I. & SANCHEZ-SAEZ, S. 2013. Numerical modelling of the low-velocity impact response of composite sandwich beams with honeycomb core. *Composite Structures,* 106**,** 716-723.

JANG, B. P., HUANG, C. T., HSIEH, C. Y., KOWBEL, W. & JANG, B. Z. 1991. Repeated Impact Failure of Continuous Fiber Reinforced Thermoplastic and Thermoset Composites. *Journal of Composite Materials,* 25**,** 1171-1203.

JI, L., SHENG, X., XIAO, X., WEN, Z. & JIN, X. 2015. A review of mid-frequency vibro-acoustic modelling for high-speed train extruded aluminium panels as well as the most recent developments in hybrid modelling techniques. *Journal of Modern Transportation,* 23**,** 159-168.

JIN, F., CHEN, H., ZHAO, L., FAN, H., CAI, C. & KUANG, N. 2013. Failure mechanisms of sandwich composites with orthotropic integrated woven corrugated cores: Experiments. *Composite Structures,* 98**,** 53-58.

JONES, R. M. 1998. Mechanics of composite materials, CRC press.

KALANTARI, M., NAMI, M. R. & KADIVAR, M. H. 2010. Optimization of composite sandwich panel against impact using genetic algorithm. *International Journal of Impact Engineering,* 37**,** 599-604.

KAZEMAHVAZI, S., RUSSELL, B. P. & ZENKERT, D. 2012. Impact of carbon fibre/epoxy corrugated cores. *Composite Structures,* 94**,** 3300-3308.

KAZEMAHVAZI, S., TANNER, D. & ZENKERT, D. 2009. Corrugated all-composite sandwich structures. Part 2: Failure mechanisms and experimental programme. *Composites Science and Technology,* 69**,** 920-925.

KAZEMAHVAZI, S. & ZENKERT, D. 2009. Corrugated all-composite sandwich structures. Part 1: Modeling. *Composites Science and Technology,* 69**,** 913-919.

KıLıÇASLAN, C., GÜDEN, M., ODACı, İ. K. & TAŞDEMIRCI, A. 2013. The impact responses and the finite element modeling of layered trapezoidal corrugated aluminum core and aluminum sheet interlayer sandwich structures. *Materials & Design,* 46**,** 121-133.

KNOX, E. M., COWLING, M. J. & WINKLE, I. E. 1998. Adhesively bonded steel corrugated core sandwich construction for marine applications. *Marine Structures,* 11**,** 185-204.

LEIJTEN, J., BERSEE, H. E. N., BERGSMA, O. K. & BEUKERS, A. 2009. Experimental study of the low-velocity impact behaviour of primary sandwich structures in aircraft. *Composites Part A: Applied Science and Manufacturing,* 40**,** 164-175.

LI, T., MO, J., YU, X., SUO, T. & LI, Y. 2016. Mechanical behavior of C/SiC composites under hypervelocity impact at different temperatures: Micro-structures, damage and mechanisms. *Composites Part A: Applied Science and Manufacturing,* 88**,** 19-26.

LI, Z., KHENNANE, A., HAZELL, P. J. & BROWN, A. D. 2017. Impact behaviour of pultruded GFRP composites under low-velocity impact loading. *Composite Structures,* 168**,** 360-371.

LIANG, C.-C., YANG, M.-F. & WU, P.-W. 2001. Optimum design of metallic corrugated core sandwich panels subjected to blast loads. *Ocean Engineering,* 28**,** 825-861.

LIU, C., ZHANG, Y. X. & YE, L. 2017a. High velocity impact responses of sandwich panels with metal fibre laminate skins and aluminium foam core. *International Journal of Impact Engineering,* 100**,** 139-153.

LIU, J., CHEN, W., HAO, H. & WANG, Z. 2019. Numerical study of low-speed impact response of sandwich panel with tube filled honeycomb core. *Composite Structures,* 220**,** 736-748.

LIU, J., HE, W., XIE, D. & TAO, B. 2017b. The effect of impactor shape on the low-velocity impact behavior of hybrid corrugated core sandwich structures. *Composites Part B: Engineering,* 111**,** 315-331.

LIU, T. & TURNER, P. 2017. Dynamic compressive response of wrapped carbon fibre composite corrugated cores. *Composite Structures,* 165**,** 266-272.

LOK, T.-S. & CHENG, Q.-H. 2000. Elastic stiffness properties and behavior of truss-core sandwich panel. *Journal of Structural Engineering,* 126**,** 552-559.

MADENCI, E. & GUVEN, I. 2006. The finite element method and applications in engineering using ANSYS.

MALCOM, A. J., ARONSON, M. T., DESHPANDE, V. S. & WADLEY, H. N. G. 2013. Compressive response of glass fiber composite sandwich structures. *Composites Part A: Applied Science and Manufacturing,* 54**,** 88-97.

MATSUMOTO, M., MASAI, K. & WAJIMA, T. 1999. New technologies for railway trains. *Hitachi Rev,* 48**,** 134-138.

MOHAMMADI, H., ZIAEI-RAD, S. & DAYYANI, I. 2015. An equivalent model for trapezoidal corrugated cores based on homogenization method. *Composite Structures,* 131**,** 160-170.

MORADA, G., OUADDAY, R., VADEAN, A. & BOUKHILI, R. 2017. Low-velocity impact resistance of ATH/epoxy core sandwich composite panels: Experimental and numerical analyses. *Composites Part B: Engineering,* 114**,** 418-431.

MUELLER, J., MATLACK, K. H., SHEA, K. & DARAIO, C. 2019. Energy Absorption Properties of Periodic and Stochastic 3D Lattice Materials. *Advanced Theory and Simulations,* 2**,** 1900081.

ODACı, İ. K., KıLıÇASLAN, C., TAŞDEMIRCI, A. & GÜDEN, M. 2012. Projectile impact testing of glass fiber-reinforced composite and layered corrugated aluminium and aluminium foam core sandwich panels: a comparative study. *International Journal of Crashworthiness,* 17**,** 508-518.

OLMO, E., GRANDE, E., SAMARTIN, C. R., BEZDENEJNYKH, M., TORRES, J., BLANCO, N., FROVEL, M. & CAÑAS, J. 2012. Lattice structures for aerospace applications. *European Space Agency, (Special Publication) ESA SP,* 691.

OMKAR, S. N., KHANDELWAL, R., ANANTH, T. V. S., NARAYANA NAIK, G. & GOPALAKRISHNAN, S. 2009. Quantum behaved Particle Swarm Optimization (QPSO) for multi-objective design optimization of composite structures. *Expert Systems with Applications,* 36**,** 11312-11322.

OTHMAN, A. R. & BARTON, D. C. 2008. Failure initiation and propagation characteristics of honeycomb sandwich composites. *Composite Structures,* 85**,** 126-138.

PARK, S., RUSSELL, B. P., DESHPANDE, V. S. & FLECK, N. A. 2012. Dynamic compressive response of composite square honeycombs. *Composites Part A: Applied Science and Manufacturing,* 43**,** 527-536.

QIN, Q., ZHANG, W., LIU, S., LI, J., ZHANG, J. & POH, L. H. 2018. On dynamic response of corrugated sandwich beams with metal foam-filled folded plate core subjected to low-velocity impact. *Composites Part A: Applied Science and Manufacturing,* 114**,** 107-116.

QUEHEILLALT, D. T. & WADLEY, H. N. 2005. Cellular metal lattices with hollow trusses. *Acta Materialia,* 53**,** 303-313.

REJAB, M. R. M. & CANTWELL, W. J. 2013. The mechanical behaviour of corrugated-core sandwich panels. *Composites Part B: Engineering,* 47**,** 267-277.

RONG, Y., LIU, J., LUO, W. & HE, W. 2018. Effects of geometric configurations of corrugated cores on the local impact and planar compression of sandwich panels. *Composites Part B: Engineering,* 152**,** 324-335.

RUSSELL, B. P., MALCOM, A., WADLEY, H. N. & DESHPANDE, V. 2010. Dynamic compressive response of composite corrugated cores. *J Mech Mater Struct,* 5**,** 477-93.

SAKLY, A., LAKSIMI, A., KEBIR, H. & BENMEDAKHEN, S. 2016. Experimental and modelling study of low velocity impacts on composite sandwich structures for railway applications. *Engineering Failure Analysis,* 68**,** 22-31.

SANG, L., HAN, S., PENG, X., JIAN, X. & WANG, J. 2019. Development of 3D-printed basalt fiber reinforced thermoplastic honeycombs with enhanced compressive mechanical properties. *Composites Part A: Applied Science and Manufacturing,* 125.

SCHNEIDER, C., KAZEMAHVAZI, S., ZENKERT, D. & DESHPANDE, V. S. 2015. Dynamic compression response of self-reinforced poly(ethylene terephthalate) composites and corrugated sandwich cores. *Composites Part A: Applied Science and Manufacturing,* 77**,** 96-105.

SCHNEIDER, C., ZENKERT, D., DESHPANDE, V. S. & KAZEMAHVAZI, S. 2016. Bending energy absorption of self-reinforced poly(ethylene terephthalate) composite sandwich beams. *Composite Structures,* 140**,** 582-589.

SCHUBEL, P. M., LUO, J.-J. & DANIEL, I. M. 2007. Impact and post impact behavior of composite sandwich panels. *Composites Part A: Applied Science and Manufacturing,* 38**,** 1051-1057.

SCHULTZ, M., OREMONT, L., GUZMAN, J. C., MCCARVILLE, D., ROSE, C. & HILBURGER, M. Compression Behavior of Fluted-Core Composite Panels. 52nd AIAA/ASME/ASCE/AHS/ASC Structures, Structural Dynamics and Materials Conference 19th AIAA/ASME/AHS Adaptive Structures Conference 13t, 2011. 2170.

SEVKAT, E., LIAW, B. & DELALE, F. 2013. Drop-weight impact response of hybrid composites impacted by impactor of various geometries. *Materials & Design (1980-2015),* 52**,** 67-77.

SHIN, K. B., LEE, J. Y. & CHO, S. H. 2008. An experimental study of low-velocity impact responses of sandwich panels for Korean low floor bus. *Composite Structures,* 84**,** 228-240.

SHIN, P.-S., WANG, Z.-J., KWON, D.-J., CHOI, J.-Y., SUNG, I., JIN, D.-S., KANG, S.-W., KIM, J.-C., DEVRIES, K. L. & PARK, J.-M. 2015. Optimum mixing ratio of epoxy for glass fiber reinforced composites with high thermal stability. *Composites Part B: Engineering,* 79**,** 132-137.

SONG, Z.-Z., CHENG, S., ZENG, T., YANG, F., JING, S.-D. & FANG, D.-N. 2015. Compressive behavior of C/SiC composite sandwich structure with stitched lattice core. *Composites Part B: Engineering,* 69**,** 243-248.

ST-PIERRE, L., DESHPANDE, V. S. & FLECK, N. A. 2015. The low velocity impact response of sandwich beams with a corrugated core or a Y-frame core. *International Journal of Mechanical Sciences,* 91**,** 71-80.

ST-PIERRE, L., FLECK, N. & DESHPANDE, V. 2012. Sandwich beams with corrugated and Y-frame cores: Does the back face contribute to the bending response? *Journal of Applied Mechanics,* 79**,** 011002.

STOLARSKI, T., NAKASONE, Y. & YOSHIMOTO, S. 2018. *Engineering analysis with ANSYS software,* Butterworth-Heinemann.

SUN, X. C. & HALLETT, S. R. 2018. Failure mechanisms and damage evolution of laminated composites under compression after impact (CAI): Experimental and numerical study. *Composites Part A: Applied Science and Manufacturing,* 104**,** 41-59.

SWANSON, S. R. & KIM, J. 2002. Optimization of Sandwich Beams for Concentrated Loads. *Journal of Sandwich Structures & Materials,* 4**,** 273-293.

TAKAHASHI, H., YOKOZEKI, T. & HIRANO, Y. 2016. Development of variable camber wing with morphing leading and trailing sections using corrugated structures. *Journal of Intelligent Material Systems and Structures,* 27**,** 2827-2836.

THILL, C., ETCHES, J., BOND, I., POTTER, K. & WEAVER, P. 2010. Composite corrugated structures for morphing wing skin applications. *Smart Materials and Structures,* 19**,** 124009.

TORRE, L. & KENNY, J. M. 2000. Impact testing and simulation of composite sandwich structures for civil transportation. *Composite Structures,* 50**,** 257-267.

TOYOBO 2005. PBO fiber zylon - Technical information about zylon, www.toyobo.co.jp Japan.

TWEDE, D., SELKE, S. E., KAMDEM, D.-P. & SHIRES, D. 2014. *Cartons, crates and corrugated board: handbook of paper and wood packaging technology,* DEStech Publications, Inc.

UDE, A. U., ARIFFIN, A. K. & AZHARI, C. H. 2013. Impact damage characteristics in reinforced woven natural silk/epoxy composite face-sheet and sandwich foam, coremat and honeycomb materials. *International Journal of Impact Engineering,* 58**,** 31-38.

VAIDYA, S., ZHANG, L., MADDALA, D., HEBERT, R., WRIGHT, J. T., SHUKLA, A. & KIM, J.-H. 2015. Quasi-static response of sandwich steel beams with corrugated cores. *Engineering Structures,* 97**,** 80-89.

VIGNJEVIC, R., CAMPBELL, J., HUGHES, K., ORŁOWSKI, M., GARCEA, S., WITHERS, P. & REED, J. 2019. Soft body impact resistance of composite foam core sandwich panels with unidirectional corrugated and tubular reinforcements. *International Journal of Impact Engineering,* 132.

VINSON, J. R. 2005. Sandwich structures: past, present, and future. *Sandwich structures 7: advancing with sandwich structures and materials.* Springer.

WADLEY, H. N. 2002. Cellular metals manufacturing. *Advanced Engineering Materials,* 4**,** 726-733.

WADLEY, H. N. 2005. Multifunctional periodic cellular metals. *Philosophical Transactions of the Royal Society A: Mathematical, Physical and Engineering Sciences,* 364**,** 31-68.

WADLEY, H. N. G., DHARMASENA, K. P., O'MASTA, M. R. & WETZEL, J. J. 2013a. Impact response of aluminum corrugated core sandwich panels. *International Journal of Impact Engineering,* 62**,** 114-128.

WADLEY, H. N. G., FLECK, N. A. & EVANS, A. G. 2003. Fabrication and structural performance of periodic cellular metal sandwich structures. *Composites Science and Technology,* 63**,** 2331-2343.

WADLEY, H. N. G., O'MASTA, M. R., DHARMASENA, K. P., COMPTON, B. G., GAMBLE, E. A. & ZOK, F. W. 2013b. Effect of core topology on projectile penetration in hybrid aluminum/alumina sandwich structures. *International Journal of Impact Engineering,* 62**,** 99-113.

WAHL, L., MAAS, S., WALDMANN, D., ZÜRBES, A. & FRÈRES, P. 2012. Shear stresses in honeycomb sandwich plates: Analytical solution, finite element method and experimental verification. *Journal of Sandwich Structures & Materials,* 14**,** 449-468.

WALSH, J., KIM, H.-I. & SUHR, J. 2017. Low velocity impact resistance and energy absorption of environmentally friendly expanded cork core-carbon fiber sandwich composites. *Composites Part A: Applied Science and Manufacturing,* 101**,** 290-296.

WANG, J., EVANS, A., DHARMASENA, K. & WADLEY, H. 2003. On the performance of truss panels with Kagome cores. *International Journal of Solids and Structures,* 40**,** 6981-6988.

WINKLER, M. 2012. *Analysis of corrugated laminates.* ETH Zurich.

WINKLER, M. & KRESS, G. 2010. Deformation limits for corrugated cross-ply laminates. *Composite Structures,* 92**,** 1458-1468.

XIE, W. H., MENG, S. H., DING, L., JIN, H., DU, S. Y., HAN, G. K., WANG, L. B., XU, C. H., SCARPA, F. & CHI, R. Q. 2018. High-temperature high-velocity impact on honeycomb sandwich panels. *Composites Part B: Engineering,* 138**,** 1-11.

XIONG, J., DU, Y., MOUSANEZHAD, D., EYDANI ASL, M., NORATO, J. & VAZIRI, A. 2019. Sandwich structures with prismatic and foam cores: a review. Advanced Engineering Materials, 21, 1800036.

XIONG, J., VAZIRI, A., MA, L., PAPADOPOULOS, J. & WU, L. 2012. Compression and impact testing of two-layer composite pyramidal-core sandwich panels. *Composite Structures,* 94**,** 793-801.

XU, G.-D., YANG, F., ZENG, T., CHENG, S. & WANG, Z.-H. 2016. Bending behavior of graded corrugated truss core composite sandwich beams. *Composite Structures,* 138**,** 342-351.

YASHIRO, S., OGI, K., YOSHIMURA, A. & SAKAIDA, Y. 2014. Characterization of high-velocity impact damage in CFRP laminates: Part II – prediction by smoothed particle hydrodynamics. *Composites Part A: Applied Science and Manufacturing,* 56**,** 308-318.

YE, G., BI, H. & HU, Y. 2020. Compression behaviors of 3D printed pyramidal lattice truss composite structures. *Composite Structures,* 233.

YELLUR, M. R., SEIDLITZ, H., KUKE, F., WARTIG, K. & TSOMBANIS, N. 2019. A low velocity impact study on press formed thermoplastic honeycomb sandwich panels. *Composite Structures,* 225.

YU, Y., YING, L., HOU, W.-B., HU, P., JIA, X.-X. & AKHMET, G. 2018. Failure analysis of adhesively bonded steel corrugated sandwich structures under three-point bending. *Composite Structures,* 184**,** 256-268.

ZANGANI, D., ROBINSON, M. & GIBSON, A. G. 2008. Energy Absorption Characteristics of Web-Core Sandwich Composite Panels Subjected to Drop-Weight Impact. *Applied Composite Materials,* 15**,** 139-156.

ZENKERT, D., SHIPSHA, A., BULL, P. & HAYMAN, B. 2005. Damage tolerance assessment of composite sandwich panels with localised damage. *Composites Science and Technology,* 65**,** 2597-2611.

ZHANG, G., WANG, B., MA, L., XIONG, J. & WU, L. 2013a. Response of sandwich structures with pyramidal truss cores under the compression and impact loading. *Composite Structures,* 100**,** 451-463.

ZHANG, J., QIN, Q. & WANG, T. J. 2013b. Compressive strengths and dynamic response of corrugated metal sandwich plates with unfilled and foam-filled sinusoidal plate cores. *Acta Mechanica,* 224**,** 759-775.

ZHANG, J., QIN, Q., XIANG, C., WANG, Z. & WANG, T. J. 2016a. A theoretical study of low-velocity impact of geometrically asymmetric sandwich beams. *International Journal of Impact Engineering,* 96**,** 35-49.

ZHANG, J., SUPERNAK, P., MUELLER-ALANDER, S. & WANG, C. H. 2013c. Improving the bending strength and energy absorption of corrugated sandwich composite structure. *Materials & Design,* 52**,** 767-773.

ZHANG, L., HEBERT, R., WRIGHT, J. T., SHUKLA, A. & KIM, J.-H. 2014. Dynamic response of corrugated sandwich steel plates with graded cores. *International Journal of Impact Engineering,* 65**,** 185-194.

ZHANG, P., CHENG, Y., LIU, J., LI, Y., ZHANG, C., HOU, H. & WANG, C. 2016b. Experimental study on the dynamic response of foam-filled corrugated core sandwich panels subjected to air blast loading. *Composites Part B: Engineering,* 105**,** 67-81.

ZHANG, Y., ZONG, Z., LIU, Q., MA, J., WU, Y. & LI, Q. 2017. Static and dynamic crushing responses of CFRP sandwich panels filled with different reinforced materials. *Materials & Design,* 117**,** 396-408.

ZHAO, Z.-Y., HAN, B., WANG, X., ZHANG, Q.-C. & LU, T. J. 2018. Out-of-plane compression of Ti-6Al-4V sandwich panels with corrugated channel cores. *Materials & Design,* 137**,** 463-472.

Appendices

Appendix A

Analytical model of trapezoidal corrugated core sandwich

Subjecting trapezoidal corrugated core to a compressive load can be simplified as the following analytical model as shown in Figure 1-A (a) (Rejab and Cantwell, 2013). It was supposed that compression on one unit cell of the trapezoidal corrugated core is *P* and then a unit cell strut will carry a compression load of 1/2*P* and have an axial displacement as shown in Figure 1-A (b). Each core strut was considered as a cantilever beam with the same axial load N , shear load R and, bending moment M as shown in Figure 1-A (c)

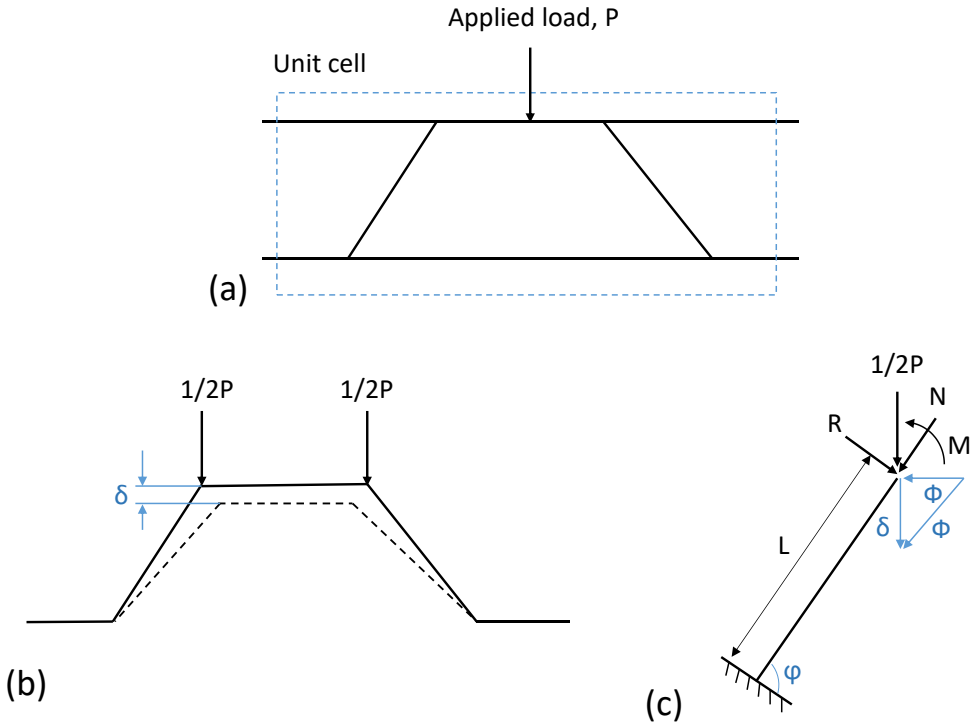

Figure 1-A (a) unit cell of trapezoidal corrugated core sandwich under compression load, (b) deformation of trapezoidal corrugated core under compression load, and (c) the force bod diagram of core strut under compression load

The conditions of load equilibrium was consider, the relationship between the supplied compressive load *P* and the displacement δ can be expressed as:

$$P = \frac{2E_c wt(L^2 sin^2 + t^2 cos^2)}{L^3} \delta \quad (1)$$

Where E_c is the Young's modulus of the parent materials of the corrugated core strut in the fibre direction and for the orthogonal laminate with even number layers is:

$$E_c = \frac{(E_{11}+E_{22})}{2} \quad (2)$$

Under compression load, the core strut has a possibility of elastic buckling modes and they are Euler buckling and core shear buckling. Form the classical Euler buckling theory the Euler buckling load can be estimated as:

$$P_E = \frac{\alpha^2 \pi^2 E_c wt^3 (L^2 sin^2 \varphi + t^2 cos^2 \varphi)}{2L^4 sin\varphi} \quad (3)$$

Where w, t, and L and are the core strut width, thickness and length respectively, and α is the boundary condition factor.

Noted that α=1 shows that the condition of the two ends of the core strut is simply-supported and α= 0.5 indicates that one end of the core strut is fixed and another is free to move.

Xiong et al. (2011) assumed that the shear stiffness of the corrugated core sandwich is approximately equals to that of the corrugated core, at neglecting the effect of the shear stiffness of the upper face sheet of the sandwich. Therefore the shear buckling load can be estimated as bellow:

$$P_s = \frac{G_c w sin2\varphi}{2L}$$

Where G_c is modulus of the effective shear of the corrugated core strut. The Gc can be calculated as bellow:

$$G_c = \frac{E_c t}{2L} sin2\varphi$$

According to Zenkert (1995) the critical buckling load can be written as :

$$\frac{1}{P_{cr}} = \frac{1}{P_E} + \frac{1}{P_s}$$

Appendix B

Analytical Model of Energy Absorption of the TCS Structure

Energy absorption in TCS due to compression or impact load is a major parameter design of corrugated core structure. Therefore, the following analytical method was devised to estimate energy absorption by corrugated core structure TCS structure due to compressive quasi-static loading (St-Pierre et al., 2015). Considering the research work done in Ref (Schneider et al., 2015) and (Zangani et al., 2008), it can be established a relationship as shown in Equation 1 to estimate an energy absorption of the members of the single-cell TCS structure as shown in Figure1-B (on overhanging support), when exposed to quasi-static compression load.

$$U_{TCS} = 2U_{cs} + U_{ls} \quad (1)$$

Let, U_{tcs} is absorbed energy by the unit cell TCS, U_{cs} and U_{lfs} are the absorbed energy by core struts and lower face sheets, respectively.

By a linear analysing of the structural members, the absorbed energy by core struts can be calculated from the formula Equation 2,

$$U_{cs} = \frac{N^2 L}{2AE} \quad (2)$$

Where N is applied load, L, A and E are the length of the member, cross-section and Young modulus, respectively. The core struts endure a buckling loading and crush load which means assuming that $N = p_R$, where, p_R is Rankine Gordon load, which is equal to the inverted summation of buckling and crushing load. According to Rankine Gordon formula,

$$\frac{1}{p_R} = \frac{1}{p_e} + \frac{1}{p_c} \quad (3)$$

By considering just the linear elastic response of core struts, the term $1/p_c$ will be neglected in Equation 3, $p_R = p_e$, where p_e is Euler buckling load. Utilizing a free body diagram of core struts, the load applied in the Y direction of the corrugated system and the core struts are fixed at the end, the Euler bucking is;

$$p_e = \frac{\pi^2 EI}{(kL)^2} \quad (4)$$

Where, E = E_x is the elastic modulus of composite materials in fibre direction, I is the second moment of area, L is the core struts length, and *k* is coefficient of end support of core struts (where *k* = 0.5 for 90 and 94 mm support position, and *k* =1 for 86 and 98mm support position in this case translation and rotation are free). Since the inclined members are acting as slender struts, the energy absorbed by core strut is;

$$U_{cs} = \frac{\pi^4 w t_c^5 E_x \sin^2\theta}{24 k^4 L^3} \quad (5)$$

Where *w* and t_c are the core sturts width and thickness respectively.

Under compression load on the top face sheet of the TCS structure, obviously, the lower face sheet undergoes abending as the bending moment created load transfer to the joint of strut and bottom sheet. In this case, depending on the elementary beam theory, an analytic expression for the lower face sheet energy absorption has been calculated. The strain energy of the bottom face sheet can be formed the Equation 6;

$$U_{lfs} = \frac{1}{2} \int_{-1/2L}^{1/2L} \frac{{\sigma_x}^2}{E_x} A dL \quad (6)$$

Where σ_x is the stress in the local X direction of core struts, i.e. fibre direction, and E_x is the Young modulus of the core struts. *A* and *L* are the area and length of the core struts respectively.

From the free body diagram of the lower face sheet of TCS structure, a relationship has been established between the compression load, deflection of lower face and support span length (with assuming a perfect bending of the lower face sheet). Fig.18 shows the deflection (Timoshenko and Gere, 1963) of the lower member and the support span. The deflection of the lower face sheet can be calculated as:

$$\delta_l = \frac{DB^2}{2r} \quad (7)$$

$$DB = \frac{1}{2} SL \quad (8)$$

Then, $$r = \frac{l_{ss}^2}{4\delta} \quad (9)$$

And,

$$\sigma_x = \frac{E_x y}{r} \quad (10)$$

Where δ is the lower face deflection, SL is the length of the span between supports, r is the curvature length, (y = t_c) is the core thickness.

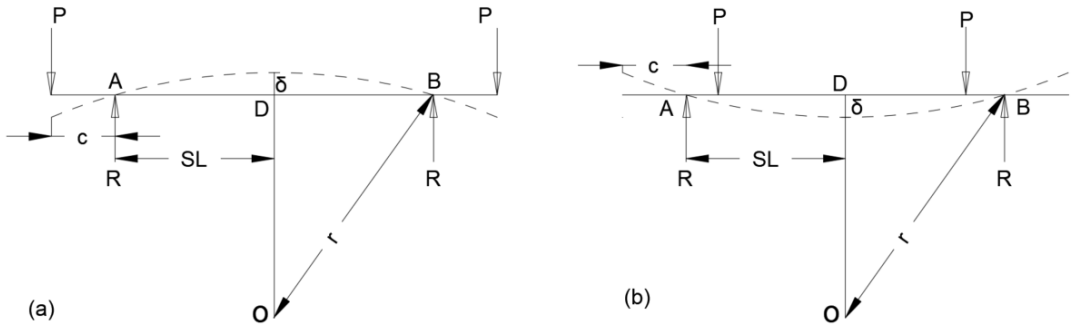

Figure 1-B: Bending of the lower face sheet of the TCS structure: (a) supports between the loading points, and (b) supports out of the loading points

From the Equations 6 to10, strain energy in the lower face sheet can be expressed as:

$$U_{lfs} = \frac{E_x w {\delta_l}^2 t_c^3}{SL^3} \qquad (11)$$

The estimated value of energy absorption by Equation 11 is very small in comparison with the Equation 5.

Substituting Equations 5 and 11 in Eqation1, the approximate energy absorption capability of the corrugation sandwich which is absorbed by the core struts and the lower face sheet can be estimated by the Equation12:

$$U_{TCS} = \frac{2\pi^4 w t_c^5 E_x \sin^2\theta}{24K^4 SL^3} + \frac{E_x w {\delta_l}^2 t_c^3}{SL^3} \qquad (12)$$

The Equation 12 is validated for energy absorption of TCS structure at the elastic response of the core struts. The first term of the equation is a modification of Euler-elastic buckling (before critical elastic failure point) involving the core angle and K as a coefficient of fixed end t of core struts. The second term shows the participation of the lower face sheet in structural energy absorption based on the support position.
Furthermore, the energy absorption capability of TCS structure (eq.12) is predicted to have a linear dependence on length support span (SL) and on the Euler coefficient of end support of core struts *k*; and thus on the lower core angle (θ). As a result, the structural strength and energy absorption capability will change with a variety of support span under the lower face of the corrugated sandwich.

The TCS absorbed energy capability (U_{AE}) can be considered as an indication of TCS ability to withstand the compression of the quasi-static load until its own failure. The global energy absorption of the single-cell TCS during each test was calculated by integrating the load-displacement curve up to a load of breaking the specimen. To acquiring the TCS energy absorption capability Equation 15 has been utilized (Hou et al., 2015).

$$U_{AE} = \int_0^{\delta} p(\delta) d\delta \tag{15}$$

Where U_{AE} absorbed energy, p quasi-static compressive load and δ the crosshead displacement.

Appendix C

Modification of the energy-balance model to match the TCS structure

At subjecting a panel to impact load a part of the kinetic energy is transformed to cause elastic deformation of the structural members, and the rest of the kinetic energy is dissipated through the failures core members (Zhang and Zhang, 2015). At assuming zero energy loss, the principle of the total energy conservation was applied to evaluate model energy balance. Based on the principle of total energy conservation between the composite plate and impactor head (Shivakumar et al., 1985), a theoretical model was developed for the TCS structure. Further, this analysis was carried out by assuming the infinitesimal time between the impact event and the instance of impactor's velocity equal to zero; therefore the TCS structure behaves approximately as a quasi-static deformation (Shivakumar et al., 1985, Abrate, 1998).

Modelling the structure using spring-mass elements will provide a reasonably accurate analytical model sufficient to investigate the impact response of TCS structure. Figure 1-C illustrates the model, which consists of spring-mass elements that represent structural members.

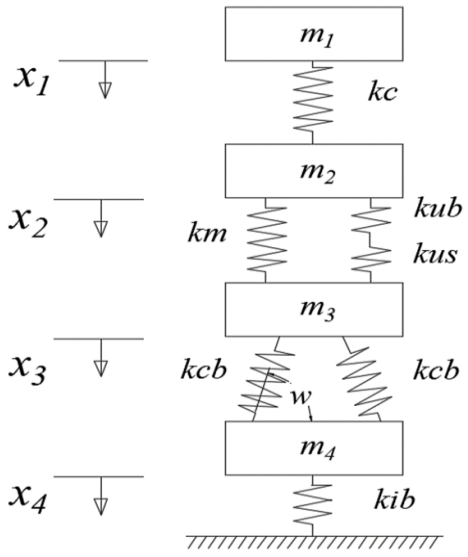

Figure 1-C: Shows the TCS structure- impact system which is consist of spring and mass of structural members

Where M1, M2, M3, and M4 represent the mass of impactor head, upper face sheet, core struts and lower face sheet face laminate respectively. K_c is the stiffness of contact spring, K_{ub}, K_{us} and are the linear bending, linear shear stiffness. K_m is nonlinear membrane stiffness of upper face sheet respectively. The K_{cb} is the core struts buckling stiffness. K_{lb} is the lower face sheet bending stiffness.

The equation energy balance model of the plate has been developed for TCS structure and according to that at t > 0 (until impactor velocity = 0) can be formulated as,

$$\frac{1}{2}M_iV^2 = E_c + E_{ub} + E_{uS} + E_{um} + E_{cb} + E_{lb} \quad (1)$$

Where M_i and V are the impactor mass and velocity. E_c, E_{ub}, E_{us}, E_m, E_{cb}, and E_{lb} refers to the energy of contact, upper face bending, upper face sheet shear, membrane deformation of upper face sheet, core struts buckling, and lower face sheet bending respectively. The integration of impact force and contact deformation of the upper face sheet lead to obtaining the contact energy.

$$E_c = \int_0^{\alpha} p d\alpha \quad (2)$$

Where P is contact force, α represents the indentation of the TCS structure by the impactor.

Where $p = n\alpha^{\frac{2}{3}}$, $n=K_c$ is the contact stiffness parameter. The n depends on the impactor radius and the material properties of the upper face sheet.

$$n = \frac{4\sqrt{r_i}}{3\pi(K_1+K_2)} \quad (3)$$

Where r_i is the impactor radius, K_1 and K_2 are the constants dependant on material Young modulus.

Depending on p and n values the Equation 2 can be written as,

$$E_c = \frac{2p^{\frac{5}{3}}}{5n^{\frac{2}{3}}} \quad (4)$$

The absorbed energy of bending and shear deformation upper of the upper face sheet is calculated by Equation 5 and membrane deformation energy by Equation 6,

$$E_{ubs} = \frac{1}{2}K_{ubs}(x_2 - x_3)^2 \quad (5)$$

Where K_{ubs} is the equivalent stiffness of bending and shear stiffness of the upper face sheet of the TCS structure.

And,

$$E_{um} = \frac{1}{4}K_{um}(x_2 - x_3)^4 \quad (6)$$

The absorbed energy of the core struts buckling and bending of the lower face sheet are estimated by Equation 7 and Equation 8,

$$E_{cb} = \frac{1}{2} K_{cb} (x_3 \cos w - x_4)^2 \qquad (7)$$

$$E_{lb} = \frac{1}{2} K_{lb} {x_4}^2 \qquad (8)$$

Where *w* is the core struts angle.

The force which is reactive from the impact of the sandwich can be determined from the components,

$$p = p_{bs} + p_m + p_{cb} \qquad (9)$$

Then,

$$p = K_{ubs} u_2 + K_m u_2^3 + K_{cb} u_3 + K_{lb} \qquad (10)$$

Where $u_1 = (x_1 - x_2)$, $u_2 = (x_2 - x_3 \cos w)$, $u_3 = (x_3 \cos w - x_4)$, and $u_4 = x_4$

By substituting Equation 10 in Equation 4, and substituting the Equations 4,5,6,7 and 8 in Equation 1. Then the energy balance of the TCS structure can be written as in Equation 11:

$$M_i V_o^2 = \frac{4[K_{ubs} u_2 + K_m u_2^3 + K_{cb} u_3 + K_{lb} u_4]^{\frac{5}{3}}}{5 n^{\frac{2}{3}}} + K_{ubs} {u_2}^2 + \frac{1}{2} K_m {u_2}^4 + K_{cb} {u_3}^2 + K_{lb} {u_4}^2 \qquad (11)$$

Equation 11 has four degrees of freedom, which represent the capability of the TCS structure to absorb the kinetic energy of impactor, involving different striker tips and velocity.

Appendix D

Numerical code of TCS structure

The ANSYS code of finite element modelling of the TCS structure can be used for doing more investigation of the mechanical behaviour of such structures. To obtain this code please contact the author via email address: sartip.engineering@gmail.com

Appendix E

Associated publications

Journals

Zangana S, Epaarachchi J, Ferdous W, Leng J. A novel hybridised composite sandwich core with Glass, Kevlar and Zylon fibres - Investigation under low-velocity impact. International Journal of Impact Engineering. 2020;137:103430. https://www.sciencedirect.com/science/article/pii/S0734743X1930778X

Zangana S, Epaarachchi J, Ferdous W, Leng J, S Peter. Behaviour of continuous fibre composite sandwich core under low-velocity impact. Journal of Thin-Walled Structures 158 (2020) 107157
http://www.elsevier.com/locate/tws

Zangana S, Epaarachchi J, Ferdous W, Leng J, S Peter. Optimization of an innovative trapezoidal composite corrugated core for sandwich structures. Prepared for submission, 2020.

Al Azzawi W Epaarachchi J, **Zangana S**. Development and Performance Investigation of a Novel Morphing Wing Design Using Shape Memory Polymers Composite Corrugated Structure. Papered to submit to the Journal of Composite Structures, 2020.

Refereed conference proceedings

S. Zangana, J. Epaarachchi1, CD. Tran1, and J. Leng 2016, 'Investigation of Stress distribution in Glass Fiber/Epoxy composite Trapezoidal Corrugated core elements due to a low-velocity impact load' paper presented to the 10th Asian-Australasian Conference on Composite Materials (ACCM10): Busan, Korea.

S. Zangana, J. Epaarachchi, P. Schubel, X. Zeng, J. Leng 2018, 'An Experimental and numerical study on the performance of composite corrugated core structure under compression load with various support conditions' paper presented to the 10th

Asian-Australasian Conference on Composite Materials (ACCM10): Cairns, Queensland, Australia.

S. Zangana, J. Epaarachchi, X. Zeng, J. Leng, P. Schubel 2019, 'Low velocity impact response of corrugated core sandwich panels - effect of impactor geometry' paper presented to the 22nd International Conference on Composite Materials: Melbourne, Australia.

References:

ABRATE, S. 1998. *Impact on composite structures,* The Edinburgh Building, Cambridge CB2 2RU, United Kingdom, Cambridge university press

HOU, S., SHU, C., ZHAO, S., LIU, T., HAN, X. & LI, Q. 2015. Experimental and numerical studies on multi-layered corrugated sandwich panels under crushing loading. *Composite Structures,* 126**,** 371-385.

REJAB, M. R. M. & CANTWELL, W. J. 2013. The mechanical behaviour of corrugated-core sandwich panels. *Composites Part B: Engineering,* 47**,** 267-277.

SCHNEIDER, C., KAZEMAHVAZI, S., ZENKERT, D. & DESHPANDE, V. S. 2015. Dynamic compression response of self-reinforced poly(ethylene terephthalate) composites and corrugated sandwich cores. *Composites Part A: Applied Science and Manufacturing,* 77**,** 96-105.

SHIVAKUMAR, K., ELBER, W. & ILLG, W. 1985. Prediction of impact force and duration due to low-velocity impact on circular composite laminates. *Journal of applied mechanics,* 52**,** 674-680.

ST-PIERRE, L., DESHPANDE, V. S. & FLECK, N. A. 2015. The low velocity impact response of sandwich beams with a corrugated core or a Y-frame core. *International Journal of Mechanical Sciences,* 91**,** 71-80.

TIMOSHENKO, S. & GERE, J. 1963. *Theory of elastic stability,* London, McGraw-Hill.

XIONG, J., MA, L., WU, L., LIU, J. & VAZIRI, A. 2011. Mechanical behavior and failure of composite pyramidal truss core sandwich columns. *Composites Part B: Engineering,* 42**,** 938-945.

ZANGANI, D., ROBINSON, M. & GIBSON, A. G. 2008. Energy Absorption Characteristics of Web-Core Sandwich Composite Panels Subjected to Drop-Weight Impact. *Applied Composite Materials,* 15**,** 139-156.

ZENKERT, D. 1995. An introduction to sandwich structures.

ZHANG, J. & ZHANG, X. 2015. Simulating low-velocity impact induced delamination in composites by a quasi-static load model with surface-based cohesive contact. *Composite Structures,* 125**,** 51-57.